Epitaxial Growth of Ge-Sb-Te based Phase Change Materials

D I S S E R T A T I O N

zur Erlangung des akademischen Grades

doctor rerum naturalium (Dr. rer. nat)
im Fach Physik

eingereicht an der
Mathematisch-Naturwissenschaftlichen Fakultät I
Humboldt-Universität zu Berlin

von
M.Sc, M.Tech Karthick Perumal

Präsident der Humboldt-Universität zu Berlin:
Prof. Dr. Jan-Hendrik Olbertz

Dekan der Mathematisch-Naturwissenschaftlichen Fakultät I:
Prof. Stefan Hecht PhD

Gutachter:
1. Prof. Dr. Henning Riechert
2. Prof. Dr. W. Ted Masselink
3. Prof. Dr. Andreas D. Wieck

eingereicht am: 21. März 2013
Tag der mündlichen Prüfung: 30.Juli 2013

I dedicate this work
to my parents

ஐயிரண்டு மாதங்கள் கருவறையில் அடைகாத்து
ஈஎறும்பு அண்டாமல் கண்ணெனவே காத்தவளே!
ஏர்பிடித்த பரம்பரையில் வேர்பிடித்த என்னை
எழுதுகோல் பிடித்து ஏற்றம்பெற ஆலம்
விழுதாய் பாரம் தாங்கிய எம்தகப்பா!
கேட்டது கேட்டபடி கிடைத்தது என்வரமே!
ஈன்றெடுத்து ஆளாக்கிய உங்கள் இருவருக்கும்
சிறுகாணிக்கை இதோ சமர்ப்பணம் இவ்வாய்வேடு!

Ich widme diese Arbeit
meiner Familie

Abstract

Ge-Sb-Te based phase change materials are considered as a prime candidate for optical and electrical data storage applications. With the application of an optical or electrical pulse, they can be reversibly switched between amorphous and crystalline state, thereby exhibiting large optical and electrical contrast between the two phases, which are then stored as information in the form of binary digits. Single crystalline growth is interesting from both the academic and industrial perspective, as ordered Ge-Sb-Te based metamaterials are known to exhibit switching at reduced energies. The present study deals with the epitaxial growth and analysis of Ge-Sb-Te based thin films.

The first part of the thesis deals with the epitaxial growth of GeTe. Thin films of GeTe were grown on highly mismatched Si(111) and (001) substrates. On both the substrate orientations the film grows along [111] direction with an amorphous-to-crystalline transition observed during the initial stages of growth. The amorphous-to-crystalline transition was studied in-vivo using azimuthal reflection high-energy electron diffraction scans and grazing incidence x-ray diffraction. In the second part of the thesis epitaxy and characterization of Sb_2Te_3 thin films are presented. The third part of the thesis deals with the epitaxy of ternary Ge-Sb-Te alloys. The composition of the films are shown to be highly dependent on growth temperatures and vary along the pseudobinary line from Sb_2Te_3 to GeTe with increase in growth temperatures. A line-of-sight quadrupole mass spectrometer was used to reliably control the GeSbTe growth temperature. Growth was performed at different Ge, Sb, Te fluxes to study the compositional variation of the films. Incommensurate peaks are observed along the [111] direction by x-ray diffraction. The possibility of superstructural vacancy ordering along the [111] direction is discussed. Growth of GeSbTe on Si(111) substrate is found to be superior compared to the growth on Si(001) in terms of structural quality.

Keywords

Phase change materials, molecular beam epitaxy, quadrupole mass spectrometer, reflection high-energy electron diffraction, x-ray diffraction

Zusammenfassung

Ge-Sb-Te basierte Phasenwechselmaterialen sind vielersprechende Kandidaten für die Anwendung in optischen und elektrischen nicht-flüchtigen Speicheranwendungen. Diese Materialien können mit Hilfe von elektrischen oder optischen Pulsen reversibel zwischen der kristallinen und amorphen Struktur geschaltet werden. Diese stukturellen Phasen zeigen einen großen Unterschied in ihren elektronischen Eigenschaften, der sich in einer starken Änderung der optischen Reflektivität und des elektrischen Widerstands zeigt. Aufgrund dieser von der Struktur abhängigen Eigenschaften ist die Epitaxie von GST sowohl aus akademischer als auch industrieller Sicht von besonderem Interesse, insbesondere da semi-strukturierte GST Metamaterialien drastische reduzierte Schaltleistungen benötigen. Diese Studie befasst sich mit epitaktischem Wachstum und Analyse der epitaktischen Schichten.

Der erste Teil der Arbiet befasst sich mir dem epitaktischen Wachstum von GeTe. Dünne GeTe Schichten wurden auf Si(111) und Si(001) Substraten mit einer Gitterfehlanpassung von 10.8% präpariert. Auf beiden Substraten bildet sich in der GeTe Schicht die [111] Oberflächenfacette parallel zur Si(001) und Si(111) Oberfläche aus. Während des inertialen Wachstums findet eine Phasentransformation von amorph zu kristallin statt. Diese Phasentransformation wurde mittels azimuthaler in-situ Beugung hochenergetischer Elektronen sowie in-situ Röntgenbeugung unter streifendem Einfall untersucht.

Der zweite Teil der Arbeit wird die Epitaxie sowie die strukturelle Charakterisierung dünner Sb_2Te_3 Schichten dargestellt.

Der dritte Teil umfasst die Epitaxie terniärer Ge-Sb-Te Schichten . Zum Wachstum wurden sowohl die Substrattemperatur als auch die Ge, Sb und Te Flüsse variiert. Es wird gezeigt, dass die Komposition der Schicht stark von der Wachtumstemperatur abhängt und nur entlang der pseudibinären Verbindungslinie von GeTe-Sb_2Te_3 variiert. Zur Kontrolle des Wachstums wurde dabei die in-situ Quadrupol Massenspektroskopie verwendet. Es zeigen sich diverse inkommensurate Beugungsmaxima entlang der [111] Oberflächennormalen der Schichten, anhand derer die Ausbildung einer Lehrstellen Ordnung in Form einer Überstruktur diskutiert wird.

Es zeigt sich, dass das Wachstum auf Si(111) Substraten gegenüber dem Wachstum auf Si(001) Substraten bezüglich der kristallinen Qualität überlegen ist.

Schlagwörter

Phasenwechselmaterialen, Molekularstrahlepitaxie, Quadrupolmassenspektrometer, Reflektions-Hochenergie-Elektronenbeugung, Röntgenbeugung

Contents

1 Motivation

Integrated circuits that perform basic computations and or storage functions are part of almost all electronic devices. With the advent of information technology, there is an ever increasing demand for high speed and large capacity storage devices. In 1965, Gordon Moore [1] predicted that the number of transistors in an integrated circuit is expected to double every 2 years. It is still valid even after five decades. Scaling down of conventional solid state memories has helped in increasing the storage capacity and reducing the programming currents over the years. For example, the first commercially available microprocessor was the Intel 4004 in the year 1971, which had just 2300 transistors, whereas 40 years later Xilinx packed 6.8 billion transistors in a chip. According to the international technology roadmap for semiconductors [2], the transistor gate size will shrink to 8 nm in 2026. However miniaturization of transistors in a chip is limited by the wavelength of the light used in the lithographic process and the corresponding photosensitive material. Another main problem of scaling down of the transistors in the integrated circuits is the high leakage current resulting in power dissipation.

In order to extend the Moore's law to be applicable for few more decades, novel materials with better scalability and programming currents as potential replacement for the conventional memory devices are required. Present day computers use two types of memory: volatile and non-volatile. For example, the main memory in the computer is DRAM, which belongs to the category of volatile memory. It has high read/write speed, low cost, but needs constant power to store the data. In case of power outage, all the saved contents will be lost. On the other hand, flash memory, which belongs to the class of non-volatile memory does not need a constant power to store the data. The disadvantage is that the read/write speed is low, it has a limited endurance of only a million times and high cost. A material which has the advantages of both DRAM and flash memory with better scalablitiy might be boon for the consumer industry.

GeTe-Sb_2Te_3 based phase change material (PCM) is one such candidate which is considered as a strong contender for replacement of flash and DRAM memories. In contrast to the charge based storage technologies such as DRAM or flash memory, in PCM information is stored on the basis of resistive state. Resistive memories have the advantage of better scaling than their charge based counterparts, also they do not require precise charge control. Binary digits 0 (reset) and 1 (set) are stored by switching the material between an amorphous high resistance state and the crystalline low resistance state. Though all materials can undergo phase change between amorphous and crystalline state, they do not exhibit the mandatory properties for use in commercial applications. For a material to be regarded as a good phase change material and to be economically viable, it should have the following properties: fast switching speed, ability to withstand large number of switching cycles without material degradation, good scalability, low programming energy, non-volatility, low production cost, long data-retention capabilities and above all should exhibit strong optical/electrical contrast between the two stable states. Already few companies such as Samsung and Micron knowing its enormous potential for future,

started the commercialization of PCRAM devices. Recent work shows the promise of multilevel phase change memory in computing, where upto 4 bits can be stored in a single cell, which greatly reduces the cost per bit for data storage and computation[3,4].

In addition to the commerical potential based on electrical contrast, PCM also exhibit strong optical (refractive index) contrast: high reflectivity in crystalline phase and low reflectivity in amorphous phase. Unlike switching by electrical pulse in electrical devices, in the case of optical discs switching between the two phases is performed by an optical laser pulse. This difference in reflectivity between the two phases is commercially being exploited for almost more than two decades in the optical data storage industry for use in CDs, DVDs, and Blu-Ray discs[5–10]. Despite its widespread usage in optical discs for data storage, the switching mechanism is still a matter of debate.

Kolobov et al.,[11] provided an initial breakthrough in understanding the switching mechanism by his widely known Umbrella flip model, where Ge atom is shown to switch from tetrahedral to octahedral coordination upon crystallization. Recently two groups independently reported that, GST which has bonding energy hierarchy, can be switched between the amorphous and crystalline states *via* non-thermal route by the destruction of weaker bonds and hence collapse of long range ordering[12,13]. Most of the studies aimed at understanding the switching mechanism were done on polycrystalline films, where the presence of grain boundaries and orientational disorder might pose limitations in understanding the structural change upon switching. Molecular beam epitaxy (MBE) offers the possibility to fabricate films of high structural quality. Additionally single crystal growth appears to be promising, as ordered metamaterials require less energy to switch between amorphous and crystalline phase[14,15]. Thus epitaxial growth of GST seems to be interesting from both the academic and industrial perspective, in terms of understanding the switching process and reducing the switching energy.

1.1 Aim and Organization of this Thesis

The aim of this thesis is to understand and improve the epitaxial growth of GeTe-Sb_2Te_3 (GST) based phase change materials lying along the technologically important pseudobinary tie line from GeTe to Sb_2Te_3. The thesis is organized as follows,

- Chapter 1 briefly describes the crystal structure as well as some physical properties relevant to the understanding of the phase change materials described in this work, namely GeTe, Sb_2Te_3 and GST.

- Chapter 2 is dedicated to the description of the MBE system and substrate preparation followed by a short description of several analytical techniques used during the course of this work such as, reflection high-energy electron diffraction (RHEED), quadrupole mass spectrometer (QMS) and x-ray diffraction (XRD).

- In chapter 3, the growth of GeTe is presented. Etching property of Tellurium on Germanium is discussed, followed by the epitaxial growth of GeTe on Si. The film evolution during the growth in terms of structural properties is studied by azimuthal RHEED and

in-vivo synchrotron XRD. Calibration of the QMS for *in-situ* compositional analysis is given.

- In chapter 4, epitaxial growth of Sb_2Te_3 is studied by atomic force microscopy (AFM) and XRD.
- Chapter 5 deals with the growth temperature related compositional changes involved in GST epitaxy, along with the limitations posed by inaccurate control of substrate temperature *via* a non-contact thermocouple. The use of QMS for growth control of GST is discussed, followed by the effect of change in supplied Ge, Sb and Te flux on composition. Incommensurate XRD peaks observed for GST along the [111] direction are considered as a fingerprint for a superstructural ordering.
- Chapter 6 gives a summary of the obtained results as well as an outlook for future experiments.

2 GeTe-Sb_2Te_3 based Phase Change Materials: An Introduction

The following chapter deals with the physical properties exhibited by phase change materials that lie along the pseudobinary line between GeTe and Sb_2Te_3.

2.1 GeTe

At low temperatures, GeTe is a ferroelectric material[16] that possesses a rhombohedral structure with a space group R3m. This structure can be visualized as a distorted rocksalt structure as shown in figure 2.1 (a), with a lattice constant of 5.985 Å and a distortion of 88.2° along the [111] direction[17–19]. In the case of undistorted rocksalt lattice, every Ge atom is surrounded by 6 Te atoms, and should have equal bond lengths, with a bond length of 2.99 Å[19]. GeTe, with mainly sp^3-p orbital bonding, undergoes Peierls distortion[20] to form a distorted rocksalt structure. The distortion appears along [111] direction and causes the formation of three shorter covalent bonds and three longer resonant bonds with bond lengths of 2.84 Å and 3.15 Å, respectively[19,21,22].

Upon heating, GeTe undergoes a structural phase transition from rhombohedral to rocksalt structure at around 700 K[19,23]. At this temperature Peierls distortion disappears as thermal energy outweighs the energy gained by Peierls distortion[20]. In the cubic rocksalt structure, the Ge and Te atoms are at equal distances, with a bond length of 2.98 Å . However, neutron diffraction studies on liquid GeTe (on melting) shows the presence of Peierls distortion, which the authors coin it as "reentrant Peierls distortion"[24–26]. To sum up, the Peierls distortion is observed in low temperature rhombohedral phase, disappears in rocksalt structure at around 700 K and re-enters in the liquid phase. This unusual phenomenon stirred the interest of few authors[23], who decided to investigate the high temperature rocksalt structure, where the disappearance of Peierls distortion is observed. The technique used was extended x-ray absorption fine structure (EXAFS). EXAFS is a powerful tool to study local structure of the atoms, its coordination number and bond lengths. They observed that, even above the transition temperature, the short and long bonds do not converge to the reported value from diffraction data, rather they remain separated with different bond lengths[23]. Thus they conclude that the Peierls distortion does not vanish in the rocksalt phase. They further conclude that instead of a displacive transition, an order-disorder transition occurs. The discrepancy with previous studies was explained by the fact that the distortion remains hidden in Bragg diffraction due to the averaging effects.

Peierls distortion in the low temperature rhombohedral phase is observed mainly because of the coherent distribution of atoms along a particular direction. This is not the case for high temperature cubic phase, where random distortions are present due to atomic vibrations. This leads to the fact that the interatomic planes appear equidistant. In the case of liquid GeTe,

the absence of sharp diffraction peaks in neutron scattering technique forced the authors to use pair-distribution analysis, that does not suffer from the averaging effects of Bragg diffraction. So, the short and long bonds were detected[25].

Upon switching from the crystalline to the amorphous phase, Ge atoms undergo a transition from octahedral to tetrahedral coordination, with the breaking of longer (weaker) bonds and the strengthening of shorter (stronger) covalent bonds with a bond length of about 2.60 Å[11]. In the amorphous phase, resonance bonding disappears due to the loss of long range order, causing a significant change in its electrical properties[27].

GeTe alloy having an equal amount of Ge and Te does not exist. Samples prepared from stoichiometric GeTe target through sputtering, have an excess of Ge in addition to the GeTe phase. Post-annealing studies on amorphous samples with different Ge concentrations showed the precipitation of Ge. EXAFS analysis on GeTe thin films showed that there are peaks corresponding to Ge-Ge bonds, which fits to an amount of 10% indicating the presence of vacancies in the Ge sublattice and segregation of Ge atoms[21]. In the GeTe crystalline phase, there is always a small percentage of less germanium than tellurium and vacancies are intrinsic to the Ge sublattice[28–30]. The role of vacancies and its influence on the switching mechanism is unclear.

GeTe is a p-type degenerate semiconductor with a narrow band gap of 0.1-0.2 eV[31]. The p-type conductivity is attributed to the vacancies in the Ge sublattice[32]. Density functional theory calculations show that the low temperature rhombohedral phase behaves like an indirect band gap semiconductor with a band gap of 0.27-0.33 eV, while the high temperature cubic phase (> 720 K) shows a direct band gap of 0.13-0.15 eV[33]. In the amorphous phase, GeTe has a band gap of 0.8 eV[32]. It shows a large electrical contrast of about 6 orders of magnitude between the amorphous (resistivity of about 10^2-10^3 Ωcm) and crystalline phase (resistivity of about 2-4x10^{-4} Ωcm)[32,34–36]. Amorphous and crystalline phases exhibit negative and positive temperature coefficient of resistivity, respectively[32]. At 633 nm, the optical reflectivity of amorphous GeTe is around 45%, while in the crystalline phase it shows enhanced reflectivity of about 65%[34]. Huber et al., observed reflectivity changes occur at lower fluences than the conductivity changes upon switching. However they attribute this phenomenon to the surface sensitivity of reflectivity[34]. Lucovsky and White reported that the presence of delocalised electrons (resonance bonding) in crystalline IV-VI materials is the cause of large difference in optical and electrical properties between the two phases[27]. Conversely, this has also helped in identifying the materials suitable for non-volatile phase change memory applications[37].

2.2 GeSbTe based Alloys

Materials lying along the pseudobinary tie line between GeTe and Sb_2Te_3 are considered to be the most auspicious for phase change memories[38]. They possess a metastable low temperature phase as shown in figure 2.1 (b) and a stable hexagonal high temperature phase. It was experimentally found that the metastable phase is NaCl type crystal structure ($Fm\bar{3}m$) with the 4a site randomly occupied by Ge, Sb or vacancies and the 4b site completely occupied by Te atoms, while the vacancy concentration present in the 4a site depends on the composition of the material system[39,40]. The most widely used compositions in the Digital versatile discs (DVDs) and

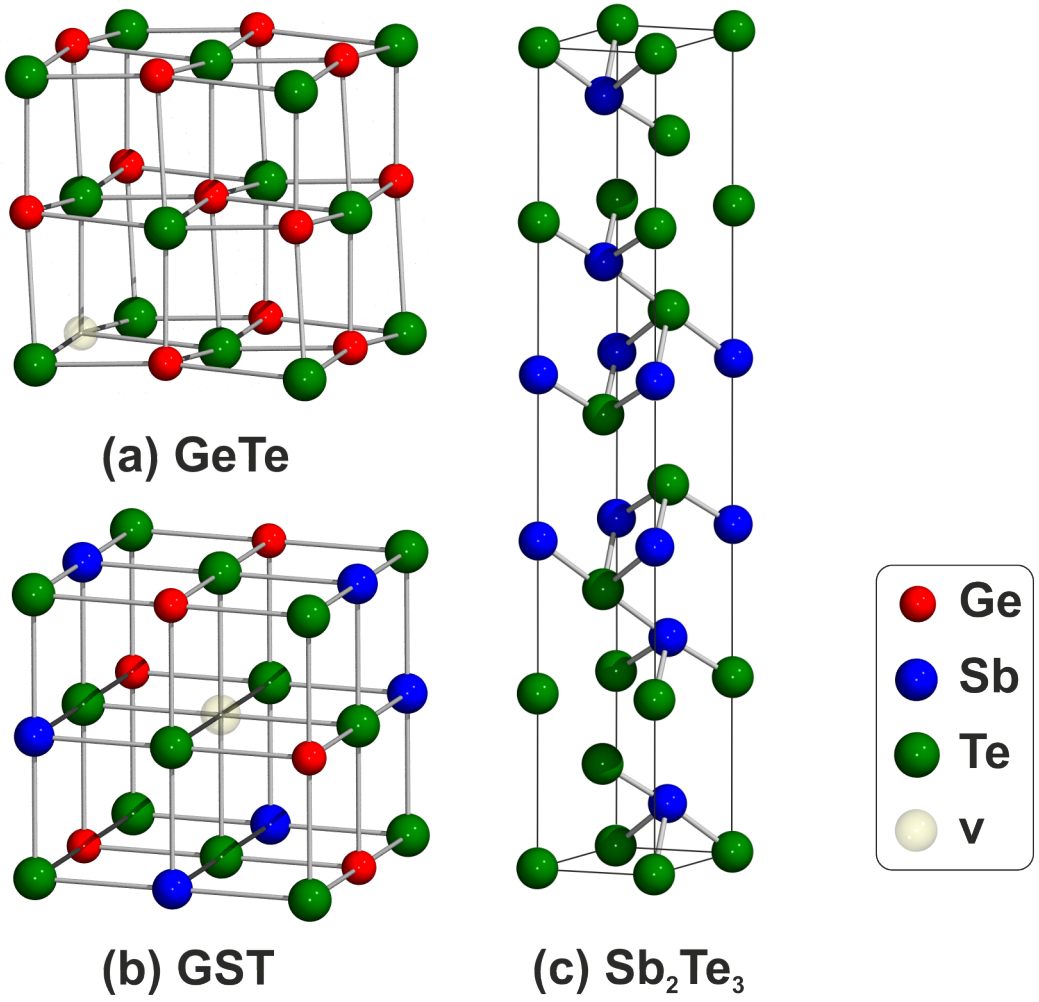

Figure 2.1: (a) Distorted rocksalt structure of metstable GeTe. (b) Metastable face centered cubic GST with Te occupying one sublattice and Ge/Sb/vacancies (v) randomly occupying the other sublattice. (c) Hexagonal Sb_2Te_3 with three quintuple layers (-Te-Sb-Te-Sb-Te-) per unit cell

Blu-ray discs (BD) are $Ge_2Sb_2Te_5$ and $Ge_8Sb_2Te_{11}$ respectively. Density functional theory total energy calculations on $Ge_2Sb_2Te_5$ show that Sb and Ge atoms in GST favour two-dimensional and three-dimensional structures perpendicular to [111] direction, respectively and random arrangement of vacancies, which is not the case for $Ge_1Sb_2Te_4$, where Ge and vacancies prefer a two-dimensional layered structure perpendicular to [111] direction[41]. Molecular dynamics simulations on crystalline $Ge_8Sb_2Te_{11}$ provide the Ge-Te and Sb-Te short/long bond lengths to be about 2.86/3.13 Å and 2.98/3.19 Å respectively[42]. GeTe rich $(GeTe)_m$-$(Sb_2Te_3)_n$ alloys show a slightly distorted rhombohedral low temperature structural phase and a high temperature cubic NaCl structure, with the rhombohedral to cubic transition temperatures increasing with increase in GeTe content. Unlike GeTe rich GST alloys, materials with a concentration less than m:n = 6:1 ratio exhibit a high temperature hexagonal phase[43]. Compositional phase boundary is expected between m:n = 8:1 and 6:1, with a high concentration of vacancies present only in the rocksalt phase and not in the high temperature stable phase[43]. In addition migration of Ge/Sb atoms to fill the vacancy sites in $Ge_1Sb_2Te_4$ was proposed[44].

Ab-initio simulations on $Ge_2Sb_2Te_5$ alloy by Zhou et al., showed that the stable hexagonal phase contains intrinsic vacancies between the weakly bonded Te-Te layers[45]. Petrov et al. proposed for the stable hexagonal $Ge_2Sb_2Te_5$ alloy, a 9-layered structure per unit cell[46] following the ABC stacking sequence Te-Sb-Te-Ge-Te-Te-Ge-Te-Sb-. Kooi and De Hosson[47] taking the Ge-Sb immiscibility into account, suggested a similar structure with Ge and Sb atoms interchanged, so that the final structure is a combination of GeTe and Sb_2Te_3 basic unit cells, with stacking Te-Ge-Te-Sb-Te-Te-Sb-Te-Ge-. However, Matsunaga et al., based on diffraction measurements from stable $Ge_2Sb_2Te_5$ alloy proposed alternating layers of Te with Ge/Sb layers in between. Their stacking sequence is Te-Ge/Sb-Te-Ge/Sb-Te-Te-Ge/Sb-Te-Ge/Sb- with the disappearance of vacancies in the stable phase[43,48]. *Ab-initio* total energy calculations show that the lowest energy and hence the most stable configuration is that of the model proposed by Kooi and De Hosson: Te-Ge-Te-Sb-Te-v-Te-Sb-Te-Ge-, with an added vacancy layer named by 'v'[49]. The calculations further show that the vacancy layers are highly ordered and lie along [111] direction between the weak Te-Te bonding layers.

While Ge atoms in crystalline phase are shown to exhibit an octahedral coordination, upon switching to amorphous phase EXAFS results show a tetrahedral coordination[11]. Recent paper by Liu et al., based on electron microscopy, diffraction measurements and first principle calculations show that about 35% of the Ge atoms in cubic $Ge_2Sb_2Te_5$ exhibit a tetrahedral coordination indicating a coexistence of both tetrahedral and octahedral coordination in the cubic phase[50]. Unlike the Umbrella flip model proposed by Kolobov et al., Liu et al., explain the fast phase transition by means of local rearrangement of the tetrahedral and octahedral Ge-centred clusters minimizing the space to form cubic phase. The Ge-Te and Sb-Te bonds get stronger and shorter with bond lengths of 2.61 Å and 2.85 Å respectively upon amorphization[51]. Molecular dynamics simulations on $Ge_8Sb_2Te_{11}$[42] show that about 42% of the Ge atoms exhibit 4-fold coordination, while most of the Sb atoms prefer 6-fold coordination.

The band gap changes from indirect to direct along the pseudobinary line from GeTe to Sb_2Te_3[52] and the band gap energy decreases with increase in Sb content[53]. The electrical conductivity and hole concentration decrease, whereas the Hall mobility increase with increase in Sb content[54].

Taking into account the studies of Lucovsky and White[27] on IV-VI materials, Shportko et al., extended it to the GST material system and attributed the large changes in optical properties to the difference in bonding between the two phases. The amorphous phase exhibits covalent type bonding and upon switching the crystalline phase exhibits resonant bonding. Crystalline phase displays 70-200% larger optical dielectric constant than the amorphous phase[37]. For a wavelength of 405 nm, the optical contrast was found to increase with increase in Ge concentration[55]. Along the pseudobinary line from GeTe to Sb_2Te_3, the crystallization temperature and thermal stability increase, while the crystallization speed decreases.

For optical and electrical data storage applications, depending on the requirements, suitable material is selected from the pseudobinary line. For high density optical recording, material system toward higher GeTe content is used, due to its better contrast at lower wavelengths. However, in electrical memories, a compromise between fast switching speed and high stability of the amorphous phase is required and in this case, the most promising and widely studied material proves to be $Ge_2Sb_2Te_5$.

2.3 Sb_2Te_3

Sb and Te belonging to group V and VI, possess 3 and 2 valence electrons available for bonding respectively, enabling it to form the stoichiometric compound Sb_2Te_3. In contrast to GeTe and GST, Sb_2Te_3 possesses only a single, stable hexagonal crystal structure as shown in figure 2.1 (c) with space group $R\bar{3}m$, lattice constants found to be about a_0= 4.26 Å and c_0= 30.46 Å[56–59]. Along the [00.1] direction, it forms a layered structure with only one kind of atom in each layer. The stacking sequence along the [00.1] direction is Te-Sb-Te-Te-Sb repeated 3 times to form a 15 layer sequence[57]. The Sb-Te bonds are alternately shorter and longer with lengths of 2.98 and 3.17 Å respectively, whereas the Te-Te weaker bonds are longer (3.74 Å)[57]. Similar to the stable GST hexagonal structures proposed by Sun et al., also for Sb_2Te_3 vacancies are expected to be ordered normal to the [00.1] direction and in between Te-Te layers[60]. There are only few studies on the local structure in the amorphous phase and hence a detailed understanding is lacking. However, EXAFS measurements show that both (short and long) Sb-Te bond lengths decrease upon amorphization[61].

Sb_2Te_3 is a p-type[58] narrow band semiconductor (0.28 eV[62]) with applications in thermoelectric devices due to its high thermoelectric figure of merit[63,64]. It is also found to exhibit topologically insulating properties i.e., metallic properties at the surface and intrinsically insulating[65,66]. A minimum of 5 quintuple layers (-Te-Sb-Te-Sb-Te-) (or 50.76 Å) are required for Sb_2Te_3 to exhibit topologically insulating behaviour[65]. The electrical resistivity of amorphous films is reported to be about $\sim 10^3$ Ωcm and upon phase transition to crystalline phase, the resistivity decreases to about $\sim 10^{-5}$ Ωcm[63]. Das et al., studied the dependence of electrical resistivity with thickness and found an inverse linear relationship[63].

2.4 Optical Devices

Though the principle of reversible phase switching of chalcogenide materials was proposed by Ovshinsky in 1966[67], it took quite a long time for commercialization, mainly because of the

low switching speeds and limited cyclability of the material used for demonstration. Initial breakthrough in commercialization of PCM by using the optical switching properties was made by Yamada et al., who showed better switching characteristics with high cyclability of materials along the GeTe-Sb_2Te_3 pseudobinary line[38]. Initial optical discs, such as compact discs employed a wavelength of 780 nm in the near infrared for optical recording, had a capacity of 700 MB. As the density of recording is inversely proportional to the wavelength of light used, the data recording densities of optical discs started improving with the development of low cost laser diodes in the shorter wavelength regime. Digital versatile discs (DVD) use 650 nm wavelength laser for recording and have a capacity of 4.7 GB. The situation further improved with the development of the dual layer recording, which increased the storage capacity on an optical disc[8]. Recently Blu-ray discs employing 405 nm diode laser can store upto 50 GB of data in a dual-layer mode. Further research is going on to increase the storage capacity and recently Nishihara et al., showed the possibility of triple-layer Blu-ray disc with a capacity of 100 GB[10].

2.5 Electrical Devices

Scaling issues in conventional solid state memories pose a serious problem for the semiconductor industry and new material systems are being investigated for increasing the storage density and reducing the read/write time. Phase change random access memory (PCRAM) is considered as a serious contender for the present day RAM and flash memories. Main advantages being its non-volatile nature, low power operation[68,69], superior switching speed with high cyclability[15,70] and better scaling capabilities[71,72]. Detailed studies by Perniola et al., show GeTe to be a viable alternative to GST with better programming speed, resistivity contrast and endurance[73]. Samsung and Micron have already started commercialising PCRAM which are used in the low-end mobile phones. Other companies such as SK Hynix and IBM have signed an agreement to jointly produce PCRAM. Recently Samsung developed 8 GB PCRAM with a cell size of 41x41 nm^2 and a program bandwidth of 40 MB/sec[74]. With more and more companies having their sight on commercialization of PCRAM, faster computing systems are set to emerge.

3 Experimental Techniques

This chapter presents the experimental techniques used for the synthesis and characterization of the samples discussed throughout the reminder of the thesis.

3.1 Molecular Beam Epitaxy

MBE is a powerful technique that allows the synthesis of epitaxial thin films of metals,[75] oxides and semiconductors. Localized atomic or molecular beams sublimated from highest purity effusion sources impinge on a heated substrate under ultrahigh vacuum (UHV) conditions of about 10^{-11} Torr. UHV ensures low partial pressure of impurities, clean growth environment, and high mean free path of the atomic/molecular beam that far exceeds the dimensions of the chamber. To achieve good epitaxial films, single crystalline substrates with high surface quality free from impurities are selected and the slow grow rate allows sufficient time for the impinging atoms to diffuse on the surface of the heated substrate to form atomic layers. The MBE chamber is cryogenically cooled in order to condense unused beam flux and to reduce the background pressure[76]. It also acts as a thermal insulation between the cells. Shutters in front of the effusion cells enable to instantly turn off the atomic/molecular beam. The MBE further offers the advantage of using various *in-situ* characterization tools such as RHEED, QMS and grazing incidence x-ray diffraction (GIXRD).

The samples reported in this thesis are grown in a compact Createc MBE system, that is designed for *in-vivo* GIXRD studies at the PHARAO beamline of the synchrotron, BESSY II. Figure 3.1 shows the schematic diagram of our MBE system. The MBE system consists of three units. A load lock for introducing the substrates, a transfer chamber for degassing the substrates and a growth chamber for epitaxial growth. Highest purity atomic sources of Ge, Sb and Te are evaporated from dual filament effusion cells equipped with crucibles of pyrolitic boron nitride. The substrate is heated radiatively and its temperature is measured *via* a non-contact thermocouple. Proportional integral derivative controllers are used to accurately control the temperatures of the cells and substrate.

3.2 Surface Processes in Epitaxial Growth

At very low temperatures, the atoms impinging on the surface do not move because of their very low energies and less thermal mobility. Epitaxial growth is usually performed at elevated substrate temperatures, where the atoms become more mobile on the surface. Atomic or molecular species impinging on the hot substrate might get chemisorbed or physisorbed on the surface and undergo various surface processes. The atoms/molecules can undergo different processes such as (a) surface diffusion on a flat surface, (b) form two dimensional clusters with nearby adatoms,

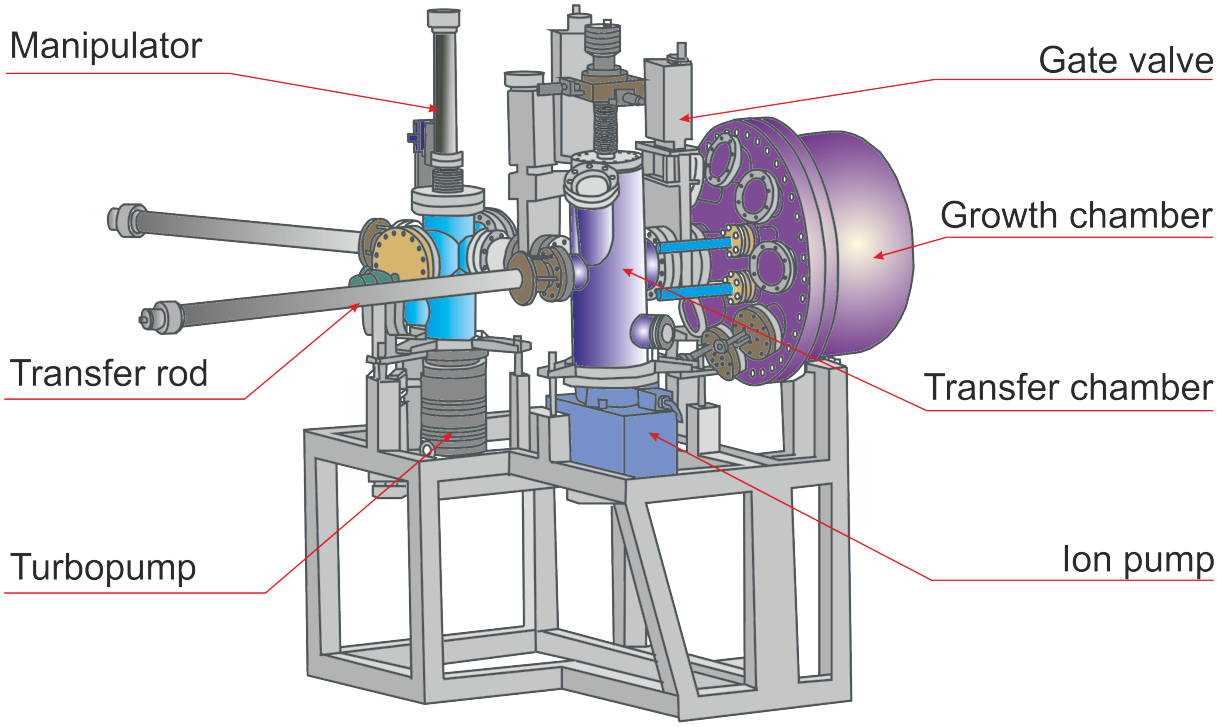

Figure 3.1: Schematic diagram of the MBE chamber used for growing phase change materials

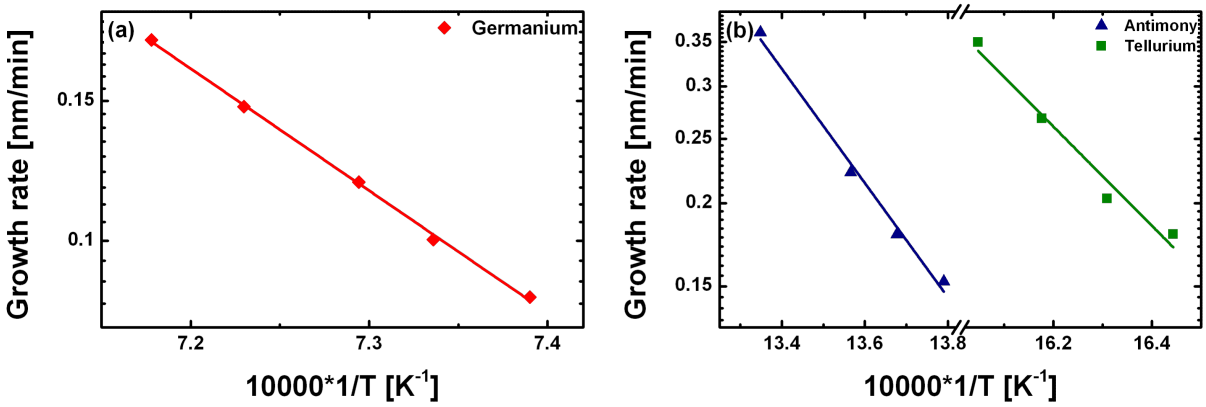

Figure 3.2: Arrhenius plot of growth rate versus inverse temperature along with their fit for (a) Germanium (red rhombus), (b) Antimony (blue triangle) and Tellurium (green squares)

(c) can be incorporated along the step edges, (d) migrate along the step to incorporate at a kink and (e) can undergo desorption from the surface. The length scale, time and energetics of each event depend on a large number of factors. In the case of rough surfaces for instance, surface migration will be negligible. Temperature, surface orientation and reconstruction affect the surface diffusion. Desorption occurs, if the adsorbate atoms/molecules have enough energy to overcome the activation energy barrier for desorption. A detailed theory of the surface processes is given here[77].

3.3 Flux Calibration

Before performing the growth, accurate calibration of the source fluxes are necessary. For materials which exhibit layer by layer growth, the flux calibration might be done by measuring the intensity oscillations of the specular beam as observed by RHEED. However, in most of the cases, layer by layer growth does not occur. In those cases, a beam flux monitor, quartz crystal monitor or optical-based flux monitor are used. Our MBE chamber is not equipped with any of those *in-situ* instruments for calibrating the flux. So, we perform amorphous growth of the different materials namely Ge, Sb and Te at very low substrate temperatures. At sufficiently low substrate temperatures, all the atomic species will have unit probability of sticking and no desorption takes place. Growths are performed by varying the source fluxes and the thicknesses are measured by XRR. Figure 3.2 shows the Arrhenius plot of growth rate vs temperature inverse for the three effusion cells hosting Ge, Sb and Te.

It is however necessary to check the growth rate every few weeks to monitor the depletion of the sources and the temperature of the effusion cells should be increased appropriately to compensate for the decrease in flux. This procedure suffers from the limitation that the measurements are not *in-situ* and time consuming compared to the beam flux monitor which can be used to monitor

day-to-day fluctuations *in-situ*.

3.4 Substrate Preparation

Highest quality single crystalline atomically smooth surfaces are required for growing epitaxial films. The surface should be free from any contaminations or oxides that hinder the realization of high quality epilayer. Silicon substrates with dimensions of ($20mm \times 20mm \times 0.525mm$), resistivity 1-10 Ωcm, p-type Boron doped and a miscut of $\pm 0.03°$ from Crystec were used for the experiments. First the substrates are dipped in warm acetone with a magnetic stirrer for 10 minutes and 5 minutes in propanol to remove organic contaminations on the surface. They are then rinsed in de-ionised (DI) water for 10 minutes. To remove organic contaminants that are visible on the surface, the substrates are dipped in a mixture of 4 parts 97% concentrated sulphuric acid (H_2SO_4) followed by 1 part 30% hydrogen peroxide (H_2O_2) usually called Piranha etch[78]. Care should be taken to always add the peroxide to the acid and not the other way around. The mixture is strongly exothermic and can reach temperatures of about 100 °C. This procedure is followed by the standard cleaning procedure 1 (SC-1) as proposed by Kern[78]. The SC-1 solution consists of 5 parts of DI water added with 1 part of ammonium hydroxide (NH_4OH) and 1 part of hydrogen peroxide (H_2O_2) heated to about 70 ï¿½C. The substrates are dipped in this solution for a duration of 15 minutes during which removal of particles, certain metals and other organic contaminants on the surface take place. This procedure dissolves the native oxide layer and forms a new oxide layer by oxidation. This is considered to be the main reason behind the removal of particles and organic impurities. The substrates are then cleaned with plenty of DI water. Prior to growth, the oxides on the Si surface that are formed during SC-1 process are removed by dipping the substrate in 5% HF solution for about 10 minutes and then rinsing with DI water to form a stable hydrogen terminated surface. The sample is immediately loaded into the load lock chamber of the MBE system and undergoes water desorption treatment at 150ï¿½C for 30 mins. This is followed by degassing at 350 ï¿½C in the transfer chamber before introducing into the growth chamber, where the substrate is heated upto 720 ï¿½C to get Si(111)-7x7 reconstruction (Si(001)-2x1 reconstruction).

Undoped GaSb(001) and (111) epi-ready substrates were prepared for growth by desorbing the native oxide under Sb flux, followed by deposition of a 100 nm thick GaSb homoepitaxial buffer layer at 350 ï¿½C using standard III-V growth techniques[79]. The thickness of the overgrown buffer layer is determined by the growth oscillations as observed by the RHEED intensity fluctuations of the specular reflection. The typical thickness of our buffer layers varies between 10-20 nm. In the absence of In and As sources in the GST MBE system, homoepitaxial buffer growth of InAs has to be performed separately. The substrates are loaded in a dedicated MBE system, annealed up to 460-490 ï¿½C to remove the native oxide and then overgrown with a 100 nm thick homoepitaxial buffer layer at 400 ï¿½C. During the cooling process, the As-stabilized (2×4) reconstructed InAs(001) surface pattern changes, displaying a diffuse (1×1) reconstruction[80]. The buffer grown InAs(001) substrates were transferred to the GST MBE system using a vacuum shuttle to preserve the surface quality and to prevent oxidation or contamination. InAs(111)A substrates were directly introduced into the GST growth chamber to remove the native oxide at 490 ï¿½C and no subsequent buffer growth was performed. InAs(111)B surfaces

have poor surface morphology on oxide desorption compared to InAs(111)A surfaces. Hence, for the epxeriments In terminated surface were used. RHEED was used to monitor the surface quality during substrate preparation as well as the surface evolution during growth.

3.5 Reflection High-Energy Electron Diffraction

RHEED is an *in-situ* surface sensitive technique employed in almost all MBE systems for real time characterization of growth processes. It is useful to determine the orientation, quality and reconstruction of the surface. The experimental setup is rather simple, a high energetic electron beam (20 keV) produced by an electron gun impinges on a sample surface at glancing angles and the resulting diffraction pattern is sensed by a phosphorescent screen located opposite to the electron gun, and further recorded digitally by a charge coupled device. The sample can be rotated along an axis normal to its surface, thus enabling access to different crystallographic directions by RHEED. The electron penetration depth according to Kanaya and Okayama[81] is given by

$$R = \frac{27.6 \times 10^{-12} E^{1.67} A}{\rho Z^{8/9}}$$

where, E is the accelerating voltage (20 keV), A is the atomic weight, ρ the density and Z is the atomic number. For Silicon, the penetration depth is about 47.3 Å. At an angle of θ, the penetration depth further decreases by a factor $l = Rsin\theta$. For a grazing incidence angle of 2°, the penetration depth is about 1.6 Å resulting in highly surface sensitive diffraction at the surfaces. Thus the real time monitoring of the surface evolution during the growth is possible with RHEED. The surface acts like a two dimensional diffraction grating and the reciprocal lattice of a two dimensional surface consists of infinitely long rods perpendicular to the surface usually called crystal truncation rods (CTRs)[82]. The de Broglie wavelength (λ in Å) of an electron having a kinetic energy V (in eV) is given by

$$\lambda = \sqrt{\frac{150.4}{V}} \tag{3.1}$$

For a 20 keV electron beam, λ is 0.087 Å and the corresponding magnitude of the wavevector k is 72.5 Å^{-1}. Thus the Ewald sphere will be large (construction of Ewald sphere is given in section 3.7) and the Laue diffraction condition for diffraction maxima occurs, when the Ewald sphere cuts the CTRs. Figure 3.3 shows the schematic diagram of CTRs cutting the Ewald sphere to produce diffraction maxima at the screen. In ideal conditions, CTRs intersect the Ewald sphere at specific points and would only give rise to spots on the Laue circle in the RHEED screen. However in non-ideal case, due to several limitations such as divergence of electron beam, energy spread of the incident electrons on non-ideal surfaces, the intensity of the sharp spots spread along the CTRs resulting in streaky intensity pattern. The presence of Kikuchi patterns (Bragg diffraction of inelastically scattered electrons by the crystal lattice planes) also indicate a well ordered epitaxial layer. Kikuchi patterns are sensitive to surface morphology and broadened by from small terraces or steps. In the case of a rough surface, the electron beam transmits through

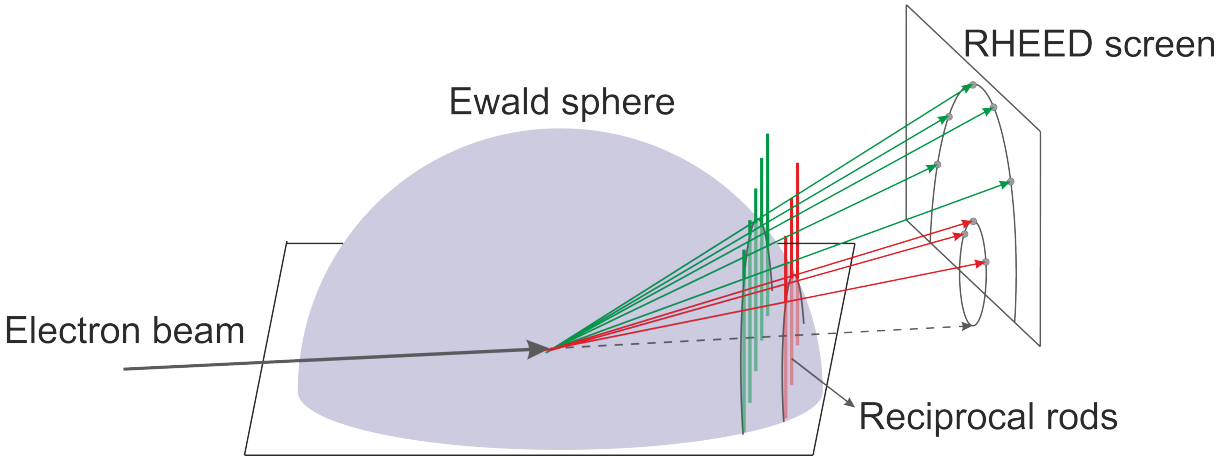

Figure 3.3: Three dimensional diagram depicting the CTRs cutting through the Ewald sphere producing 0^{th} and 1^{st} order Laue pattern on the RHEED screen in red and green respectively

the islands or mounds to form diffraction spots. An amorphous surface does not produce any diffraction pattern due to the absence of ordered arrangement on the two dimensional surface. However if the surface is polycrystalline, all possible diffraction patterns are superimposed and result in concentric rings as in a typical powder diffraction pattern.

3.6 Quadrupole Mass Spectrometer

QMS is based on the stability of ion trajectories in oscillating electric fields[83]. It ideally consists of four hyperbolic rods set parallel to each other. However, due to the complexities involved in designing hyperbolic rods, circular rods are used with the condition that the radius of the circular electrode r should be equal to 1.1468 r_0 to achieve higher sensitivity or lower driving power[84]. A pair of opposite rods is applied a potential of (U+V cos ωt) and the other pair of rods with -(U+V cos ωt), where U is a time-independent dc potential and Vcos ωt is a time-dependent alternating potential with an angular frequency of ω (given by $\omega = 2\pi\nu$, where ν is the radio frequency or rf). In the first part of the rf cycle, two rods are at positive potential and the other two are at negative potential. Thus positive ions get squeezed in a plane perpendicular to the plane in which the rods are at positive rf potential. During the next half cycle the direction reverses and thus the ions travel through the quadrupole with a complex trajectory. For a given dc and ac potentials, only certain ions pass through the quadrupole and all other ions which fail to satisfy the particular mass-to-charge ratio (m/z) are lost. By increasing the rf frequency and ac potential, the quadrupole acts like a high pass filter. Low m/z ions have a larger acceleration and hence greater amplitude of oscillation, resulting in the ions getting lost or colliding with the rods due to unstable trajectory. Thus low m/z ions can be selectively filtered by appropriate rf frequency and potential. On the other hand, dc voltage affects high m/z ions, as they are weakly refocused with the change in rf frequency and slowly drift towards the electrodes, while low m/z

ions are easily refocussed and not affected greatly by the dc voltage. Thus QMS acts like a low pass filter. Using the right combination of the dc and ac potential, ions below a certain mass range are lost because of their unstable trajectory, while ions above the selected mass range are lost due to poor focusing[85]. Detailed theory about the quadrupole mass analyser and the QMS stability diagram are reported here[86].

Among the various studies performed using a line-of-sight QMS during the growth of thin films using MBE, a few noteworthy are: quantitative study of nucleation phenomena by monitoring the desorption process,[87–89] compositional measurements during growth,[90–94] growth rate, and surface temperature determination[95]. In addition to the compositional measurements during growth, Evans *et al.*,[91] successfully used a feedback loop between the QMS and substrate heater to achieve realtime control over the composition during the growth.

Though various works deal with the applications of QMS in the epitaxial growth of thin films, no details are provided on how to eliminate the time dependent background signals, and the contribution of desorption from the substrate holder. In the following, a description on how to tune the mass spectrometer to obtain high signal to noise ratio, exclusion of substrate contribution on desorption, monitoring time dependent background signals, determining the growth regime of the particular alloy is given. Calibration of the QMS for compositional analysis will be discussed later in section 4.5.1.

3.6.1 Experimental Details

Figure 3.4 shows a schematic diagram of an MBE system hosting a line-of-sight QMS and a RHEED. Atomic beam from the effusion cells upon impinging onto the substrate undergo various surface mechanisms such as adsorption, surface migration or desorption. A part of the desorbed atomic/molecular species from the substrate are detected by the QMS. The surface quality can be simultaneously monitored by the RHEED, as the QMS does not obstruct the RHEED view.

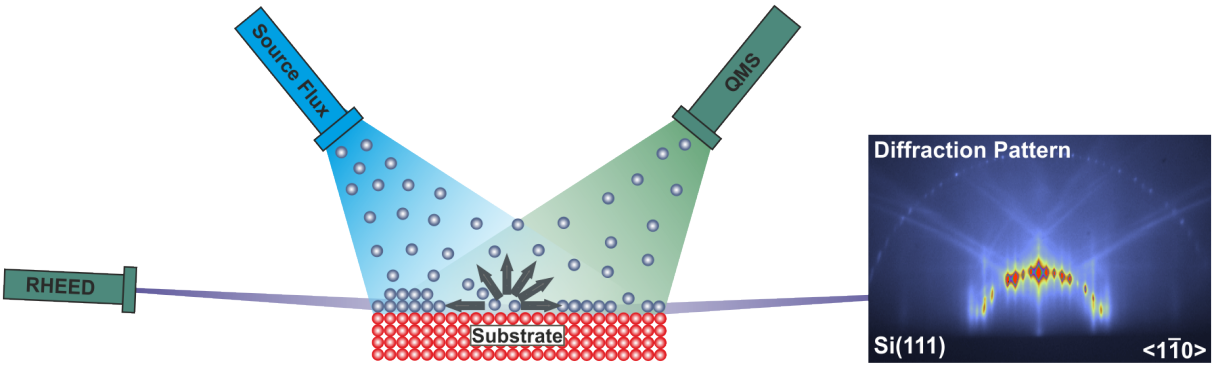

Figure 3.4: Schematic diagram of a line-of-sight QMS

A Hiden HAL IV line-of-sight QMS capable of scanning atomic/molecular species with masses upto 500 amu is installed at one of the vacant source/cell ports of the MBE chamber. The QMS is mounted in such a way that the quadrupole is directly facing the sample surface. The

quadrupole is 110 mm long, has a 5 mm circular opening and is placed 300 mm away from the sample surface (see figure 3.6). Similar to the effusion cells, the quadrupole is inclined at an angle of 20° from the surface normal to the substrate. QMS is capable of scanning simultaneously different atomic/molecular species using multiple ion detection mode with a resolution of up to 0.01 amu.

Design Considerations

It is important to perfectly align both source and filter to obtain the highest sensitivity. In the case of misaligned source and filter, the sensitivity decreases and to restore the same accuracy, higher ion energy is required, which in turn reduces the mass resolution[96,97]. The sensitivity reduces by up to 2 orders of magnitude for a tilting of the main axis by 1.5ï¿½ with respect to the source. Mao et al.,[96] reported that misalignment of the quadrupole rods cause distortion of electric fields which in turn results in the splitting of peaks. Hence, extreme care was taken to have a perfect alignment of the quadrupole filter with the source. Longer the mass analyser, more is the number of RF oscillations that the ions undergo, and greater is the resolution[98]. So, high resolution mass spectrometric studies require long mass analysers.

Tuning to Specific Needs

Most of the atomic/molecular species that we monitor in the present work, such as Ge, Sb, Te have more than one stable isotope. Hence scanning with a very high resolution results in a weak signal and low signal to noise ratio. To avoid this, low mass resolution was selected for the growth experiments as it is capable of scanning the nearby isotopes, thus increasing the signal strength and better signal to noise ratio. However one must be cautious in lowering the resolution, while working on atoms that are close to each other in atomic mass. In those cases, it is necessary to work at a better resolution to avoid mixing up signals from the neighbouring atomic species. The dwell time (the time to acquire a single point in scan) and settle time (the time to allow the electronics to settle before the start of the scan) are set at 160 ms and 40 ms respectively. Longer dwell time is required to reduce the measurement noise in the observed signal.

Another important factor influencing the mass spectrometer is the sensitivty, which depends on various factors such as the rate at which positive ions are created, alignment of the source and filter,[96] ionization energy[98] and contamination over time[99]. For a particular species of atom at constant ion energy, as the sensitivity of the atomic species increases, the mass resolution decreases[96,98]. As a function of change in ion energy, the sensitivity changes are relatively high when compared to the change in resolution. Mao et al.,[96] show that the stability of the instrument can be maximised by working at higher ion energy to have higher sensitivity but lower resolution. The sensitivity is greatly affected by the contaminaton of the filter over time and the effect is greater at lower ion energies[99]. Hence Austin et al.,[99] proposed for long term stability of the instrument, the following: (1) operation at high ion energy, or (2) cleaning the filter assembly or (3) switching of the filament when not in use. To avoid the drifts in sensitivity we switch off the filament when not in use. It is necessary to switch it on a couple of hours before the start of the growth experiments to outgas the deposited material on the filament.

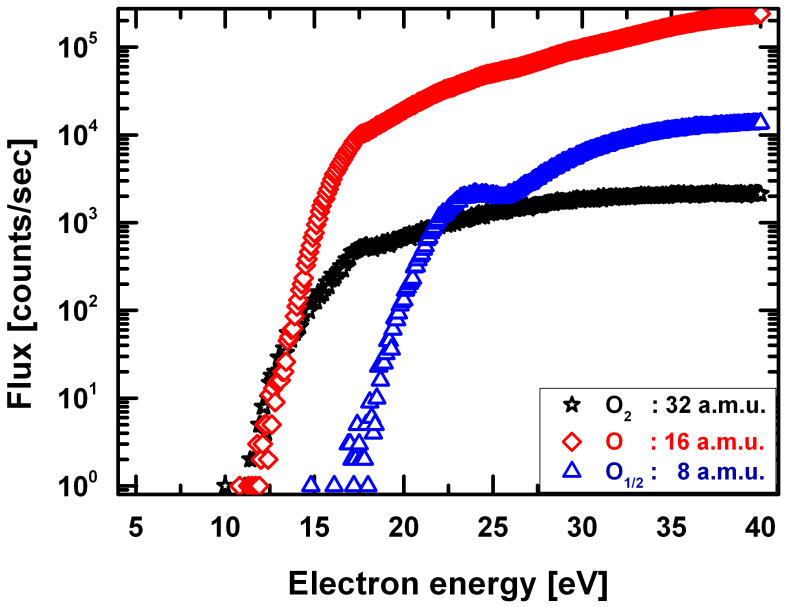

Figure 3.5: Ion yield as a function of electron energy. Multiple ionisation occurs at higher electron energies

Figure 3.5 shows the flux observed by the QMS as a function of change in supplied electron energy. Ion yield increases as a function of electron energy. No signal is observed for electron energies lower than 12 eV. However, at higher electron energies fragmentation occurs and we could observe atomic oxygen at 16 amu and doubly ionised oxygen at 8 amu. Typically the mass spectrometer measures the mass over charge (m/Z) ratio. For a doubly ionised atom the charge is 2 and hence the mass spectrometer will detect the ion only at half its mass value. At higher electron energies, multiple ionisation becomes more probable. The problem of multiple ionsiation of atoms should be avoided by carefully tuning the supplied electron energy. This critical value for fragmentation is different for different atoms/molecules and must be selected such that the ion yield is not compromised much, when scanning multiple atomic species.

3.6.2 Signal from Substrate Holder and its Exclusion

The quadrupole monitors an area of 816 mm^2, excluding the 20° angle from the surface normal which necessarily increases the effective area by 1.06 times (865 mm^2) (see figure 3.6). For our growth experiments (20×20) mm^2 wafers with a surface area of 400 mm^2 are used. This means that the quadrupole views a larger (almost twice) area. So, a majority of the information that comes from the species desorbing from the substrate holder might complicate the interpretation of the obtained data. It is thus necessary to eliminate the signals originating at the substrate holder from the one arising from the substrate.

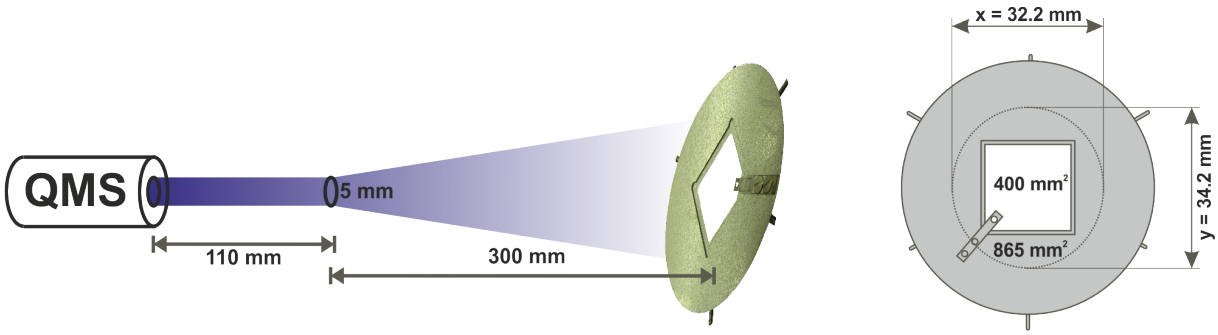

Figure 3.6: Sketch depicting the dimensions of the QMS with substrate (left) and the QMS viewing area on the substrate (right)

To discriminate between substrate and substrate holder signal, following experiment was performed. An amorphous thin film of GeTe was deposited and subsequently desorbed by ramping up the substrate temperature at 0.1 ï¿½C/sec up to 500 ï¿½C. As observed from Figure 3.7 (a), two peaks well separated by about 200 °C can be clearly seen. Subsequently, an amorphous thin film was deposited on a dummy substrate placed on the substrate holder. Later the substrate was replaced with a fresh substrate without any film on top, while the substrate holder was not changed. During annealing only the high temperature peak appears (see Figure 3.7 (b)), which thus corresponds to desorption from the substrate holder. This ensures that the mass spectrometer observes only the flux arising from the substrate in the temperature regime (200-250 ï¿½C) at which the crystalline thin films are grown.

3.6.3 Background Signal Elimination

Different atomic species have different background signal in the chamber. The background pressure is not constant and keeps changing depending on the liquid nitrogen flow around the growth chamber, the temperature of the cells, substrate temperature and the flux provided. The quadrupole monitors both the signal from the substrate and the background. If the quadrupole is intended to be used for desorption stuides or for quantitative analysis, it is necessary to decouple substrate and background signals. To overcome this problem we use a shutter placed in front of the QMS, so that when the shutter is closed only the background signal is observed and when opened both the contribution from the substrate and background are seen. Thus by shuttering the QMS every few seconds, the real time change in background flux or the amount of material that is desorbed from the substrate are alternately monitored. The difference between these two signals gives the amount of material that is desorbed from the substrate excluding the background contribution.

Figure 3.8 shows the advantages of shuttering the mass spectrometer. We used a buffer grown GaSb substrate for desorption measurements shown in Figure 3.8 (a)-(c). The temperature ramp was done at 0.1°C/s.

In Figure 3.8 (a), Sb desorption is clearly observed while the background pressure of antimony remains constant throughout the temperature ramp (Case 1: desorption with constant back-

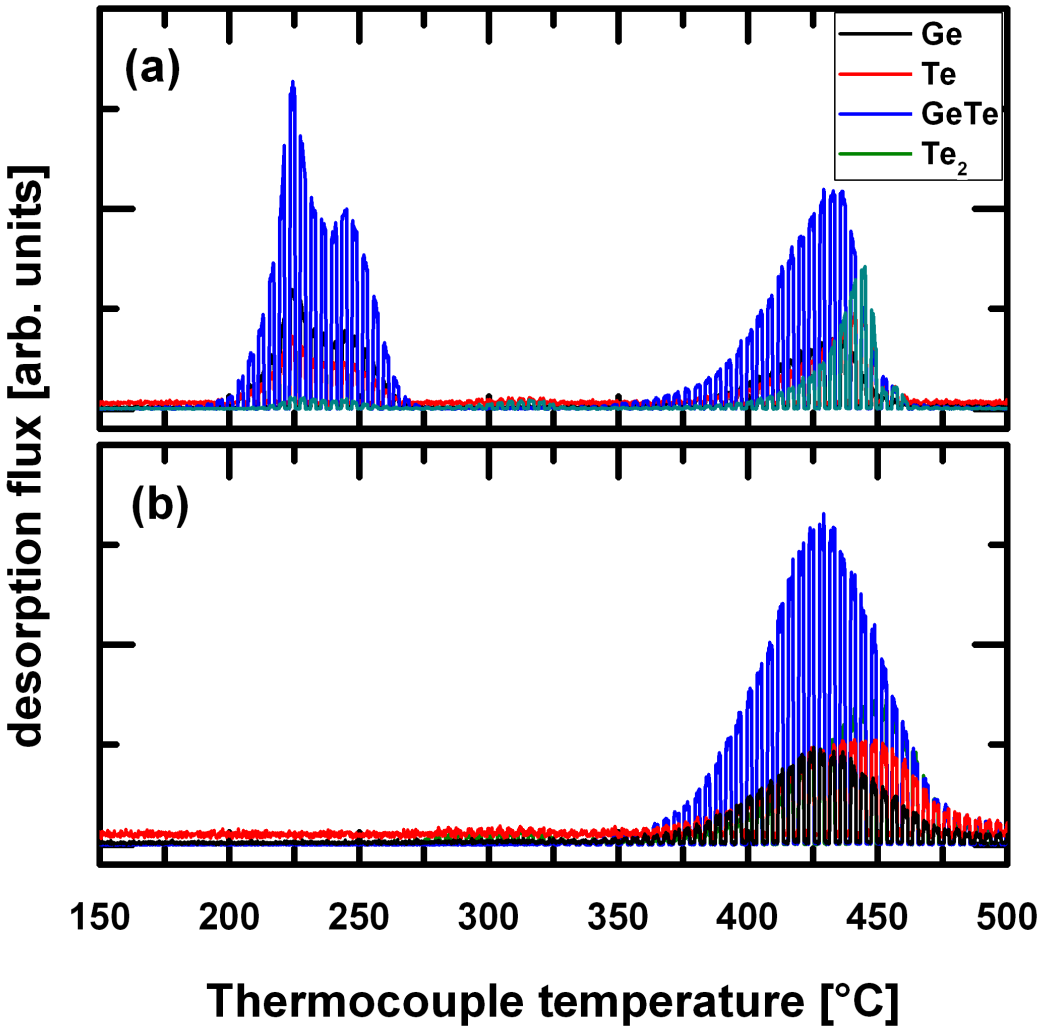

Figure 3.7: Desorption studies: (a) desorption from both substrate and substrate holder and (b) from substrate holder only

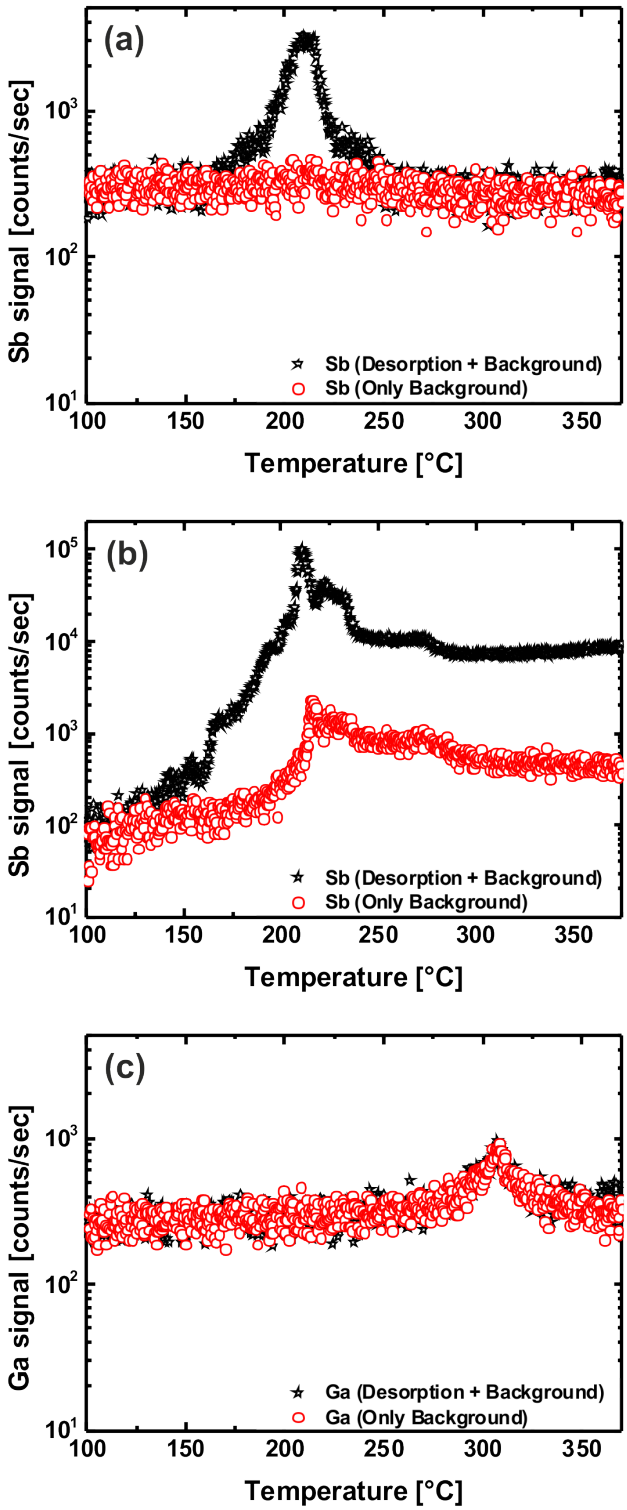

Figure 3.8: Desorption and background signals from a GaSb film. (a) Sb desorption, (b) Sb desorption in the presence of Sb flux, and (c) Ga desorption

ground signal). Thus the desorption characteristics of a particular species can be determined and if calibrated from the standard desorption temperature for a particular atomic species, the temperature offset of the thermocouple can be found.

Figure 3.8 (b) shows the same desorption characteristics in the presence of a constant supply of Sb flux. The background signal also increases with temeprature during heating (Case 2: desorption with temperature dependent change in background signal).

Figure 3.8 (c) shows the Ga signal observed during desorption. The background and the (desorption+background) signal increases similar to one another and the observed peak in desorption is not really a peak, but rather a change in background signal at that temperature (Case 3: No desorption with change in background signal).

In the last two cases, if a constant background signal is assumed, the extrapolation of the final data would lead to erroneous results. Whether using the mass spectrometer for desorption studies or as quantitative analysis tool, the above measurements show that it is really necessary to monitor the background signal from time to time to record its fluctuations. In our custom built MBE, we use QMS as a substitute for BEP (beam equivalent pressure). In fact, it is particularly advantageous in determining the stability of the effusion cells.

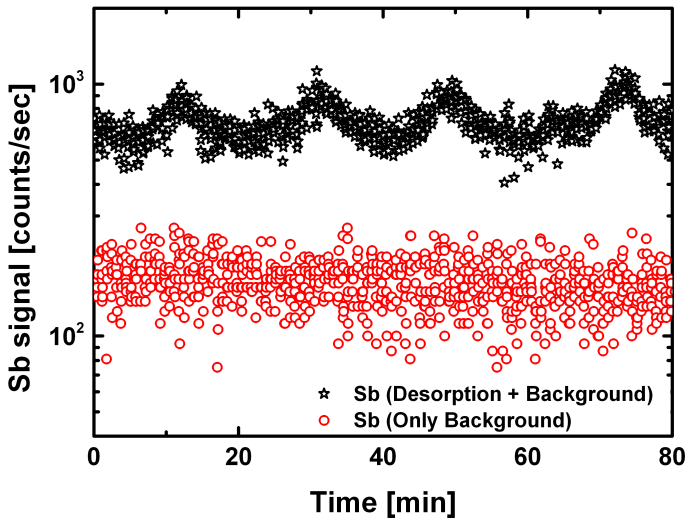

Figure 3.9: Desorption of Sb during Sb deposition on Si(111) substrate. The flux modulations are observed every 20-22 minutes

Sometimes, the effusion cells are not stable and the fluxes might fluctuate with time. Modulations in supplied flux might seriously affect the epitaxial growth in certain material systems. In our system, Sb flux fluctuations even within a short time range are observed. Figure 3.9 shows the supplied Sb flux, which is completely desorbed upon impinging on Si(111) at 300 °C, where the sticking of Sb on to the substrate is negligible. The desorbing flux, which is indeed a factor of the flux provided by the effusion cell, fluctuates every 20-22 minutes. As the

fluctuation is not observed in the background signal, and the sticking is found to be negligible for Sb at this substrate temperature. The change in desorbing flux can only be attributed to the fluctuations in the effusion cell flux. This is useful to know in the case of epitaxial growth where the fluctuations in the source flux might seriously affect the quality of the films.

3.7 X-ray Diffraction

XRD is a powerful non-destructive technique for structural characterization of materials as the interatomic distances are comparable to the wavelength of x-ray photons. X-rays are electromagnetic radiation with an electric field vector oscillating rapidly (3×10^{16}-3×10^{19} Hz) and upon interaction with an atom, they can either remove a weakly bound electron by means of photoelectric absorption or lead to scattering effects. The scattering can be elastic (Thomson scattering) or inelastic (Compton scattering). In XRD we deal with the elastic scattering of x-rays. In contrast to electron diffraction, x-rays weakly interact with matter and the problem of multiple scattering effects can be neglected in the case where the observed crystal is not perfect. Hence in most of the cases (non ideal), a simple kinematical approximation is enough to decribe the scattering.

Crystals possess long range atomic ordering and can be considered as a three dimensional grating, which produce interference effects, when x-rays pass through. Consider an incoming x-ray beam with a wavevector $\mathbf{k_i}$ incident on a crystal with its tip on the origin of the reciprocal space. Draw a sphere as shown in figure 3.10 (a)[1] with the origin of the wave vector as the center and $\mathbf{k_i}$ as the radius. This is the Ewald sphere and according to conservation of momentum, diffraction will not occur outside this sphere. The incident beam scatters with a wave vector $\mathbf{k_f}$ at an angle 2θ to the incident beam. From the law of conservation of momentum $\mathbf{k_i}$=$\mathbf{k_f}$+$\mathbf{G_{hkl}}$. All points in the reciprocal space intersecting the Ewald sphere satisfy the condition for elastic scattering. Using simple trignometric relation from the figure 3.10, we obtain

$$\sin\theta = \frac{|\mathbf{G_{hkl}}|/2}{|\mathbf{k_i}|} \tag{3.2}$$

From Pythagoras theorem (for a cubic crystal), we can write

$$|\mathbf{g}| = \left(\frac{4\pi^2}{d^2}h^2 + \frac{4\pi^2}{d^2}k^2 + \frac{4\pi^2}{d^2}l^2\right)^{1/2} = \frac{2\pi}{d}(h^2+k^2+l^2)^{1/2} \tag{3.3}$$

where $2\pi/d$ is the reciprocal lattice plane spacing. The wave vector $\mathbf{k_i} = 2\pi/\lambda$, so we can write,

$$\sin\theta = \frac{\lambda}{2d}(h^2+k^2+l^2)^{1/2} \tag{3.4}$$

which gives the Bragg condition for diffraction:

$$2d\sin\theta = n\lambda \tag{3.5}$$

[1]Reproduced from the book: Surface Analysis: The Principal Techniques, 2nd Edition, John Wiley & Sons Ltd [100]

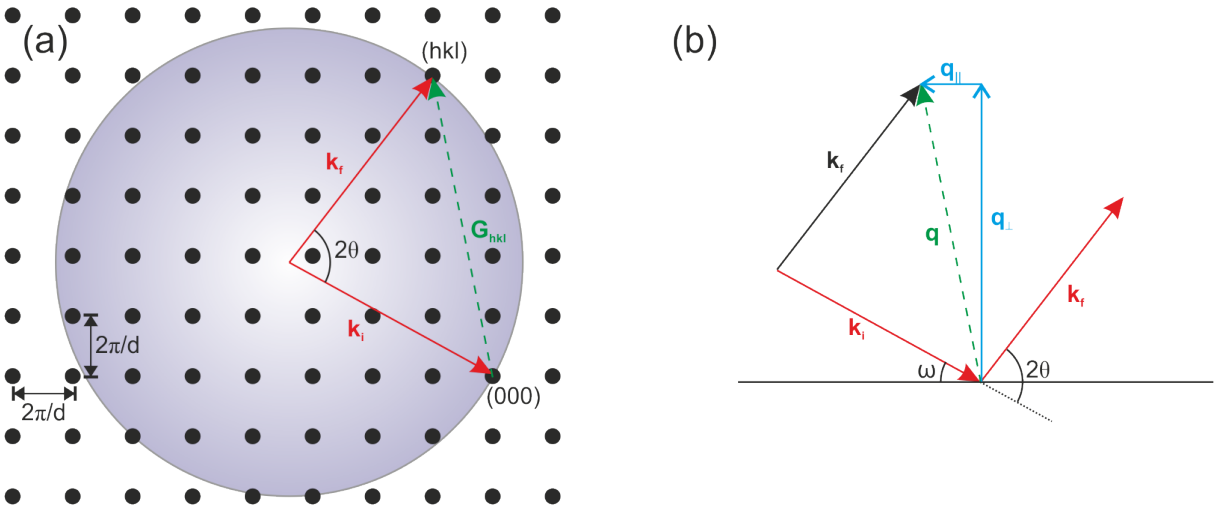

Figure 3.10: (a) Ewald sphere for a simple cube with interplanar spacing 'd'. (b) $\mathbf{k_i}$ and $\mathbf{k_f}$ are the incident and scattered wavevectors respectively, ω is the incident angle and 2θ is the angle of diffraction, $\mathbf{q}$ is the momentum transfer

where n is the order of diffraction. In a coplanar geometry, $\mathbf{q}$ is the resultant of the momentum transfer along parallel ($\mathbf{q}_{||}$) and perpendicular directions ($\mathbf{q}_{\perp}$). From the figure 3.10 (b), we can write ($\mathbf{q}_{||}$) and ($\mathbf{q}_{\perp}$) in terms of simple trignometric identities as follows,

$$\mathbf{q}_{||} = \mathbf{k_f}\cos(2\theta - \omega) - \mathbf{k_i}\cos\omega \tag{3.6}$$

$$\mathbf{q}_{\perp} = \mathbf{k_f}\sin(2\theta - \omega) + \mathbf{k_i}\sin\omega \tag{3.7}$$

Since all the points intersecting the Ewald sphere satisfy the condition of elastic scattering, then $|\mathbf{k_i}| = |\mathbf{k_f}| = \mathbf{k} = 2\pi/\lambda$. The above equation can be simplified as

$$\mathbf{q}_{||} = 2\mathbf{k}\sin\theta\sin(\omega - \theta) \tag{3.8}$$

$$\mathbf{q}_{\perp} = 2\mathbf{k}\sin\theta\cos(\omega - \theta) \tag{3.9}$$

3.7.1 Grazing Incidence X-ray Diffraction

Though x-rays are used for probing bulk crystals due to their high penetration depth, by carefully selecting the incidence angle, the penetration depth can be reduced and in fact at grazing incidence geometry, the x-rays can penetrate only upto few nanometres into the crystal and can act as a surface sensitive characterization tool. The idea of GIXRD was first proposed by Marra et al.,[101] based on the concept of total external reflection. For most materials, the refractive

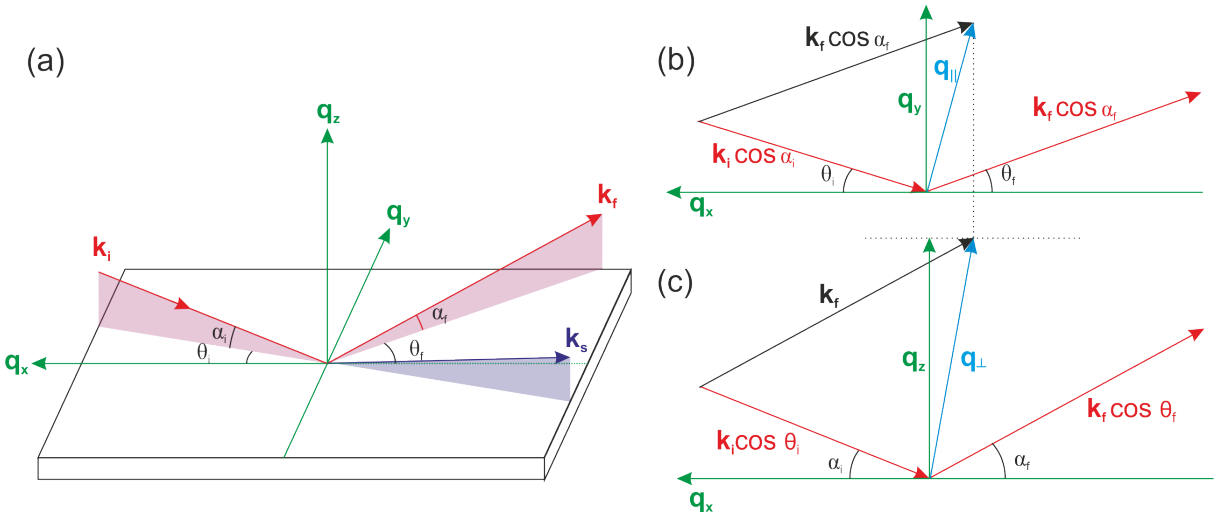

Figure 3.11: Sketch of the GID geometry. (a) 3D view : α_i and α_f are the incident and scattering angles respectively. θ_i and θ_f are the corresponding angles in-plane. (b) top view (x-y plane) and (c) side view (x-z plane)

index (n) of x-ray is less than unity and is given by

$$n = 1 - \delta + i\beta \tag{3.10}$$

where, $2\delta = \sin^2 \alpha_c$ and $\beta = \nu\lambda/4\pi$, α_c is the critical angle for total external reflection and ν is the linear absorption coefficient. Total external reflection is possible as long as the incident angle (α_i) is less than the critical angle (α_c). Under this condition, only a rapidly decaying evanescent wave passes through the surface and we observe a specularly reflected beam. In grazing incidence configuration, diffraction occurs at planes perpendicular to the sample surface. Figure 3.11 shows the scattering geometry. X-ray beam with wave vector k_i incident on the surface at grazing angle (α_i) produces a specularly reflected beam k_s. By rotating the crystal around surface normal, the planes perpendicular to the surface that satisfy the Bragg condition can be found. At an angle of α_f with respect to the sample surface, the scattered beam with wave vector k_f emerges.

From figure 3.11 (b), using trigonometric relations, the magnitude of the wave vector in different directions is written as follows,

$$q_x = \mathbf{k}(\cos\alpha_f \cos\theta_f - \cos\alpha_i \cos\theta_i) \tag{3.11}$$

$$q_y = \mathbf{k}(\cos\alpha_f \sin\theta_f - \cos\alpha_i \sin\theta_i) \tag{3.12}$$

$$q_z = \mathbf{k}(\sin\alpha_i + \sin\alpha_f) \tag{3.13}$$

In the case of two dimensional lattice or surface diffraction, a symmetry break appears along

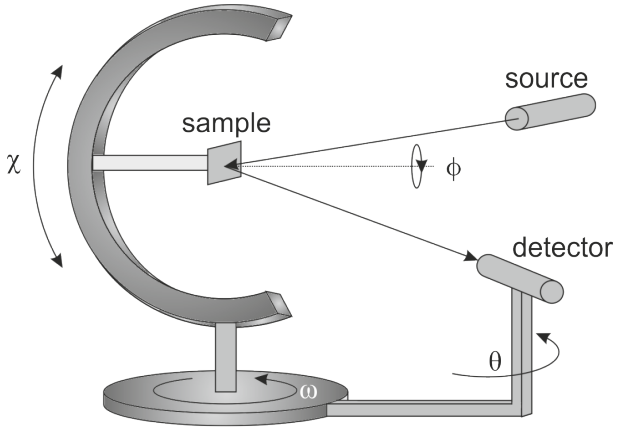

Figure 3.12: Schematic diagram of a four circle diffractometer

the z-direction at the surface and the corresponding reciprocal lattice has infinitely long rods similar to the case of RHEED pattern observed on an atomically smooth surface. In the GID configuration, it is difficult to experimentally set zero q_z, as it requires the incident and diffracted beam to be parallel to each other. In this case, usually the diffraction peaks can be found close to non-zero values of q_z along the CTR.

3.7.2 Four Circle Diffractometer

Most of the specular $\omega - 2\theta$ scans and reflectivity measurements are performed using the Panalytical X'pert 4-circle diffractometer. It has 4 degrees of freedom, 3 for sample orientation (ω, ϕ, χ) and one for detector orientation (θ). Figure 3.12 shows the schematic diagram in which the source is fixed. The sample alignment can be performed by x, y and z movements (not shown in the schematic diagram). The x-ray source has a photon energy of 8.048 keV and produces copper K_{α_1} radiation of wavelength $\lambda = 1.54$ Å. Specular $\omega - 2\theta$ scans help to find the preferred out-of-plane orientation of the grown film. The diffraction pattern is obtained by varying the incident angle by ω $(= \theta)$ and the scattering angle by 2θ. The scattering vector (q_z) in a $\omega - 2\theta$ scan is always parallel to the surface normal. Prior to any measurements, the substrate reflection is aligned to the theoretical bulk value to account for the instrumental offsets.

X-ray reflectivity (XRR) is performed to study the thickness, density, roughness and interface roughness of the epilayer or amorphous films. It is basically a $\omega - 2\theta$ scan performed at low incident angles. At very low scattering vector (q_z) the sample which is at half the beam intensity, will have lower footprint of the beam. With increasing scattering vector the footprint of the beam on the sample increases upto a critical angle (∼0.1-0.3ï¿½), where a plateau is observed due to total external reflection. This critical scattering angle is dependent on the density of the film. Above the crictical angle, x-ray start penetrating inside the film and for an ideal surface, the reflectivity of the x-rays is strongly dependent on the scattering vector by a relation $I_{ref} \propto q_z^{-4}$. In this region, if the path difference between the x-rays reflecting from the surface and interface are $n\pi$ (where n is odd), they produce an intensity minima. These successive intensitiy minima

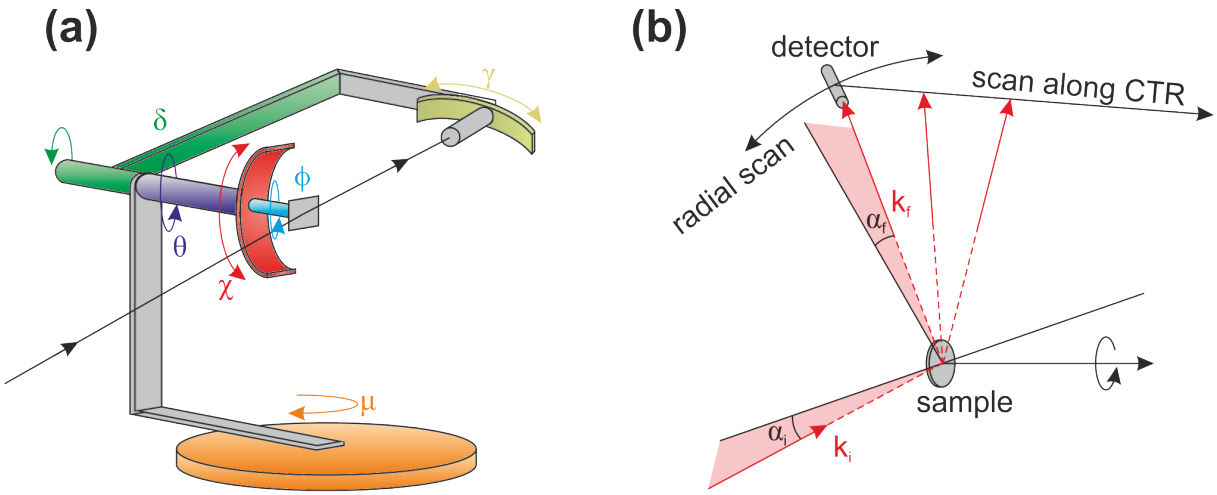

Figure 3.13: (a) Schematic diagram of a six circle diffractometer showing the six rotation circles. (b) GID geometry depicting the detector movements for in-plane and out-of-plane scans. k_i and k_f are the incident and scattered wave vectors and α_i and α_f are their corresponding angles with respect to the sample surface

and maxima are usually called as Kiessig fringes. The distance between two successive minima is inversely proportional to the film thickness. The amplitude of the fringes is proportional to the density difference between the film and substrate. At larger incident angles, the intensity of the interference maxima reduces as the surface roughness increases.

Reciprocal space maps (RSM) are performed by a combination of ω scan (rocking curve) around the Bragg peak of interest and subsequent $\omega - 2\theta$ scan to construct a RSM in Q space around the Bragg peak of interest. χ rotation tilts the sample perpendicular to the ω rotation axis. Fixing the epilayer at a particular Bragg peak, a combination of ϕ (0-360ï¿½) and χ (0-90ï¿½) movement can be performed to obtain stereographic projections or pole figure for that particular Bragg reflection. Pole figures give the orientation distribution of a family of netplanes having the same d-spacing.

3.7.3 Six Circle Diffractometer

The MBE chamber is mounted on a six circle diffractometer placed in the path of the PHARAO synchrotron beamline at BESSY II. The diffractometer has 6 degrees of freedom: three for the sample (θ, χ, ϕ), two for the detector (δ, γ) and one for the rotation (μ) of the entire diffractometer. A schematic diagram of the six circle diffractometer is shown in the figure 3.13. The sample is aligned such that the surface normal is parallel to the horizontal axis of the diffractometer. This is achieved using a laser reflected from the substrate surface and projected on a screen. The aim is to keep the laser beam on the screen at the same point by aligning the ϕ and χ circles (which are in turn mounted on the θ stage). Once the sample surface is perpendicular to the axis of the θ circle, ϕ and χ motors are fixed so that θ rotation will not alter the angle between the sample surface and x-ray beam. The γ detector arm combines translation and rotation

Circle	Range	Resolution
μ	0ï¿½ - 45ï¿½	0.02ï¿½
χ	-3ï¿½ - +3ï¿½	0.001ï¿½
ϕ	0ï¿½ - 360ï¿½	0.001ï¿½
θ	0ï¿½ - 360ï¿½	0.001ï¿½
δ	0ï¿½ - 130ï¿½	0.001ï¿½
γ	0ï¿½ - 45ï¿½	0.001ï¿½

Table 3.1: Sample and detector circles along with their range and resolution

movements in order to always keep the detector facing the diffracted beam. The γ movement is used for performing out-of-plane measurements along the CTR with large momentum transfer perpendicular to the surface and is mounted on the δ arm of the diffractometer. The δ circle can be rotated perpendicular to the sample surface normal to perform azimuthal rotations. The angular range of all the six rotation circles with the corresponding resolution is given in table 3.1.

Figure 3.13 (b) shows the schematic diagram of the detector movement along in-plane and out-of-plane scans. Detailed report about the integration of the MBE system with the diffractometer for *in-situ* x-ray studies is given elsewhere[102].

3.7.4 PHARAO U125/2-KMC Beamline

The idea of synchrotron was first proposed in 1945[103,104] and within a span of two years the first synchrotron was built[105]. Charged sub-atomic particles accelerated to relativistic speeds in circular orbits of the synchrotron emit high fluence photon over a broad range of the electromagnetic spectrum, usually called synchrotron radiation. They are highly collimated, have wide spectral range from extreme terahertz to hard x-rays.

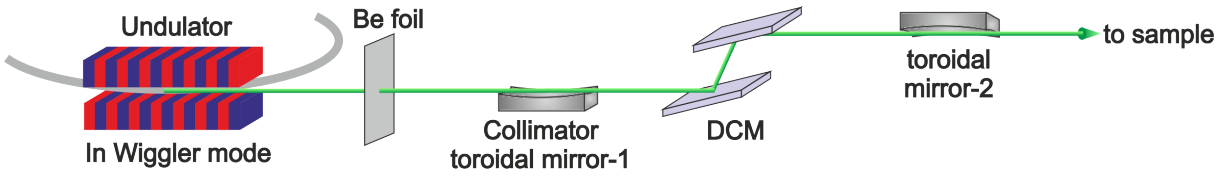

Figure 3.14: Schematic diagram of the PHARAO beamline

Most of the GIXRD experiments presented in this thesis were performed at the PHARAO beamline of the synchrotron at BESSY II, Helmholtz Zentrum, Berlin, which is a third generation synchrotron operating at an energy of 1.7 GeV. The PHARAO beamline is also called as U125/2-KMC beamline. The letter 'U' represents that the x-ray source arises from an undulator and KMC refers to crystal monochromator (Kristallmonochromator). The undulator consists of magnets arranged in 32 periods each having a length of 125 mm and the gap between the magnets can be varied from 100 mm to 15.7 mm. For GIXRD studies, the undulator is operated in a wiggler mode. A wiggler can be considered as a series of several bending magnets that

forces the electrons to travel in a sinusoidal path by the application of a periodic magnetic field. The intensity increases with the number of dipole periods. Wigglers are used where high energy photons are required, while undulators are preferred for its high brightness at specific wavelengths. Figure 3.14 shows the schematic diagram of our beamline. A water cooled beryllium foil is used to absorb the low energy part of the spectrum. The first toroidal mirror, which is a Si substrate coated with Rh reflecting layer is used to collimate the beam before passing through the double crystal monochromator (DCM). The DCM consits of two flat Si(111) crystals, and by turning to specific angles, it monochromatises the incoming broad light source. Energy ranges between 6 keV and 12 keV can be obtained. The energy resolution of the monochromator is about 7×10^{-4}. The monochromatic beam from the DCM is focussed into the center of the diffractometer using a second toroidal mirror. The toroidal mirror produces a spot size of 1 mm^2 on the sample and typical beam flux of about 10^9 photons/sec. Further details about the beamline can be found here[102].

4 Epitaxial Growth of GeTe

GeTe is considered as a prime alternative to GST in phase change memory devices due to its better electrical contrast between the two phases, faster switching and longer data retentivity at higher temperatures[73]. Being a binary material and analagous to GST in terms of switching properties, it is widely studied to understand the switching mechanism of GST based ternary alloys. From the growth point of view, the complexities involved in the growth of ternary GST alloy pose a serious challenge and hence understanding the growth mechanism of binary alloy is trivial. In this chapter we report the MBE growth of GeTe.

4.1 Experimental Details

$(20 \times 20)mm^2$ sized, p-type (B-doped, resistivity of 1-10 Ωcm) Si(111) and Si(001) substrates with a miscut of $\pm 0.03^\circ$ were wet cleaned and loaded into the MBE chamber. Elemental Ge and Te are loaded in dual-filament effusion cells. For the growth experiments discussed here, the base/hotlip temperatures of Ge and Te were respectively 1098/1118 °C and 345/483 °C. The corresponding fluxes were estimated by measuring with *ex-situ* XRR the thickness of amorphous Ge and Te films, deposited at room temperature to ensure complete sticking of the impinging species. Ge and Te growth rates were found to be ∼0.23 and ∼0.58 nm/min. This flux ratio was selected, so as not to interrupt the day-to-day growth of GST films, which uses a similar flux ratio for $Ge_2Sb_2Te_5$ deposition. Due to the complexities involved in determining the day-to-day flux fluctuations without a beam flux monitor, we preferred the aforementioned strategy. The layers were fabricated under UHV conditions with a chamber pressure of less than 1×10^{-9} *mbar*. A line-of-sight QMS and RHEED were used to monitor the desorbing species and surface morphology during the growth.

4.2 Germanium Etching by Tellurium

Before proceeding to discuss about the epitaxial growth of GeTe, it is better to start understanding the interactions of Ge and Te atoms with one another. Epitaxial growth is performed at substrate temperatures (T_{sub}) high enough to ensure good crystalline quality of the deposited film. This is achieved if the impinging atoms have enough surface mobility to arrange on energetically favourable lattice positions. Together with surface diffusion mechanisms, also adsorption or desorption of the impinging atoms is possible. We use a line-of-sight QMS to monitor the desorbing atomic/molecular species. During the epitaxial growth of GeTe, the following species are observed *via* QMS: Ge, Te, GeTe and Te_2. Within the scanning limit (500 amu) of the mass spectrometer, no other molecular (homo- or heteromolecular) species such as Ge_2, Ge_3, Ge_2Te, $GeTe_2$, Ge_3, Te_3 or Ge_2Te_2 can be detected. This shows the ability of the Ge and Te

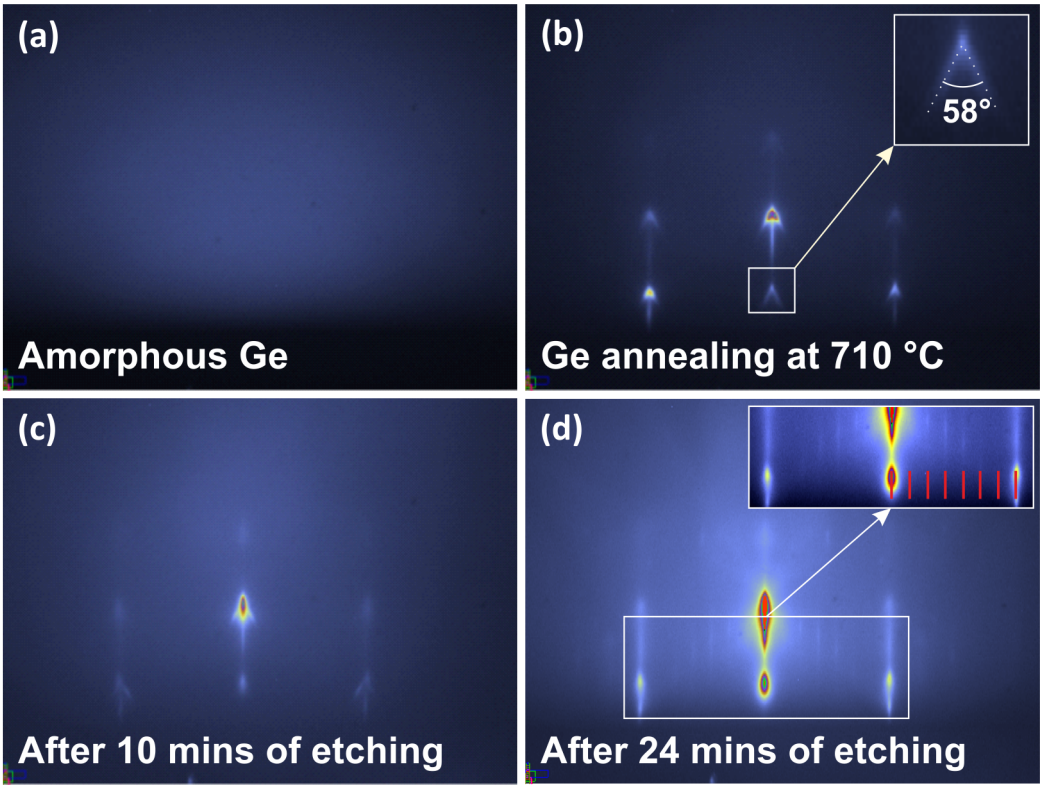

Figure 4.1: (a) RHEED pattern acquired after (a) amorphous Ge layer growth, (b) annealing at 710 °C (chevron patterns are observed with an angle of 58±3°), (c) 10 mins of etching and (d) 24 mins of etching (Si(111)-7 × 7 reconstruction start to reappear)

atoms to form GeTe heteromolecule and its stability upon desorption. The tendency of Ge to interact with Te to form stable heteromolecular bonds can be harnessed in etching away the deposited Ge film. Ge has a very low vapour pressure[106] compared to Te[107,108], thus Ge thin film is comparatively stable at temperatures where Te sticking is almost negligible. At these temperatures where the Ge atoms do not desorb on their own, it is possible to etch away the stable Ge atomic species by providing a flux of Te. If this is possible, it might be useful for selective growth/etching experiments. To prove this assumption, we performed the following experiment. A thin amorphous layer of Ge was deposited at room temperature for 60 minutes. There are two reasons why we preferred to grow amorphous films (though the experiment might work equally well with crystalline Ge layers): (1) at room temperatures the sticking coefficient of Ge on Si is unity and hence one can quantitatively determine the amount of deposited material, and (2) if in case, we could etch away the deposited Ge film using Te, then from the flux supplied and time for etching away the complete film, one can find a correlation between the time taken to etch and the supplied flux.

For our growth and etching experiment a flux ratio of Ge:Te::2:5 was set. For 60 minutes of growth duration, 13.8 nm thick amorphous Ge film was deposited at a growth rate of 0.23 nm/min. As discussed earlier, to obtain an effective etching T_{sub} has to be ramped up to temperatures where Te does not stick on to the surface and Ge does not desorb on its own. Concurrently RHEED and QMS were used to monitor the changes in surface quality and desorbing species from the substrate. Figure 4.1 (a) shows a diffuse RHEED pattern, typical of an amorphous layer obtained after 60 minutes of growth. During the temperature ramp up at around 350 °C, the surface turns from amorphous to crystalline. However there is no desorption of Ge species even at 710 °C. At this temperature the ramping was stopped and the corresponding RHEED picture of the annealed Ge layer is shown in figure 4.1 (b). It shows a chevron (v-shaped) pattern with an half angle of 29° (±1.5°) from the [111] direction. These chevron patterns are generally attributed to the facet planes[109–112]. So, it is possible to conclude that the annealing process lead to roughening of the surface.

Figure 4.2 shows the QMS signal observed for Ge, Te, GeTe and Te_2 upon Te shutter opening. The origin of the time axis corresponds to the opening of the Te shutter. The graph 4.2 can be divided into four regions (I-IV). At time t=0 (represented by region I), the QMS signal of all the species increases, however the GeTe desorption signal increases by a factor of four with respect to others, indicating strong formation of GeTe bonds and subsequent desorption. The increase of all the signals at t=0 might be attributed to a sudden surface reaction between the deposited Ge and the incoming Te. Further, the rapid decrease also indicates that the reaction rate also decreases, pointing to a stabilization of the surface temperature after the initial rise caused by effusion cell opening.

In region (II), the signals keep decreasing with two different slopes for about 20 minutes. The first slope accounts for a stronger desorption rate, whereas the second slope corresponds to a slower rate and this is an indication that the reaction almost stabilizes and proceeds in a steady state. In this region, the GeTe signal is almost three times higher than the other species indicating preferred formation of GeTe, with small amounts of Ge, Te and Te_2 desorption. Figure 4.1 (c) shows the RHEED pattern acquired after 10 minutes of etching. The Ge crystalline pattern is still visible on the surface.

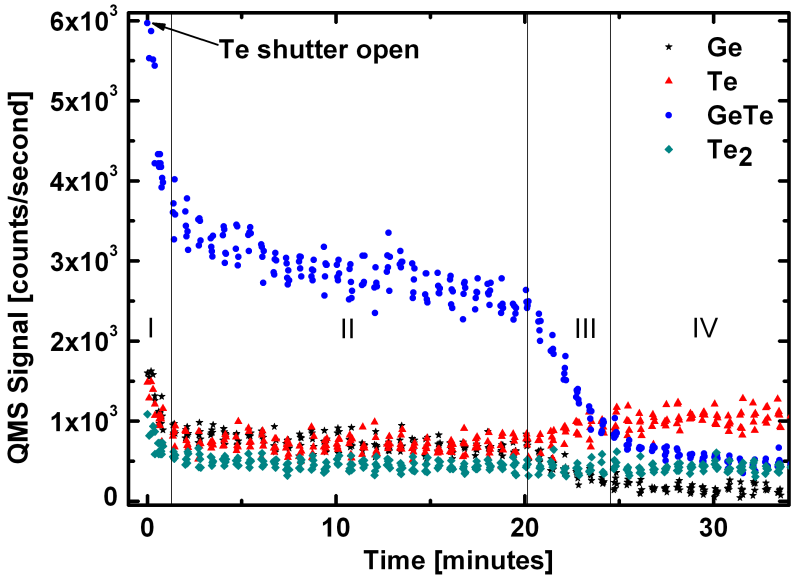

Figure 4.2: Etching time versus mass spectrometer signal of various desorbed species namely Ge, Te, GeTe and Te_2

In the third region (III), the GeTe and Ge desorption signals strongly decrease, whereas the Te signal increases. The reason for the decrease of the signals is that there are not enough Ge atoms left on the surface for Te atoms to interact. Hence the Ge, GeTe signals drop, while the unreacted Te atoms desorb. The decrease in Ge, GeTe signals and increase in Te, Te_2 crosses at 24 minutes which correponds to two-fifth of the Ge deposition time. Interestingly the Ge deposition flux to the supplied Te flux is in the ratio 2:5. This indicates that with two and a half times the Te flux, the Ge layer is etched away almost completely with in two-fifth of the Ge deposition time. This quantitative etching data result is very helpful to calibrate the QMS for *in-situ* compositional analysis which will be discussed in section 4.5.1. At this point, the RHEED pattern shows faint signals of Si(111)-7×7 reconstruction (see figure 4.1 (d)). However, the intensity of the reconstruction signal continues to increase over time, before it reaches a steady state at around 30 minutes. In the region (IV), a weak GeTe signal is monitored, indicating that it takes a longer time to etch away the Ge layer completely.

4.3 Growth of GeTe

The etching studies also indicate that Ge can act as a limiting flux for the growth of GeTe when an oversupply of Te is present. At growth temperatures the Te atoms in excess, which do not find a Ge atom on the surface to form stable GeTe, desorb. Hence we used an overpressure of Te and Ge:Te flux ratio of 2:5 for the growth of GeTe thin films. Prior to growth studies, well cleaned Si substrates are chosen. The substrate preparation is already discussed in 3.4.

Initial Si surfaces show well defined RHEED reconstruction patterns with Kikuchi lines indicating high quality of the substrate surface. The typical GeTe growth rate is about ∼0.5 nm/min for the samples mentioned here at a growth temperature of 220 °C. Figure 4.3 (a-c) shows the RHEED images at various stages of the GeTe growth on Si(111). Epitaxial growth is performed by opening both Ge and Te shutters simultaneously. As soon as the shutters are opened, the Si(111)-7×7 reconstruction disappears. In about ~ 2 minutes, the intensity of the Si reflections completely disappear and only a diffuse pattern characteristic of an amorphous layer as shown in figure 4.3 (b) is visible. The amorphous pattern persists for about ~ 600 secs before a streaky crystalline RHEED pattern appears as shown in figure 4.3 (c). This amorphous-to-crystalline transition, also called incubated epitaxy is reported for the growth of GST on GaSb(001) [113,114] and Sb on GaAs(110) [115].

The streaky RHEED pattern indicates a smooth surface. However, if the surface contains large smooth islands, the RHEED intensity will still show a streaky pattern. If we look at the RHEED streaks carefully, an intensity modulation (figure 4.3 (c)) is visible, indicating that the layer is not completely smooth and has some flat islands. Atomic force microscopy (AFM) studies on the GeTe films grown on Si(111), show flat triangular islands (see figure 4.4). The root mean square (rms) roughness of the film is about 5.3 nm. The triangular islands point in different directions as shown in figure 4.4. This might indicate the presence of rotational domains. To know whether the film is closed, a side view scanning electron microscope (SEM) image was taken and is shown in figure 4.4 (b). The triangular islands project above the surface of the completely filled GeTe film. In the inset, a top view SEM is shown which displays an identical morphology as observed *via* AFM.

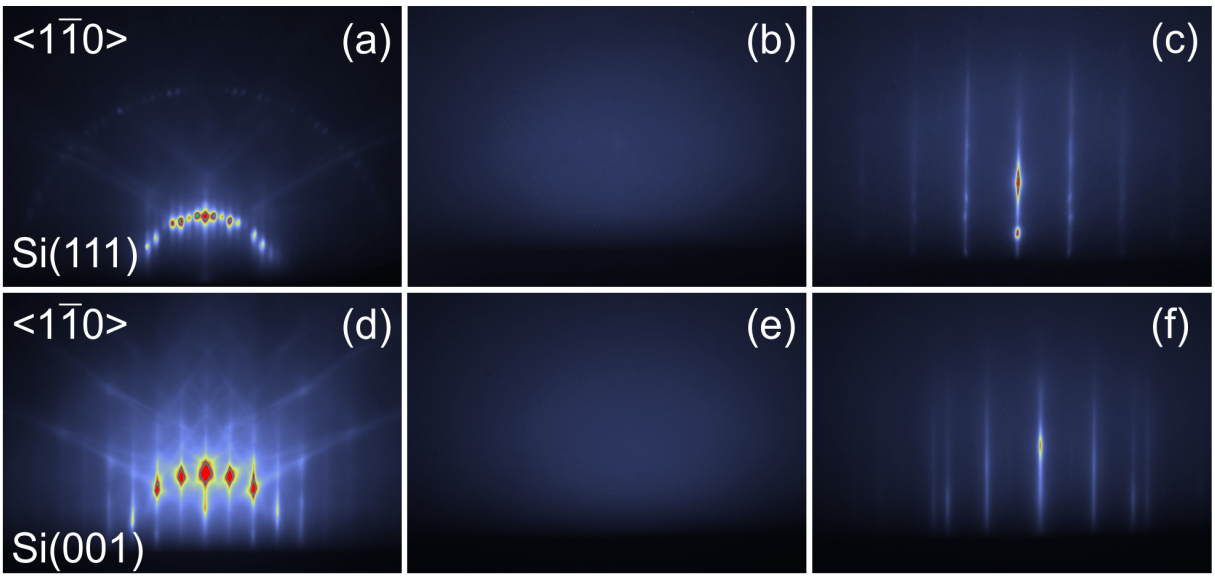

Figure 4.3: RHEED image along <1$\bar{1}$0> azimuth during various stages of GeTe growth on Si(111) (a-c) and on Si(001) (d-f); (a)&(d) show the initial silicon surface; (b)&(e) the intermediate amorphous transition stage during GeTe growth; (c)&(f) the final surface of the GeTe epitaxial layer

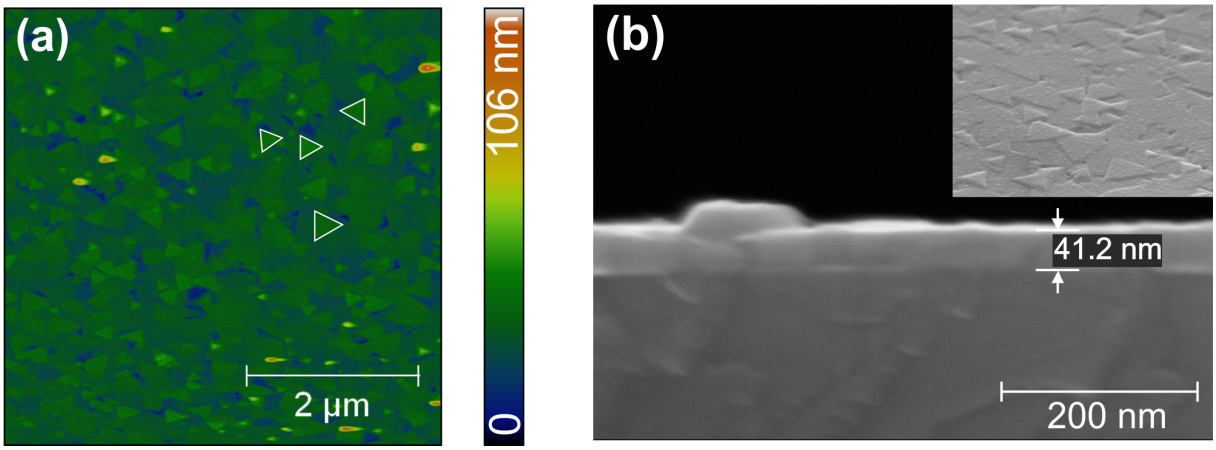

Figure 4.4: Surface morphology of GeTe grown on Si(111): (a) AFM image over an area of 5×5 μm^2 show a rms roughness of ∼5.3 nm. Few rotational domains are highlighted in white triangles (b) Side view SEM showing smooth surface with flat islands and the inset shows a top view SEM image

The growth on Si(001) also exhibits an intermediate amorphous transition (figure 4.3 (e)) before turning into streaky crystalline RHEED pattern as shown in figure 4.3 (f). The origin of the incubated epitaxy is unclear. To understand this further, let us consider the example of GST on GaSb(001), which exhibits a similar growth pattern. In-plane XRD pattern shows two different surface symmetries: four fold and six fold symmetry [114]. GST exhibits a distorted rhombohedral structure with the rhombohedral distortion along the [111] direction. For films growing on (001) substrates, the rhombohedral distortion will lay in-plane and thus affects the film quality. To avoid the poor crystalline quality, Shayduk et al., chose (111) oriented surface to accommodate the distortion along growth direction. Interestingly, GST grown on (111) oriented surfaces does not show an intermediate amorphous transition during growth [116] and exhibit high crystalline quality [117]. The case of GeTe on Si can be similarly treated. Figure 4.5 (a), (b) and (c) show the GeTe unit cell viewed along [111], [11$\bar{1}$] and [001] directions respectively. It is to be noted that the lattice stacking viewed along [111] and [11$\bar{1}$] directions are dissimilar. For growth along [111] direction, the distortion is perpendicular to the surface, and hence we expect a smooth growth as reported for GST on GaSb(111). However, if the distortions are parallel to the surface, strain along the in-plane directions are expected as is the case of GST on GaSb(001).

Considering the GeTe growth on Si(111), the in-plane lattice mismatch[1] are given in table 4.1 for growth along [001] and [111] direction. Coincidence site lattice favours the growth of

Epitaxial relationship	Lattice mismatch
$GeTe[1\bar{1}0]\|\|Si[1\bar{1}0]$	8.38 %
$GeTe[11\bar{2}]\|\|Si[11\bar{2}]$	8.38 %
$GeTe[010]\|\|Si[1\bar{1}0]$	43.50 %
$GeTe[100]\|\|Si[11\bar{2}]$	148.56 %
$4 \times GeTe[010]\|\|6 \times Si[1\bar{1}0]$	3.69 %
$4 \times GeTe[100]\|\|11 \times Si[11\bar{2}]$	2.04 %

Table 4.1: GeTe lattice mismatch for growth along [001] and [111] direction on Si(111)

GeTe along [001] direction as the mismatch is smaller. However, during the nucleation both the epitaxy relations seem to coexist however without any long range order. The diffuse RHEED pattern might be the resultant of the absence of long range ordering. After a certain critical thickness, the growth along [111] direction seems to be energetically stable and the film continues to grow along this direction.

To analyze the nucleation stages further, we performed azimuthal RHEED scans, which give the in-plane structural information of the surface. Figure 4.6 (a) shows the initial Si(111) surface. The high symmetry directions [0$\bar{1}$1] and [1$\bar{2}$1] are highlighted. A zoom of the rectangle shown in figure 4.6 (a) is given in figure 4.6 (b). A typical Si(111)-7 $\times$ 7 reconstruction is observed.

[1]Lattice mismatch is calculated using the formula

$$(\frac{a_{epilayer} - a_{substrate}}{a_{substrate}}) or (\frac{q_{substrate} - q_{epilayer}}{q_{epilayer}})$$

where, a is the lattice parameter and q is the scattering vector.

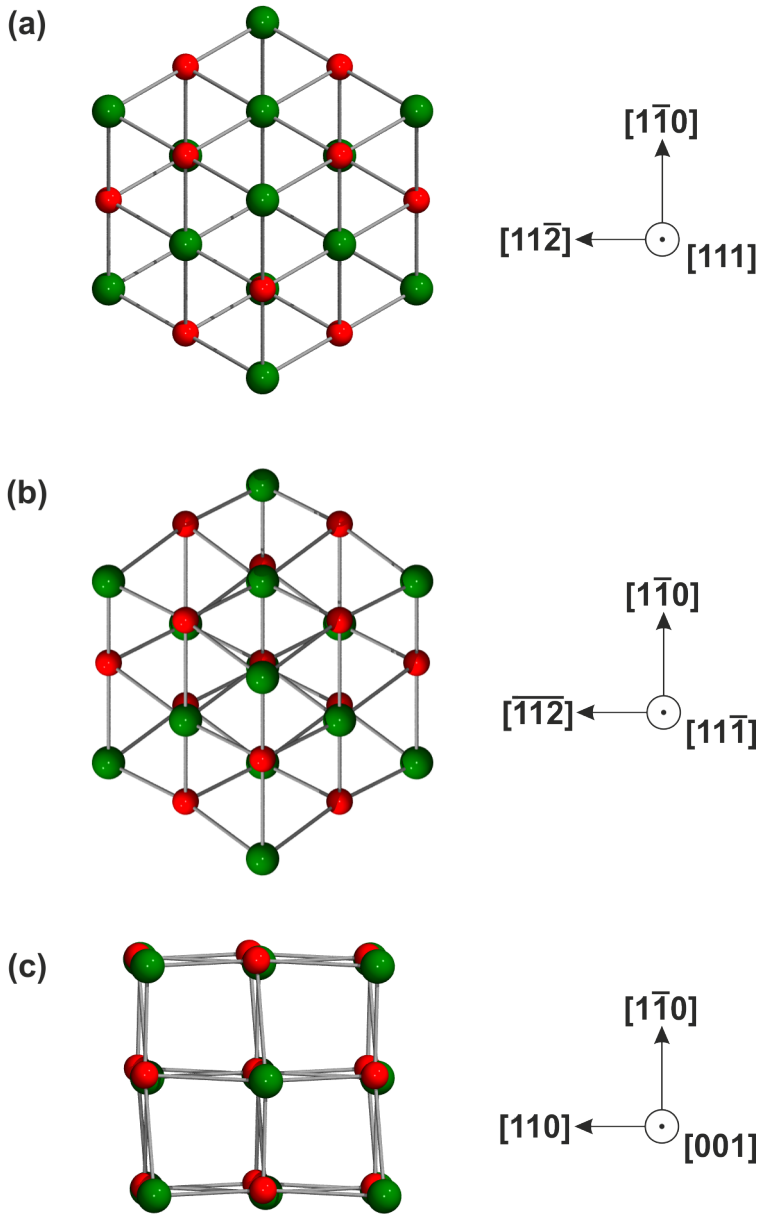

Figure 4.5: View of the GeTe unit cell along (a) [111] direction, (b) [11$\bar{1}$] direction and (c) [001] direction

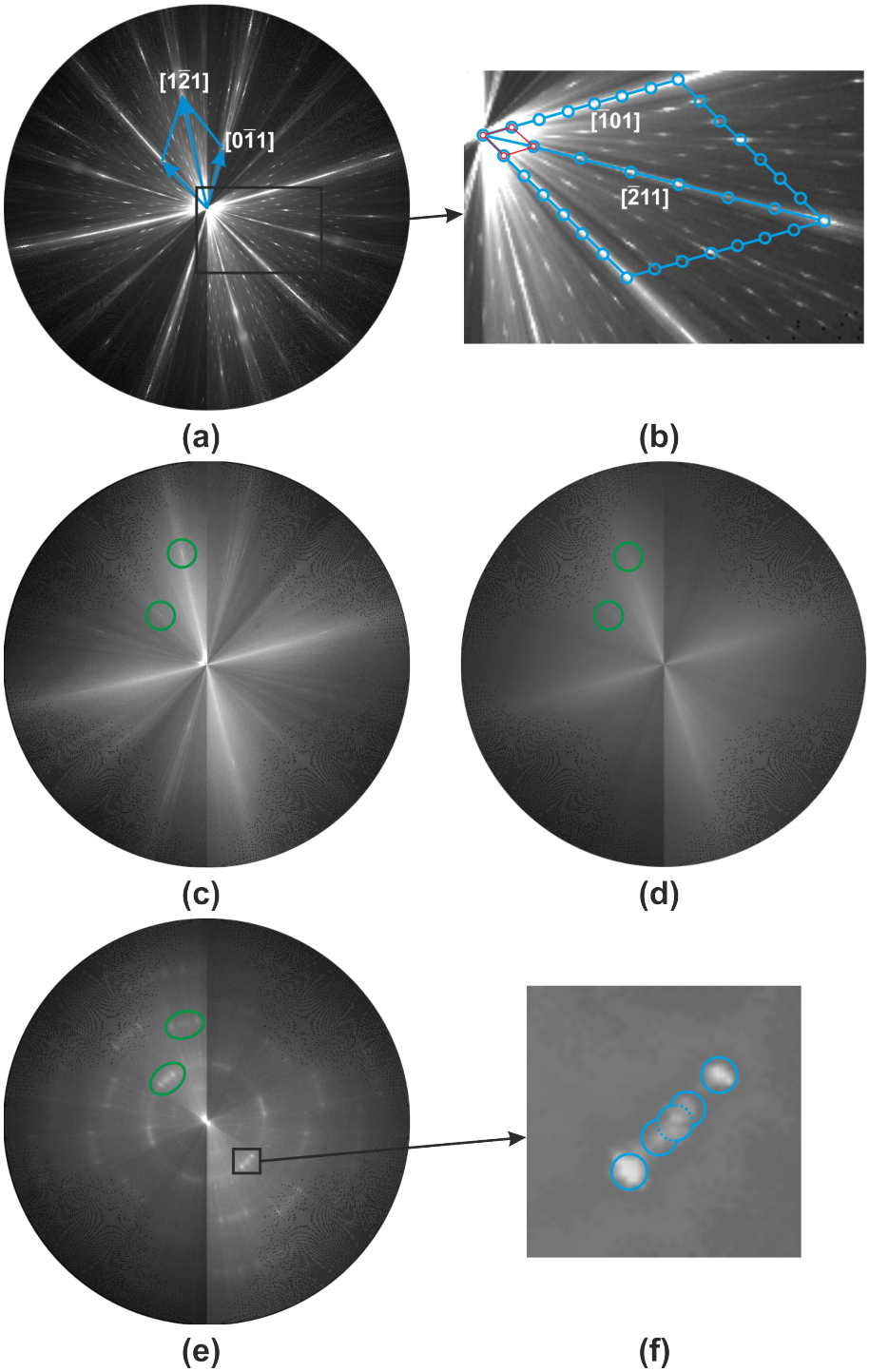

Figure 4.6: In-plane azimuthal RHEED scans during various stages of growth. (a) Initial Si(111) surface; (b) Zoom of the rectangle showing Si(111)-7×7 reconstruction, blue rhombus is the unreconstructed Si unit cell and the red rhombus is the surface unit cell; (c) After opening Ge and Te shutters, green circles contain (1$\bar{1}$0) and (1$\bar{2}$1) reflections); (d) Amorphous transition; (e) Crystalline transition; (f) Zoom of the rotational domains indicating 5 distinct spots

The azimuthal scans are performed with a rotation speed (of the substrate) of about 1° for every 10 seconds. So, the resolution of the reconstructed image is not good enough to distinctly see each reflection. However, the intensity modulations are clearly seen. RHEED intensity of the Si(111) reconstruction starts to decrease at the onset of GeTe growth as shown in figure 4.6 (c). Faint Si diffraction spots (inside green circles) along the $[1\bar{1}0]$ and $[1\bar{2}1]$ directions are visible. However upon amorphous transition, six fold symmetry disappears completely and a weak diffuse intensity pattern with four fold symmetry appears (see figure 4.6 (d)). During this stage, RHEED image along any particular azimuth shows amorphous pattern with diffuse background. However, a difference in intensity of the diffuse background signal is observed upon substrate rotation, resulting in the appearance of a weak four fold symmetry. The origin of this weak four fold symmetry is unclear as to why it is observed on amorphous layer. This might suggest that growth happens along [001] during the nucleation stage. This phenomenon is unusual and therefore a detailed nucleation study is further necessary to clarify this point. Upon crystalline transition, the six fold surface symmetry reappears indicating possible [111] oriented growth. Growth along the [111] direction might be energetically favourable as the distortion is aligned perpendicular to the surface. The rhombohedral distortion and suitability of growth along [111] direction was discussed in detail by Shayduk et al., using the comparison of GST growth on (001) and (111) oriented GaSb substrates[116].

Rotational domains are observed as soon as the crystalline transition takes place. Figure 4.6 (f) is a zoom of the region of interest showing rotational domains along $[\bar{1}10]$ direction. Five intense spots are seen (highlighted in blue) and the details about these peaks will be discussed later in section 4.3.1.

4.3.1 Growth Direction and Rotational Domains

Specular $\omega - 2\theta$ XRD scan of GeTe on Si(111) is shown in graph 4.7 (blue curve). The sharp

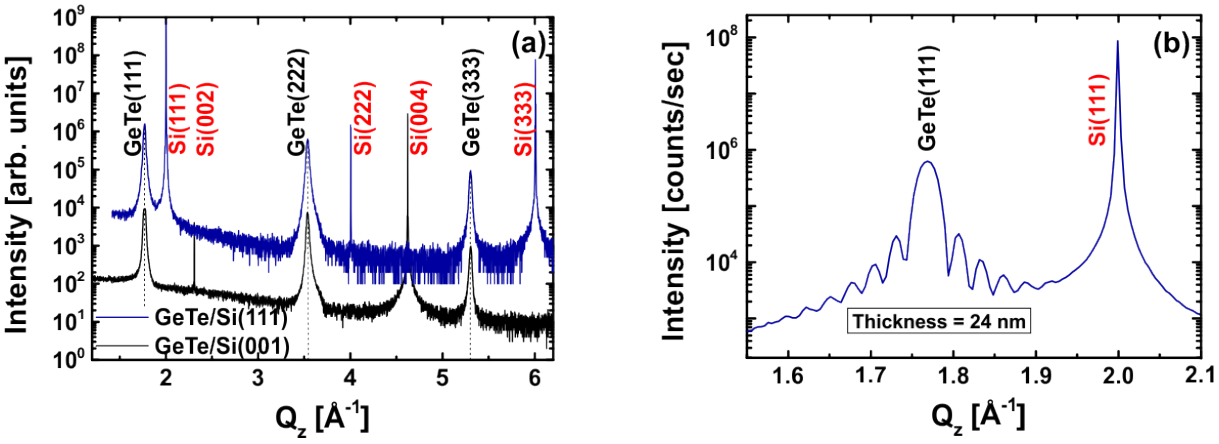

Figure 4.7: (a) Specular $\omega - 2\theta$ xrd scans for the growth of GeTe heterostructures on Si(111) (blue) and Si(001) (black). (b) Laue oscillations around the GeTe (111) peak

features at $q_z = 2.00$, 4.01 and 6.01 Å^{-1} are attributed to Si(111), (222) and (333) reflec-

tions respectively. The three remaining Bragg peaks at q_z = 1.77, 3.54 and 5.31 Å^{-1} are from GeTe(111), (222) and (333) reflections respectively. There are no other out-of-plane orientations implying that the GeTe growth proceeds only along the [111] direction. Its out of plane lattice mismatch with respect to silicon is about 13.18% and the out of plane lattice constant (10.649 Å) is about ∼0.16% smaller than the bulk value (10.666 Å)[118]. Interestingly, the specular $\omega - 2\theta$ XRD scan of GeTe on Si(001) shows that GeTe grows along [111] direction rather than [001] direction (see figure 4.7 black curve)). This implies that the substrate orientation does not have a major influence on the growth direction of GeTe. It seems that in both cases (GeTe/Si(111) and GeTe/Si(001)), the growth along the [111] direction is more favourable, most probably due to reduced strain along this particular direction. The preferential growth of GeTe on Si(111) is mainly due to the local forces that act on the nucleus in the film plane, which is released by favouring the growth along [111] direction, so that the distortion is perpendicular to the film surface[119]. Figure 4.7 shows a zoom of the specular rod around the Si(111) peak. Laue fringes due to interference effects between the epilayer and substrate appear around the GeTe(111) Bragg peak, indicating high crystalline quality of the film. From the q_z spacing of the Laue oscillations, the thickness of the epilayer is estimated to be about ∼24 nm.

Figure 4.8 (a and b), (c and d) shows the RHEED images taken along the two high symmetry directions [11$\bar{2}$] (indexed in red) and [1$\bar{1}$0] (indexed in white), respectively. Figure 4.8 (a and c), (b and d) corresponds to the RHEED images for the epitaxial GeTe films grown on Si(111) and (001) substrates, respectively. Analysis of the streak positions indicate that, on both substrates a 3× (red line) reconstruction along [11$\bar{2}$] direction and 1× (white line) reconstruction along the [1$\bar{1}$0] direction are present.

The multiple streaks present in the RHEED pattern are due to the contribution of rotational domains present in the film. Figure 4.9 (a-d) helps to visualise the diffraction pattern in the presence of rotational domains. For a perfect surface without any rotational domains, we should observe only the diffraction pattern that corresponds to the beam direction. Figure 4.9 (a) shows the Ewald sphere (2D) and reciprocal lattice points for electron beam incident along [1$\bar{1}$0] direction. By a rotation of 30° of the crystallographic netplanes, the electron beam impinges along the [1$\bar{2}$1] direction as shown in figure 4.9 (b). If two domains rotated by 30° against each other are present, the reciprocal lattice points as shown in figure 4.9 (c) are expected and their combined diffraction contribution results in muliple streaks. For the sake of simplicity, we have given the first three figures in 2D space. In reality, the Ewald sphere consists of reciprocal lattice points in 3D space and the intersection of all the reciprocal lattice points with the Ewald sphere gives rise to diffraction maxima along the Laue rings or streaks depending on the surface morphology as shown in figure 4.9 (d).

To investigate the reconstruction further, azimuthal RHEED scans were performed after the end of the growth run, when substrate temperature was ramped down to room temperature. Figure 4.10 (a) shows scan obtained after the growth of GeTe on Si(111). From the azimuthal scans acquired during various stages of growth and shown in figure 4.6 (a-d), it is evident that the GeTe film aligns its high symmetry in-plane directions with the ones of the substrate, namely: GeTe<1$\bar{1}$0>||Si<1$\bar{1}$0> and GeTe<11$\bar{2}$>||Si<11$\bar{2}$>. The surface has a six fold symmetry, as can be seen from the highlighted hexagons in the figure. Furthermore each spot is actually a combination of 5 features (see zoom of figure 4.10 (a)) with a maximum angular separation

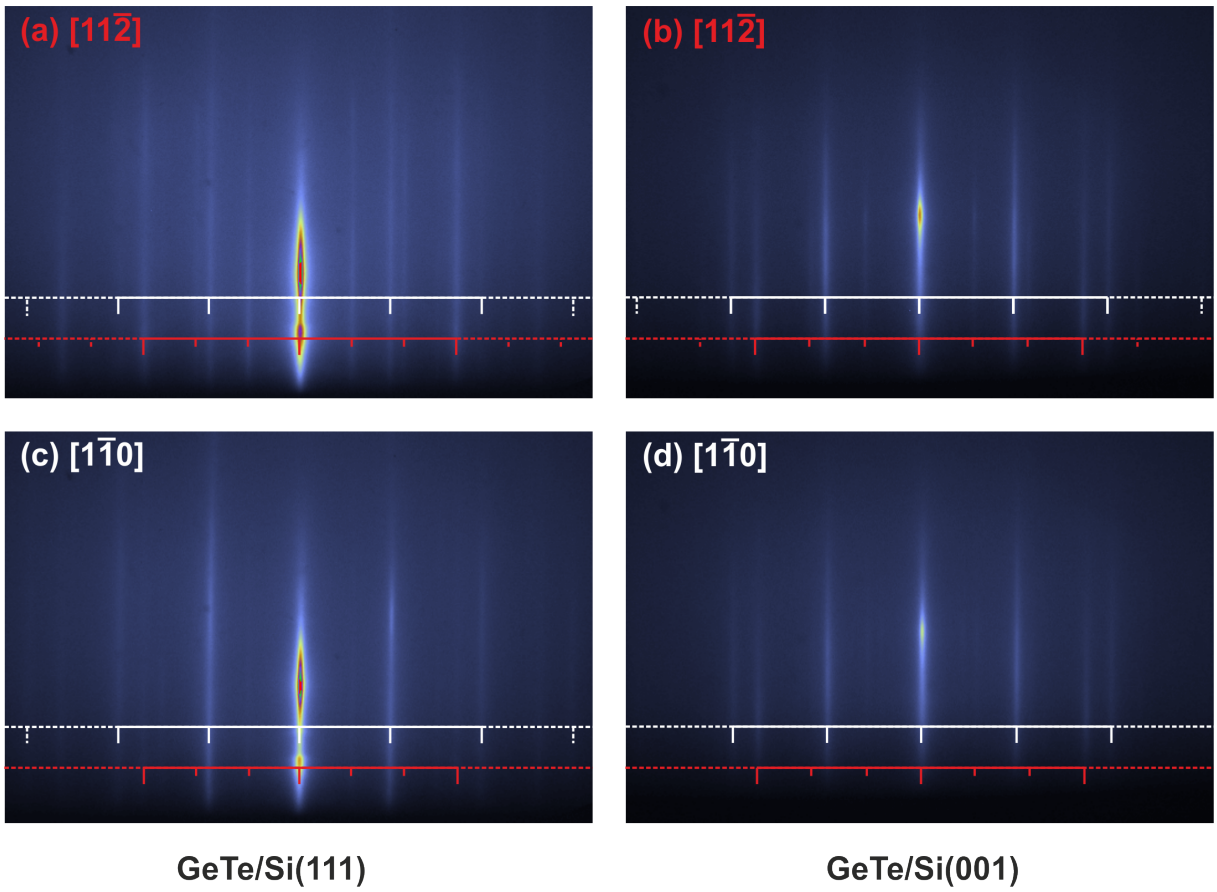

Figure 4.8: RHEED images along [11$\bar{2}$] (indexed in red) and [1$\bar{1}$0] (indexed in white) directions for epitaxial GeTe films grown on Si(111) (a and c) and Si(001) (b and d) substrates. On both substrates, we observe a 3× reconstruction along the [11$\bar{2}$] and 1× reconstruction along the [1$\bar{1}$0] directions, respectively

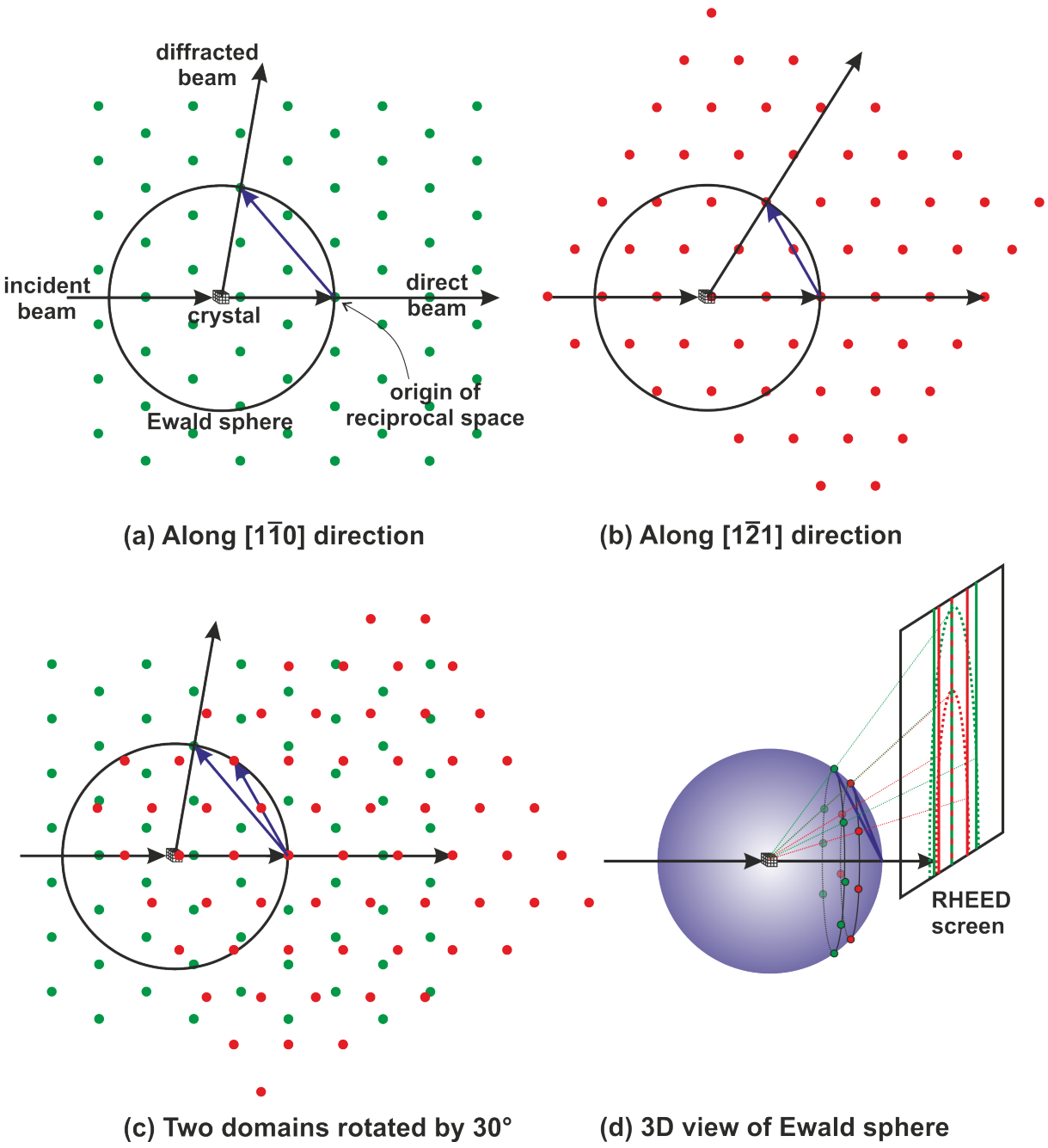

Figure 4.9: Schematic diagram of diffraction in the presence of rotational domains. Diffraction along, (a) [1$\bar{1}$0] direction , (b) 30° rotated domain (along [1$\bar{2}$1] direction), (c) in the presence of both the domains. (d) Artistic view of the Ewald sphere showing diffraction from the two domains

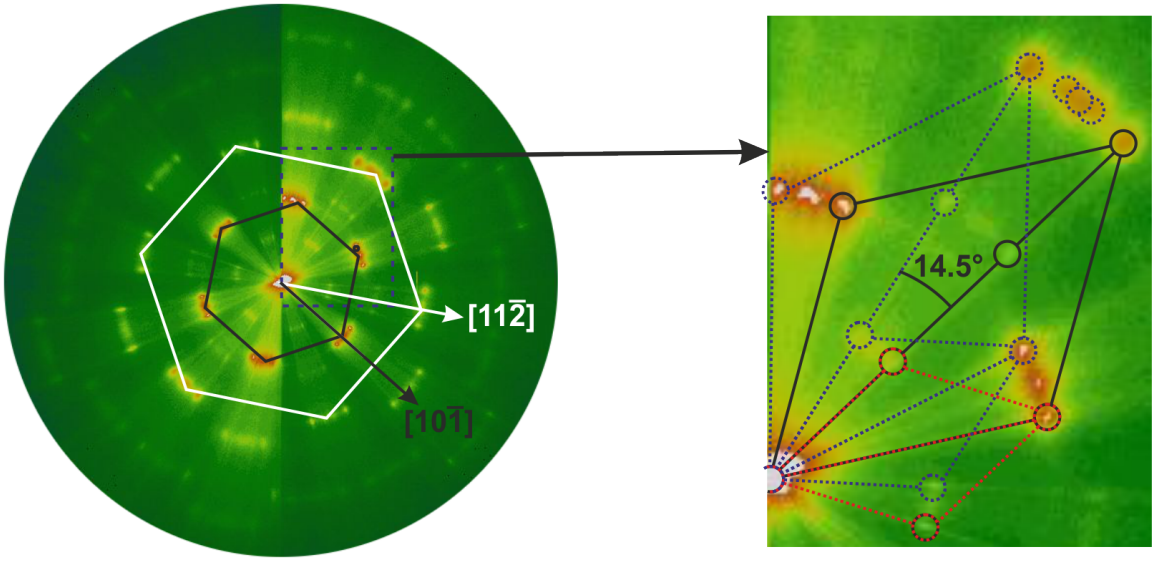

(a) GeTe/Si(111)

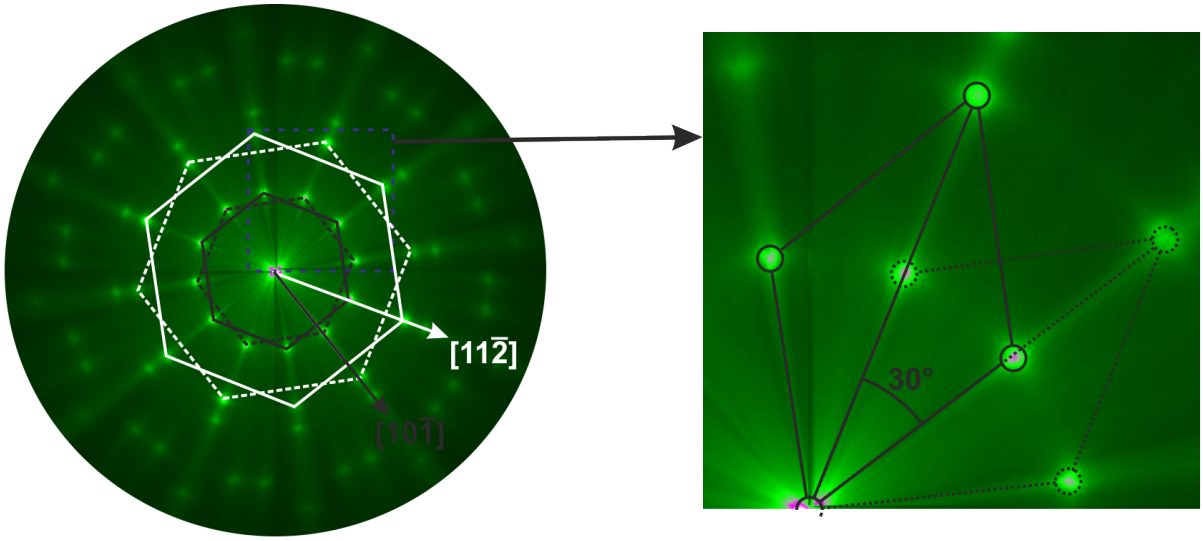

(b) GeTe/Si(001)

Figure 4.10: Azimuthal RHEED scans for GeTe growth: (a) on Si(111), zoom of the white rectangle shows rotational domains with 5 prominent spots. Black rhombus represents the bulk unit cell and the red, the surface unit cell. The surface and bulk unit cell are rotated by 30° giving rise to $(\sqrt{3} \times \sqrt{3})$R30 reconstruction and (b) on Si(001), zoom shows each domain is rotated by 30°, The bulk and surface unit cell (black rhombus) overlap each other giving rise to 1x1 reconstruction

of about ∼7° from the central spot (see also azimuthal scan shown in figure 4.11 (a)). The large mismatch between the epilayer and substrate[120,121] combined with different in-plane symmetry[122–124] might play a dominant role in the formation of these rotational domains. The presence of rotational domains affect the determination of the surface reconstruction. However, from the azimuthal RHEED scans, a 1× reconstruction along the $[0\bar{1}1]$ direction and 3× reconstruction along the $[1\bar{2}1]$ direction are visible. The GeTe unreconstructed surface unit cell is represented by a black rhombus and the surface unit cell by the red rhombus. The bulk and the surface unit cell are rotated by 30°, giving rise to $(\sqrt{3} \times \sqrt{3})$R30 reconstruction.

In the case of GeTe growth on Si(001), we observe 12 fold symmetry (see the hexagons in figure 4.10 (b)) in-plane with the domains rotated by 30° and consisting of twins. Unlike the GeTe growth on Si(111), these domains have sharp intensity peaks. The minimum number of rotational domains is given by the formula $N_{RD} = lcm(n, m)/m$, where lcm is the least common multiple, n and m are the in-plane symmetries of substrate and epilayer respectively[122]. In-plane symmetry for the case of Si(001) surface is 4 and for GeTe it is 3. Using the formula, the number of rotational domains is 4 in this case. However, due to the presence of twins, two domains rotated by 30° are present, while the other two overlap with the first. Along the $[0\bar{1}1]$ direction, a 1× reconstruction is observed and along $[1\bar{2}1]$ direction, a weak 3× reconstruction is observed (see figure 4.8 (b and d)), which is not visible in the azimuthal scan maybe due to the weak streaks. If the weak 3× reconstruction observed in figure 4.8 (b and d) are taken into account, the surface reconstruction must be similar to the one on Si(111), giving rise to $(\sqrt{3} \times \sqrt{3})$R30 reconstruction.

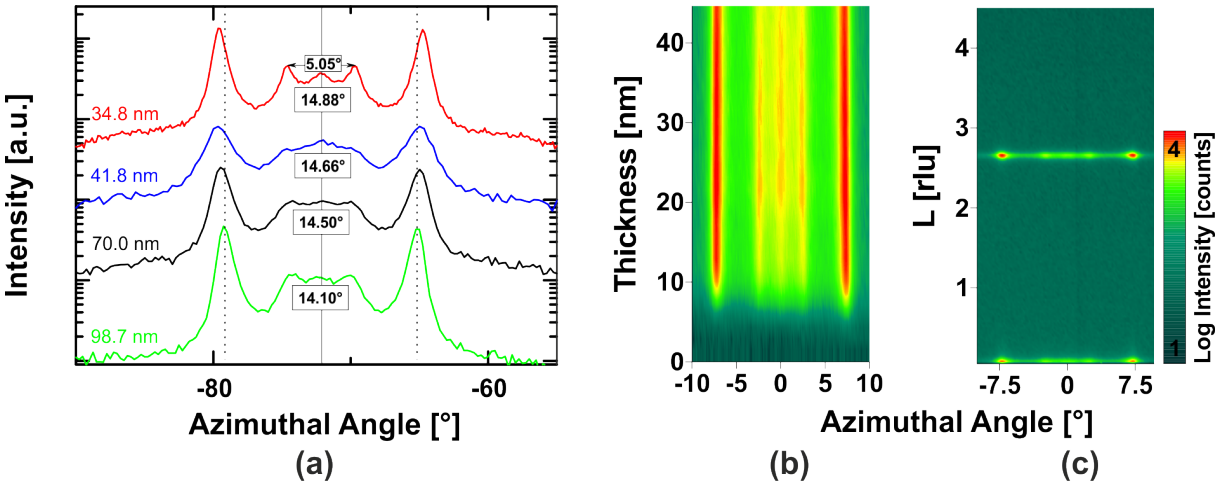

Figure 4.11: (a) Angular range of the rotational domain decreases with film thickness; (b) Right from the amorphous-to-crystalline transition, the azimuthal rotation is observed; (c) No additional peaks observed out-of-plane close to the GeTe rotation domains

It is to be noted that for GeTe growth on Si(111), the substrate and epilayer have the same orientational symmetry, and hence according to Grundmann[122], a single domain is expected. In certain systems, it is observed that even though the surface symmetry of the epilayer and substrate are the same, the large lattice mismatch results in rotation of domains to minimize

the misfit [120,121]. GeTe has about 8.38% in-plane lattice mismatch with respect to the substrate. Hence, rotational domains are possible. Figure 4.11 (a,b) shows the rotational domain as a function of thickness for GeTe growth on Si(111).

GeTe growth was carried out and the $(22\overline{4})$ reflection monitored *in-vivo* (more details about *in-vivo* studies can be found in the next section). Figure 4.11 (b) shows the thickness versus azimuthal rotation scans (which was taken around $(22\overline{4})$ reflection) obtained during the growth of GeTe on Si(111). The rotational domains start to appear right from the amorphous-to-crystalline transition. The separation between the rotational domains decreases from 15.1° during the initial stages to about 14.5° for about 50 nm. Figure 4.11 (c) shows a series of out-of-plane (L) scans around the same peak. The map shows that the rotational domains are present only at specific scattering vectors corresponding to $22\overline{4}$ and $33\overline{3}$ planes. However, there are no other additional reflections corresponding to different lattice planes as shown from the $Q_{angular}$ scans at different L values.

The spacing between the rotational domains is a function of layer thickness. At larger thickness the rotational domains get closer and closer. A possible explanation can be that, during the nucleation the larger lattice misfit results in large separation of the rotational domains. But with the growth of subsequent GeTe monolayers, the newly formed GeTe layers have lower and lower misfit with respect to the underlying GeTe layer. Thus the rotational domain angles decreases with increase in thickness. The outer peaks are sharp and intense and are separated by approximately ∼14.5° for a layer thickness of 50 nm.

4.4 *In-situ* Grazing Incidence X-Ray Diffraction

With the movement of MBE chamber into the Pharao beamline, it was possible to perform *in-vivo* measurements during the growth of GeTe thin films. It is especially useful in studying the initial amorphous-to-crystalline transition, which is not accessible with a lab diffractometer because of its low intensity and aging of the GeTe thin films. Here we discuss some of the *in-vivo* studies performed during the growth and *in-situ* studies after the growth.

4.4.1 *In-situ* Studies of the Incubation Stage: GeTe on Si(111)

In-situ studies in particular might help to shed light on the origin of the amorphous-to-crystalline transition during the growth. To this end, a GeTe growth with the usual growth procedure was performed. As soon as the amorphous-to-crystalline transition appears (a faint signal is observed in the RHEED pattern), the growth was interrupted and the sample abruptly cooled down. Immediate cooling is necessary to prevent desorption.

Figure 4.12 (a) shows an extended reflectivity scan ($\omega - 2\theta$ scan) along the specular rod taken to determine the thickness of the amorphous layer (grown during the incubated stage). The film shows Kiessig fringes with an average q_z spacing of $\sim 0.1065\text{Å}^{-1}$. In real space, this corresponds to a thickness of $\sim$ 59 Å. Along [111] direction, a bulk GeTe unit cell measures 10.6657 Å. This is about 5-6 unit cells of GeTe formed during the incubation stage indicating that the incubation stage is pretty large. With the high photon flux of synchrotron, it is possible to observe diffraction from rather thin layers. The extended reflectivity or the specular $\omega - 2\theta$ scan

shows 4 Bragg peaks corresponding to a larger unit cell. The four peaks present in the scan correspond to a lattice spacing of 6.81 Å, 3.41 Å, 2.28 Å and 1.76 Å. For typical GeTe growing along [111] direction, we should observe two peaks corresponding to a lattice spacing of 3.56 Å and 1.78 Å for GeTe (111) and (222) reflections respectively. Considering the second and fourth peaks, they might be interpreted as strained GeTe. However, looking at the d-spacing carefully they do not belong to the same set of Bragg planes. Interestingly, the first three peaks belong to

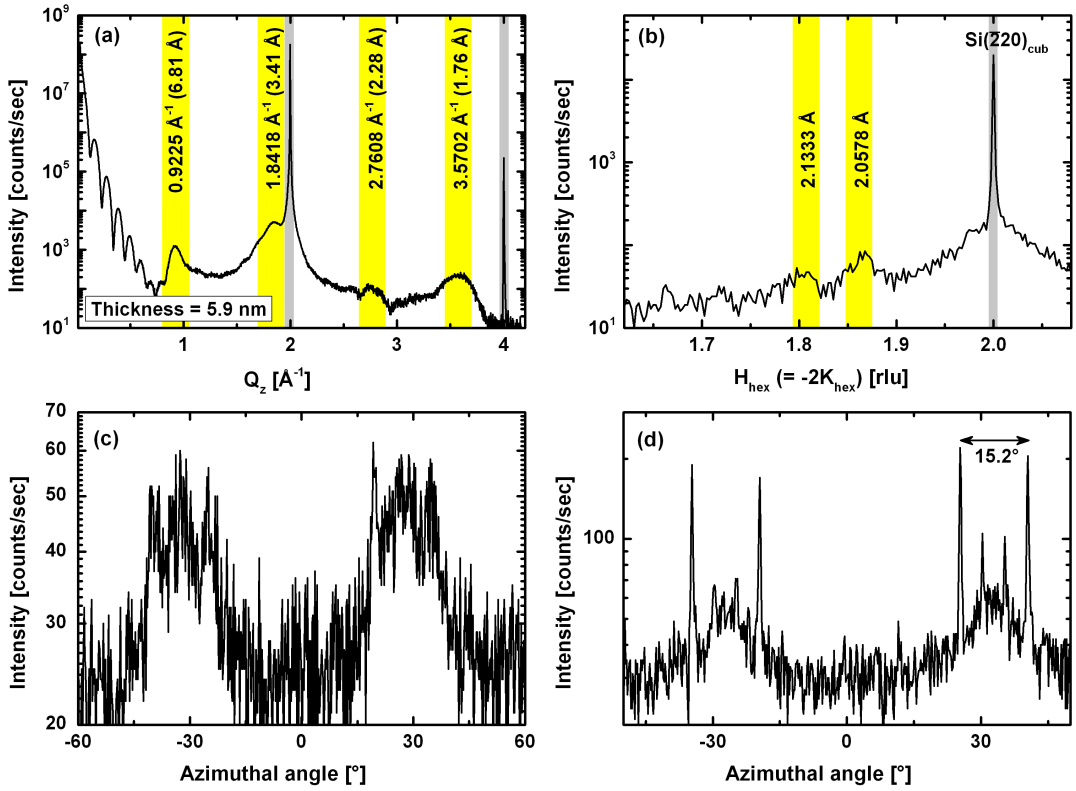

Figure 4.12: (a) Extended reflectivity scan of GeTe on Si(111), (b) In-plane scan along [$\bar{2}$20] direction showing two peaks at H = 1.8 Å^{-1} and 1.866 Å^{-1}, (c) Azimuthal scan at H = 1.8 rlu and (d) Azimuthal scan at H = 1.866 rlu

the same set of Bragg planes exhibiting integer order reflections. The second and third peak are two and three times the reciprocal spacing of the first peak respectively. The presence of peak at almost half the q_z value of a typical (111) GeTe reflection indicates a superstructure of twice the typical GeTe cell along [111] direction. However, the presence of other orientations cannot be ruled out, as is the case of the fourth peak at $q_z = 3.5702$ Å^{-1} which does not correspond to the first three reflections. The peak positions were compared with the Ge and Te structures to account for atomic segregation, but they do not correspond to the d-spacing of these reflections.

The out of plane reflection does not give full information of the crystal stacking and preferred

orientations. So an in-plane line scan along [$\bar{1}$10] direction was performed and the resultant graph is shown in figure 4.12 (b). Two weak peaks are present corresponding to a lattice spacing of 2.1333 Å and 2.0578 Å at H = 1.8 and 1.8666 rlu respectively[2]. These d-spacing values are close to the bulk GeTe values for ($\bar{2}\bar{2}$0) = 2.1436 Å, ($\bar{2}$20) = 2.0810 Å and (221) = 2.0455 Å.

reflection	**bulk d-spacing (in Å)**	**film d-spacing (in Å)**	**error with bulk**
($\bar{2}\bar{2}$0)	2.1436	2.1333	$\sim$ 0.48 % smaller
($\bar{2}$20)	2.0810	2.0578	$\sim$ 1.11 % smaller
(221)	2.0455	2.0578	$\sim$ 0.60 % larger

Table 4.2: Possible orientations of the observed two peaks in figure 4.12 compared with bulk GeTe d-spacing

Table 4.2 shows a comparison of the GeTe lattice spacing observed during the nucleation stage with respect to the bulk GeTe values. For the first case (d-spacing = 2.1333 Å), only the ($\bar{2}\bar{2}$0) reflection almost matches the bulk value and is 0.48% smaller than the bulk value. Considering that GeTe has a larger lattice constant than Si, it is reasonable that during the initial nucleation stages, there is a compressive strain of the GeTe lattice to match the Si lattice. Hence the in-plane d-spacing of the film gets smaller. However, for the second peak (d-spacing = 2.0578 Å), two possible reflections can be assigned namely ($\bar{2}$20) and (221). Considering the first case, we expect the second peak also to be of compressively strained and hence the only possibile reflection for that peak corresponds to ($\bar{2}$20) reflection. ($\bar{2}$20) and ($\bar{2}\bar{2}$0) are two orthogonal directions with two different lattice spacings because of the rhombohedral distortion, can lie in-plane only when the growth is along [001] direction. So, this shows there is a signature of growth along the [001] direction.Figure 4.12 (c) and (d) shows the azimuthal scan corresponding to the two reflections at H = 1.8 and 1.8666 rlu respectively. Rotational domains are observed even during the incubation stage and the domains are separated by a maximum angle of about 15.2°. These rotation domains are a signature of GeTe growth on Si(111) indicating that both the peaks correspond to the GeTe reflections. Considering that, the growth process was interrupted just before the start of streaky RHEED pattern, we expect a small contribution of film growth along [111] direction towards the end of amorphous transition and the resultant roational domains might be attributed to film growing along [111] direction.

4.4.2 *In-vivo* Studies During the Growth of GeTe on Si(111)

Out-of-Plane Scan

Figure 4.13 (a) shows the specular L-scans (conventional $\omega - 2\theta$ scans) during the growth of GeTe on Si(111). The scans were performed continuously during the growth, with each scan corresponding to a layer thickness of approximately 1 nm. An out-of-plane map is constructed as shown in the figure 4.14 (a) by extrapolating datapoints between each successive scan. The peak at L=6 corresponds to the Si(222) peak, while the region between L=4.8 and 5.9 corresponds to the GeTe peak evolution during the growth. In this region, the scan with the lowest intensity

[2]where H and K are the reciprocal surface coordinates

(figure 4.13 (a)) corresponds to the substrate and subsequent scans with increasing intensity correspond to an addition of 1 nm film each. The graph represents the first 7 nm of growth. The peaks are fitted using a Gaussian function to find the peak parameters such as intensity, area, FWHM and position. The mismatch of the peak positions with respect to the substrate is shown as a function of thickness in figure 4.13 (b). An interesting thing to note here is that,

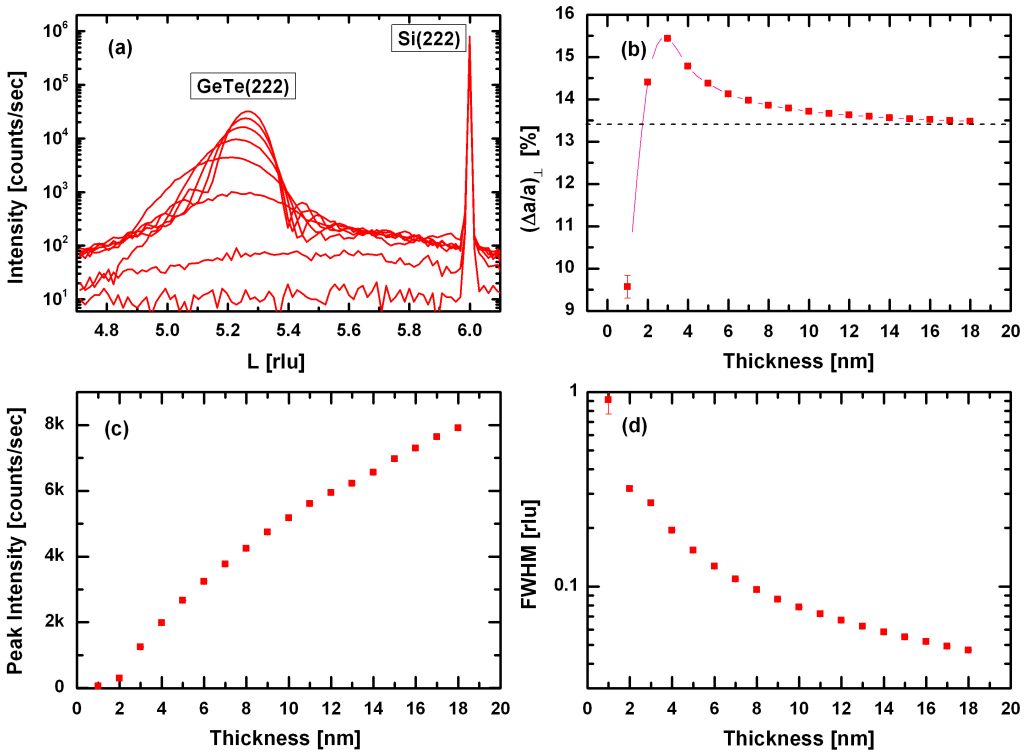

Figure 4.13: *In-vivo* studies during growth: (a) specular L-scans during growth, (b) lattice mismatch with respect to the substrate, black dashed line indicates the bulk mismatch (c) change in peak intensity with thickness and (d) change in full width at half maximum with increase in thickness

the out-of-plane lattice mismatch increases from 9.57% (for 1nm film) initially upto 15.43% (at 3nm) and then decreases gradually to reach a steady state value of 13.48%. We expect the film to be compressively strained in-plane as the GeTe lattice parameter is larger than the Si lattice parameter. So, if the film is compressively strained in-plane, it should be tensely strained out-of-plane and in this case, the lattice mismatch should decrease from a maximum value to a value expected for a completely relaxed film. This is observed only for a thickness greater than 3 nm. If we look at the initial d-spacing of GeTe reflection at 1 nm and the final d-spacing for a lattice mismatch of 9.57% and 13.48%, they are 1.7178 Å and 1.7774 Å respectively. These

correspond to $(22\bar{2})$ and (222) reflections of GeTe respectively. GeTe being a rhombohedral crystal with distortion along [111] direction, it has different lattice spacing along $[11\bar{1}]$ and [111] directions respectively. It is assumed that during the amorphous transition as observed by RHEED, the film initially tries to grow in different directions (one among them being $[11\bar{1}]$ direction as found from the initial out-of-plane lattice spacing which matches closely with the $(22\bar{2})$ reflection). During the amorphous-to-crystalline transition, the growth seems to be more

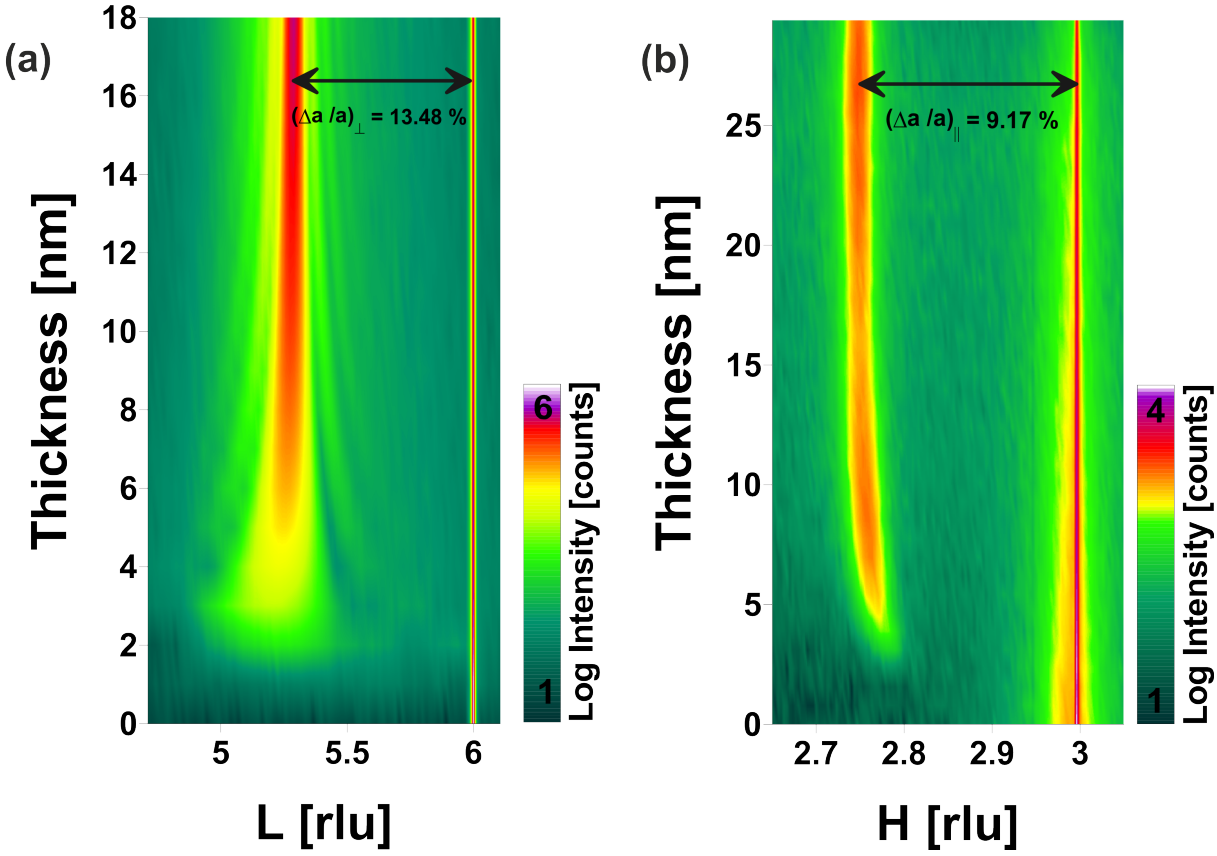

Figure 4.14: XRD scans during the growth as a function of thickness (a) Out-of-plane: L-scan (|||[111] direction) and (b) In-plane: H scan (|||$[\bar{2}11]$)

favourable along the [111] direction, as the strain is accommodated perpendicular to the film surface. This preferential direction is confirmed by the final d-spacing of the (222) reflections measured from the specular L-scans or the $\omega - 2\theta$ scans. Figure 4.13 (c) shows a non-linear change in peak intensity with respect to thickness indicating that the growth rate is non-linear. The full width at half maxima (FWHM) decreases with increase in thickness as shown in figure 4.13 (d). Initially the crystallite sizes are small during the start of growth and with time, they coalesce to form large islands resulting in narrowing of the peaks or the reduction of peak widths.

In-Plane Scan

Figure 4.14 (b) shows the in-plane map during growth. H axis corresponds to $[\bar{2}11]$ direction and the peak at H = 3 rlu is the Si($\bar{4}22$) peak. The region between H = 2.7 and 2.8 rlu shows the GeTe($\bar{4}22$) peak evolution during growth. At the start of the growth, there are no peaks observed till a growth of 3 nm. Interestingly, this thickness is the critical point in the out-of-plane scan above which the out-of-plane lattice mismatch decreases and below which the out-of-plane lattice mismatch increases considerably. We start to observe any diffraction signal only after a film thickness of about $\sim$ 3 nm. Initially the layer is compressively strained in-plane

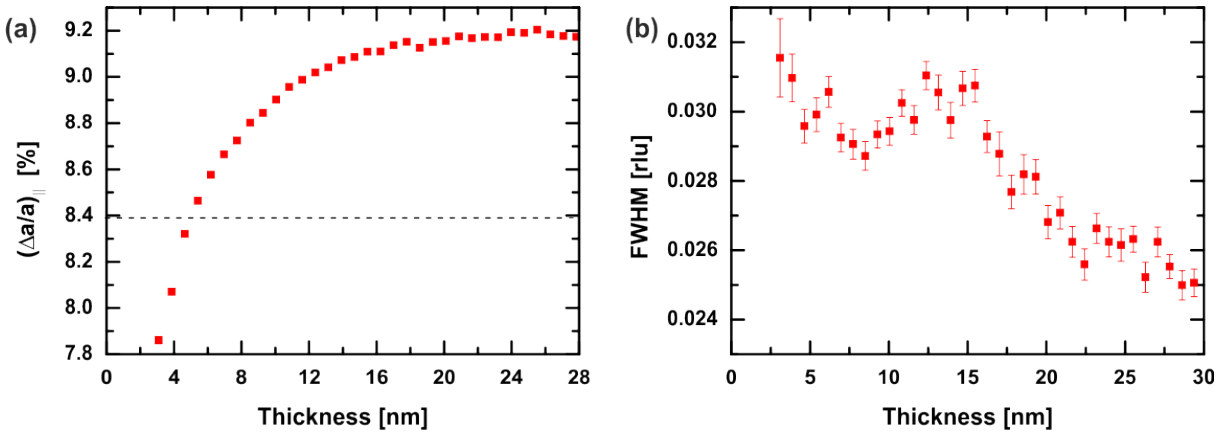

Figure 4.15: (a) In-plane mismatch with respect to thickness, dashed line shows the bulk mismatch and (b) change in FWHM with increase in thickness

in order to accommodate the smaller lattice constant of Si. As the film thickness increases, the strain decreases continuously with increase in thickness. Above a thickness of about 18-20 nm it completely relaxes and attains a final mismatch of 9.17% which is about 0.7% larger than the bulk value (see figure 4.15 (a)). For this reflection, the observed d-spacing of the epilayer is 2.4204 Å (bulk value: 2.4030 Å). The FWHM of the peaks during the growth decreases with increase in thickness indicating the increase in crystallite size as the growth proceeds (see 4.15 (b)).

4.4.3 *In-situ* Studies After Growth

Out-of-Plane Scan

Figure 4.16 (a) shows a KL reciprocal space map obtained using grazing incidence geometry. $\overline{K}$ is parallel to the $[11\bar{2}]$ direction. Along with the substrate Si($11\bar{1}$) reflection, few GeTe peaks are also observed, namely ($11\bar{1}$), ($22\bar{2}$) and ($33\bar{3}$) reflections. Apart from these main peaks, a couple of peaks corresponding to the twin reflections of GeTe (marked in red), namely ($\bar{1}\bar{1}3$) and (002) reflections are observed. The formation of twin defects is common in face-centred cubic related heterostructures,[125,126] including tellurides on Si(111)[127,128]. There are no polycrystalline rings observed out-of-plane. However, close to the GeTe$(002)_{twin}$ peak, there is an additional peak.

Azimuthal scan around this peak, shows the rotational domains normally observed for a GeTe

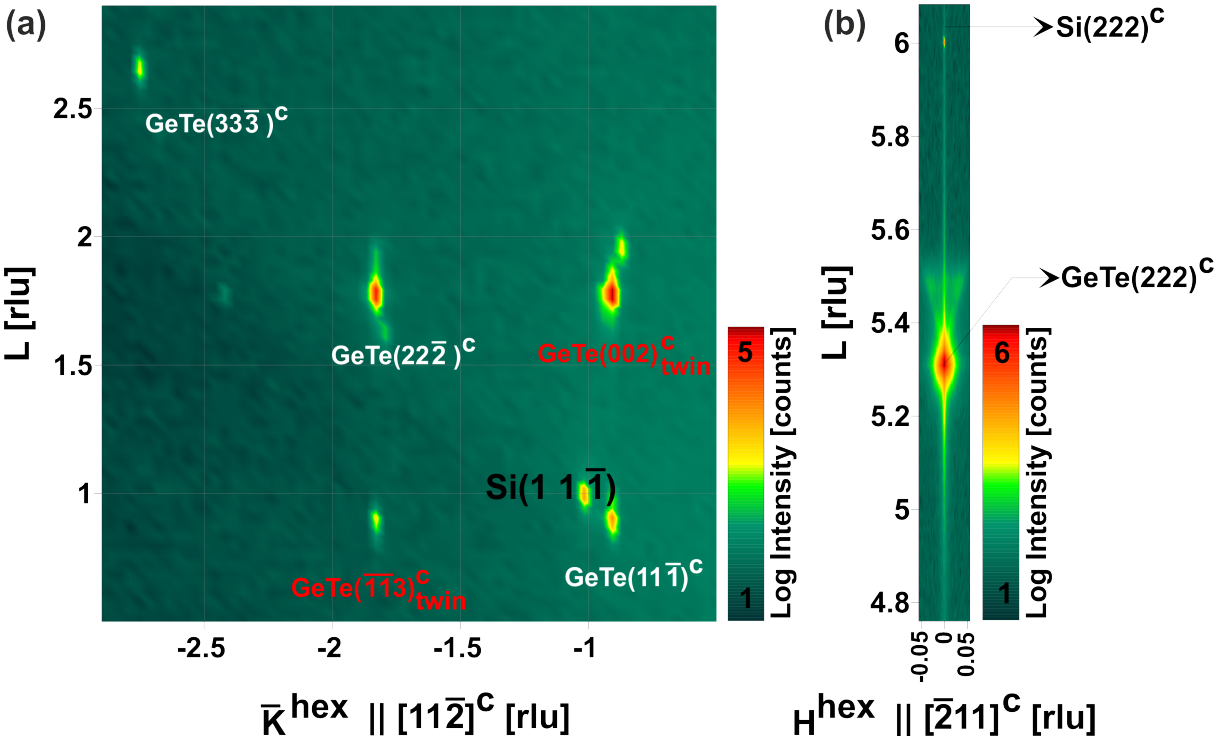

Figure 4.16: Out-of-plane RSM: (a) K versus L map in grazing incidence gemoetry

peak (as shown in figure 4.11 (a)) with a maximum separation of about ∼14° indicating that the signal comes from the GeTe film. The reason for the position of the peak to be at different in-plane and out-of-plane spacing is not clear. The possibility of it resulting from the rhombohedral distortion can not be excluded. Figure 4.16 (b) shows a RSM around the specular Si(222) Bragg peak with y-axis|||[111] and x-axis|||[$\bar{2}$11] directions. The sharp streak at H=0 corresponds to the Si CTR. It is observed that the GeTe(222) peak perfectly lies along the Si CTR indicating that, at least in this plane there is no lattice tilt between film and substrate, that is to say GeTe[111]|||Si[111].

In-Plane Scan

Figure 4.17 (a) shows an in-plane scan performed after growth under grazing incidence geometry along [11$\bar{2}$] direction. The scan cuts through the Si CTRs at K = -1 and -3 rlu. GeTe(22$\bar{4}$) peak observed at K ≈ -2.75 rlu corresponds to a mismatch of about ∼9.08% with respect to Si(22$\bar{4}$). The bulk GeTe value for (22$\bar{4}$) reflection is 1.2015 Å and the epilayer d-spacing as determined from the K scan for the corresponding reflection is 1.2095 Å. This shows that the epilayer has a larger d-spacing of about 0.66% than the bulk crystal and hence it is slightly tensely strained in-plane. A small peak is observed in figure 4.17 (a) close to K= -1.58 rlu, which is a polycrystalline feature of the GeTe(20$\bar{2}$) reflection. Line scan performed along a different azimuth|||[10$\bar{1}$] show a

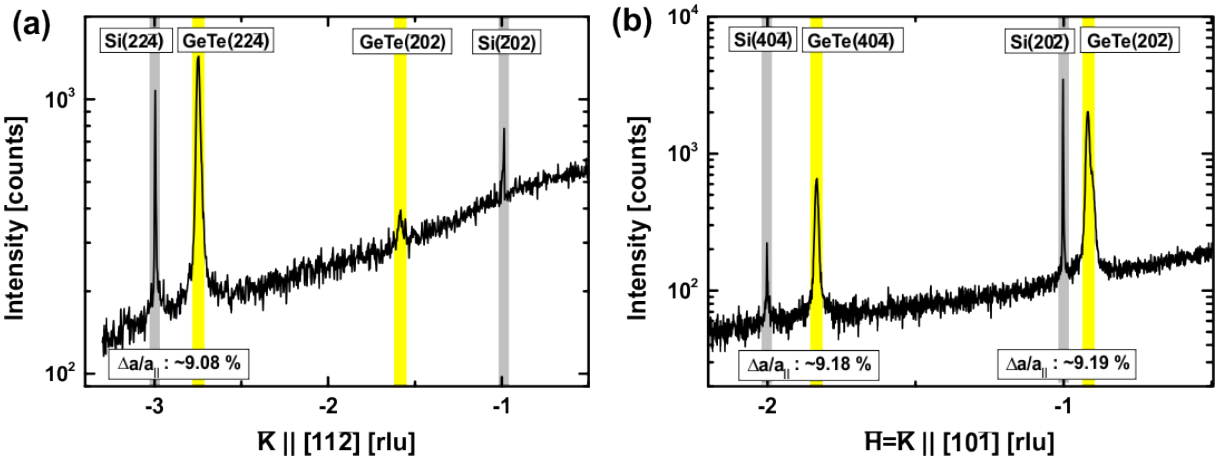

Figure 4.17: Grazing incidence in-plane scan along (a) [11$\bar{2}$] direction and (b) [10$\bar{1}$] direction

different mismatch (∼9.18%) in-plane as shown in figure 4.17 (b). The different mismatch can be attributed to the rhombohedral distortion of the GeTe film.

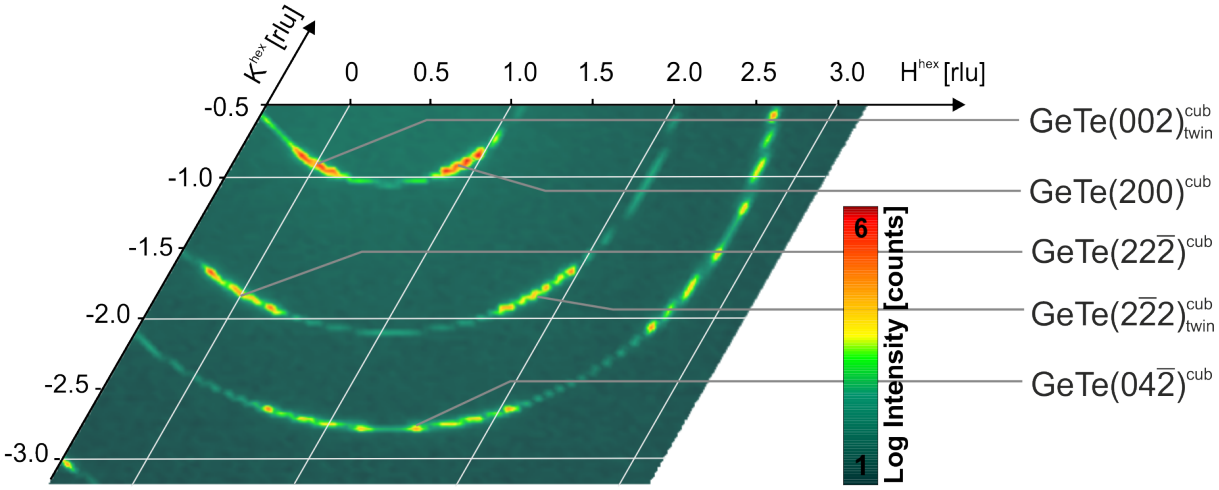

Figure 4.18: Grazing incidence in-plane map at L=2 rlu

Figure 4.18 shows a $H\overline{K}$ in-plane map measured in the grazing incidence geometry. The map is measured at L = 2 rlu. The rotational domains are observed in-plane and a very weak polycrystalline feature is also observed. However, the intensity of the polycrystalline feature is almost two orders of magnitude lesser (see figure 4.19) than the main GeTe diffraction peaks indicating almost <1% of the film to be polycrystalline. The peak positions are given in cubic coordinates and are shown in figure 4.18. For an azimuthal rotation of every 60°, a peak appears and the corresponding reflections are assigned by a subscript twin to differentiate between untwinned and 180° rotated twinned domains. The observed intensity ratio between

the twinned and untwinned domains is found to be 45:55, indicating 45% of twin domains in the crystal. The 30° rotation domains observed in RHEED can be explained by the low intense

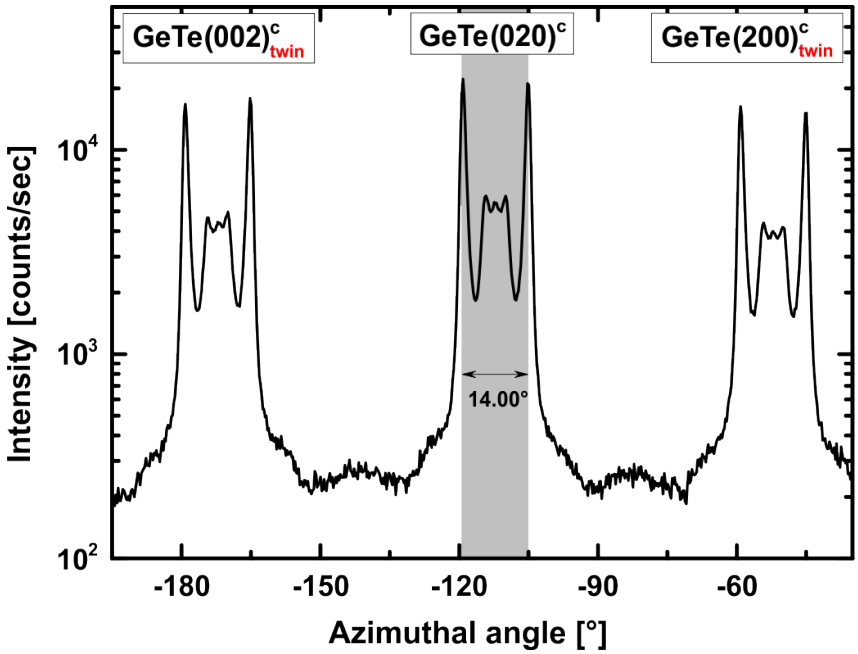

Figure 4.19: Azimuthal scan of the GeTe(020) reflection. Twins are observed for a rotation of 60° on both directions. The intensity of the untwinned and twinned peaks are in the ratio 45:55. The rotational domains have a separation of about 14° between their extremes

peak (also seen as polycrystalline ring in figure 4.18) between the two strong peaks observed every 60°.

4.5 Compositional Analysis

A series of samples at different substrate temperatures were grown for a duration of 200 minutes. The nominal film thickness were between 50-70 nm, and the growth rate varied betweeen 0.25-0.35 nm/min depending on the substrate temperatures. The film composition was measured by x-ray fluorescence (XRF). A sample grown at room temperature to determine the initial flux conditions showed a Ge content of ∼31.4 % and Te content of about ∼68.6 %. Interestingly samples grown at higher substrate temperatures (in the epitaxial regime) show that the composition is almost independent of the substrate temperature yielding a Ge:Te atomic ratio of about 46:54 %. The sticking coefficient of different species is determined by opening the sources at high substrate temperature, where nothing sticks on to the substrate. The substrate temperature is ramped down till complete sticking occurs, and the corresponding QMS desorption signal is plotted as a function of substrate temperature. The sticking coefficient for Ge, Te and GeTe are shown in the desorption versus temperature curve shown (see figure 4.20). Where

1 represents maximum desorption (negligible sticking) and 0 represents negligible desorption (maximum sticking) of the atomic/molecular species. Te has a very low sticking coefficient at temperatures greater than 200 °C as can be seen in the figure 4.20. At these temperatures corresponding to the usual GeTe epitaxial growth window, only Te atoms which bond with Ge stay on the surface and the remaining Te atom desorb. Thus, Ge acts as growth limiting species and a stoichiometric compound is formed as long as an excess of Te is present. This growth is similar to most III-V semiconductor materials[129]. Compositional analysis agree with the fact that even though an excess of Te is supplied, the composition is $Ge_{0.46}Te_{0.54}$ irrespective of the substrate temperatures within the epitaxial growth window. Analysis of a bulk GeTe crystal also showed a composition of $Ge_{0.46}Te_{0.54}$[3]. Further epitaxial sample grown using MBE from a GeTe molecular source also exhibited the same compositional results[4], indicating that this might be the stable composition of the GeTe crystal irrespective of the flux condition or substrate temperatures. It is interesting to note that, the composition is non-stoichiometric. GeTe

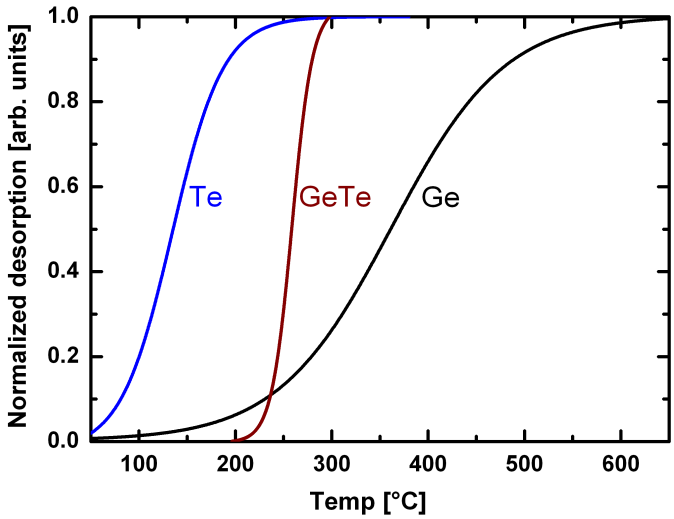

Figure 4.20: Sticking/desorption curve for different species as observed by a QMS. The maximum desorption is normalized to 1.

crystals with exactly 50:50 composition do not exist[28] and in the case of sputtered films, always a small fraction of segregated Ge atoms is present in the GeTe film[21]. Structural studies on GeTe show that Te fully occupies one sublattice and Ge/vacancies randomly occupy the other sublattice[39,40]. From the compositional measurements, we can infer that there are 8 vacancies for every 54 Te atoms, or in short the vacancy concentration is about 14.8% , which is in close agreement with the experimental and theoretical results[21,22,130,131].

[3]Courtesy: Max-Planck-Institut für Metallforschung, Stuttgart
[4]Private communication with Mahmood Hassan, University of Linz

4.5.1 Compositional Analysis using QMS

The stable composition of the epitaxial GeTe allow us to calibrate the QMS for *in-situ* composition analysis. We perform the growth at a high substrate temperature where nothing sticks on to the substrate as seen by the RHEED. This maximum desorption is taken as a reference. The growth is performed by lowering the substrate temperature where the GeTe starts to stick onto the substrate. The desorption during the growth is monitored by the QMS and the background is subtracted using a computer program written in Java^{TM} (see Program Code). The difference between the maximum desorption and the desorption during growth gives the incorporating flux onto the substrate as depicted in Figure 4.21. At the end of the growth, the average incorpo-

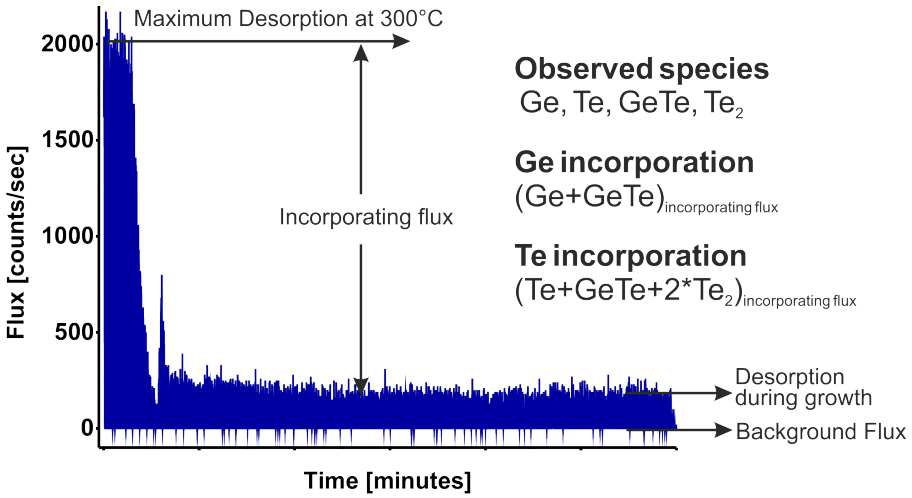

Figure 4.21: Schematic diagram depicting the maximum desorption, background signal and incorporating flux

rating flux in counts/second of each species observed i.e., Ge, Te, GeTe, Te_2 is used to find the composition. Ge incorporation is given by the sum of Ge and GeTe, while the Te incorporation is given by the sum of Te, GeTe and twice Te_2. Since GeTe contains one atom of Ge and one atom of Te, we add it for both Ge and Te incorporation and same is the case for Te_2 as each molecule constitutes two atoms. The sensitivity of different atomic species are not the same and the position of the source cells also affects the amount of material detected by the spectrometer as reported by Celii et al[?] . There are two options, either to account for the change in sensitivity of the atomic/molecular species by multiplying it with a factor or we can account for the different amount of material observed by the mass spectrometer due to its relative position in the MBE chamber. Either way, the principal aim is to calibrate the QMS data with the XRF measurements to use it as a tool for *in-situ* compositional analysis. We asssume the sensitivity of the atomic species with atomic mass greater than 150 amu to be less than 1. So for GeTe,

Temperature (°C)	**XRF** (atomic %)		**QMS** (atomic %)	
	Ge	Te	Ge	Te
20	31.39 ± 0.07	68.61 ± 0.03	33.38	66.62
204	45.96 ± 0.05	54.04 ± 0.03	47.55	52.45
220	45.89 ± 0.08	54.11 ± 0.02	45.30	54.70
253	45.92 ± 0.05	54.08 ± 0.03	46.51	53.49

Table 4.3: Compositional analysis of GeTe using XRF and its calibration using a line-of-sight QMS

which has an atomic mass of 200.24 amu, a factor of 1.2 is multiplied and for Te_2 which has 255.2 amu, it is multiplied with a factor of 1.3. The resultant mass spectrometric singal ratio is presented in the table 4.3. For the case of amorphous sample grown at room temperature, no mass spectrometric data is available. Hence the average of the maximum desorption data from the other three samples are taken to calculate the composition (desorption is zero for room temperature growth). From the table, we observe that the composition found by calibrating the QMS is in close agreement with the XRF results with an error percentage of less than 5%.

4.6 Conclusions

A line-of-sight QMS was used to study the quantitative etching property of Ge using Te. The etching studies indicate that Ge can act as a limiting flux for the growth of GeTe thin films. It was demonstrated that GeTe thin films can be grown epitaxially on largely mismatched Si(111) and Si(001) substrates. During the nucleation stage, an initial amorphous-to-crystalline incubation stage is observed from the RHEED pattern on both Si(111) and Si(001). Interestingly, on both substrate orientations, GeTe prefers to grow only along the [111] orientation as observed by specular $\omega - 2\theta$ scans. This indicates that the substrate orientation does not influence the growth direction. Azimuthal RHEED scans during GeTe growth on Si(111) show a weak diffuse four fold symmetry during the nucleation stage before it turns to six-fold symmetry with the presence of twins and rotational domains. Specular scan along the [111] direction shows peaks at half Bragg positions, indicating a superstructure during the nucleation stage, which disappears once the film starts to grow along [111] orientation. The surface morphology shows flat triangular islands with a rms roughness of about ∼5 nm. Rotational domains are present and give rise to five symmetrically arranged maxima observed right from the amorphous-to-crystalline transition. The separation between the two extremes is a function of layer thickness. The observed multi-domain epitaxy is tentatively attributed to the fact that the actual structure of the grown GeTe epitaxial layer deviate from the ideal rocksalt structure, in that the unit cell is rhombohedrally distorted and the Ge sublattice contains vacancies. Additionally twins rotated by 180° around the epitaxial layer are detected. *In-vivo* out-of-plane studies during growth show that the lattice mismatch increases rapidly during nucleation stage and decreases above a thickness of 3 nm. Larger lattice mismatch (13.48%) along [111] direction and smaller lattice mismatch (9.17%) along $[\bar{2}11]$ direction with respect to Si indicate distortion of the unit cell. Samples grown within the epitaxial window show a composition of $Ge_{0.46}Te_{0.54}$ irrespective of

the substrate temperatures. The XRF results were used to calibrate a line-of-sight QMS to perform *in-situ* compositional analysis and the composition was found to be within an error percentage of less than 5%.

5 Epitaxial Growth of Sb_2Te_3

Sb_2Te_3 displays fast crystallization time at low temperatures, and this implies poor thermal stability of the amorphous phase. However, it is reported that Sb_2Te_3 crystalline templates reduce the crystallization temperature and enhances the crystallization speed of GeTe by up to four orders of magnitude[118]. Simpson et al., proposed that the Ge atoms lying at the Sb_2Te_3 interface form nucleation centers by switching to octahedral positions, thereby reducing the nucleation time and enhancing the switching speed. The principle is similar to that of GeTe$-Sb_2Te_3$ superlattice structures, where switching with lower energy consumption is explained by the reduced movement of Ge atoms at the interfaces[15].

From the growth point of view, the complications involved in growing a ternary compound can be understood and overcome, if the growth properties of the binary alloy are investigated and studied. Different growth mechansims for fabricating Sb_2Te_3 thin films are widely in use such as thermal evaporation from Sb_2Te_3 target[132], coevaporation from atomic sources[133,134], atomic layer epitaxy[135], electrochemical co-deposition[136], MOCVD[137] and MBE[64,65,138]. Among these techniques MBE growth has superior control over the crystalline quality. The high quality obtained in our layers allowed to measure topological insulating properties[66]. Here we present the epitaxial growth of Sb_2Te_3 on Si(111).

5.1 Growth of Sb_2Te_3

Si(111) substrates were cleaned using the standard procedure discussed in section 3.4 before loading them into the MBE chamber and 7×7 reconstructed. Highest purity Sb and Te were evaporated from standard effusion cells. The Sb and Te effusion cell base/hotlip temperatures were set to (470/620) and (340/476) °C respectively. The corresponding fluxes were estimated by measuring, with *ex-situ* XRR, the thickness of amorphous Sb and Te samples deposited at room temperature to ensure complete sticking of the impinging species. The Sb and Te growth rates were found to be ∼0.12 nm/min and ∼0.31 nm/min respectively, yielding a Sb:Te flux ratio of 2:5. The growth process was followed in real time by means of *in-situ* RHEED and a line-of-sight QMS.

In order to determine the growth window of the two species, Sb and Te are deposited individually and then later together (for Sb_2Te_3). The substrate temperature is slowly ramped from high (maximum desorption of the species) to low (minimum desorption). Figure 5.1 shows the fit to the normalized desorption signal of various species during temperature ramp down at 0.1 °C/s. The curve between maximum and minimum desorption gives the approximate epitaxial growth window. The temperatures mentioned here are measured by a non-contact thermocouple, and a temperature error of about ±30 °C is expected at these growth temperatures[116]. We could observe that Sb_2Te_3 has a narrow epitaxial growth window between 200-260 °C. The growth

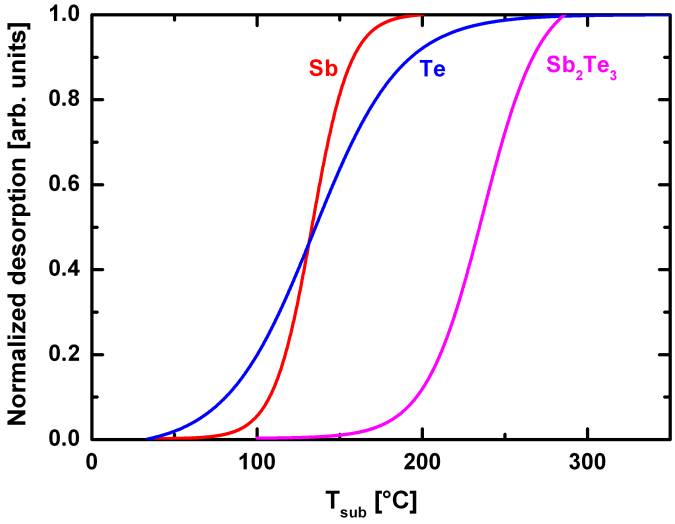

Figure 5.1: Fit to the desorption signal as observed for Sb, Te and Sb_2Te_3 from a line-of-sight QMS as a function of T_{sub}. Maximum desorption of each species is normalized to 1

occurs at T_{sub} where Sb and Te atoms singularly do not stick, but as a molecule they remain stable on the surface to form epitaxial layers.

T_{sub} was set at 220 °C and at this temperature, the growth rate is about 0.42 nm/min. Both Sb and Te shutters are opened simultaneously to start the growth. Figure 5.2 shows the RHEED pattern at important stages of growth, with the electron beam incident on the surface along the $[1\bar{1}0]$ direction. Figure 5.2 (a) shows the initial Si(111) surface 7×7 reconstructed with Kikuchi patterns indicating surface of high crystalline quality. Contrary to GeTe, as soon as the growth proceeds there is a smooth transformation from the substrate to the layer reflection as can be seen in figure 5.2 (b), where both Si and Sb_2Te_3 reflections are present. Analysis of the relative peak positions from the line profile shown in figure 5.2 (c) during this stage gives a lattice

Si		**Sb_2Te_3**		**Lattice Mismatch**
reflection	d-spacing [Å]	reflection	d-spacing [Å]	
$(2\bar{2}0)_{cubic}$	1.9200	$(\bar{2}10)_{hex}$	2.1320	11.04 %
$(\bar{4}22)_{cubic}$	1.1085	$(300)_{hex}$	1.2309	11.04 %
$(111)_{cubic}$	3.1354	$(009)_{hex}$	3.3842	7.94 %

Table 5.1: Lattice mismatch of bulk Sb_2Te_3 with Si.

mismatch of about ∼11.01% (see figure 5.2 (d)) along $[1\bar{1}0]$ direction, which is close to the bulk value (see table 5.1). Streaky diffraction pattern is observed till the end of the growth (after 200 minutes) indicative of smooth crystalline surface morphology. The final RHEED pattern along $<1\bar{1}0>$ and $<11\bar{2}>$ azimuth are shown in figure 5.2 (e) and (f), respectively. The same

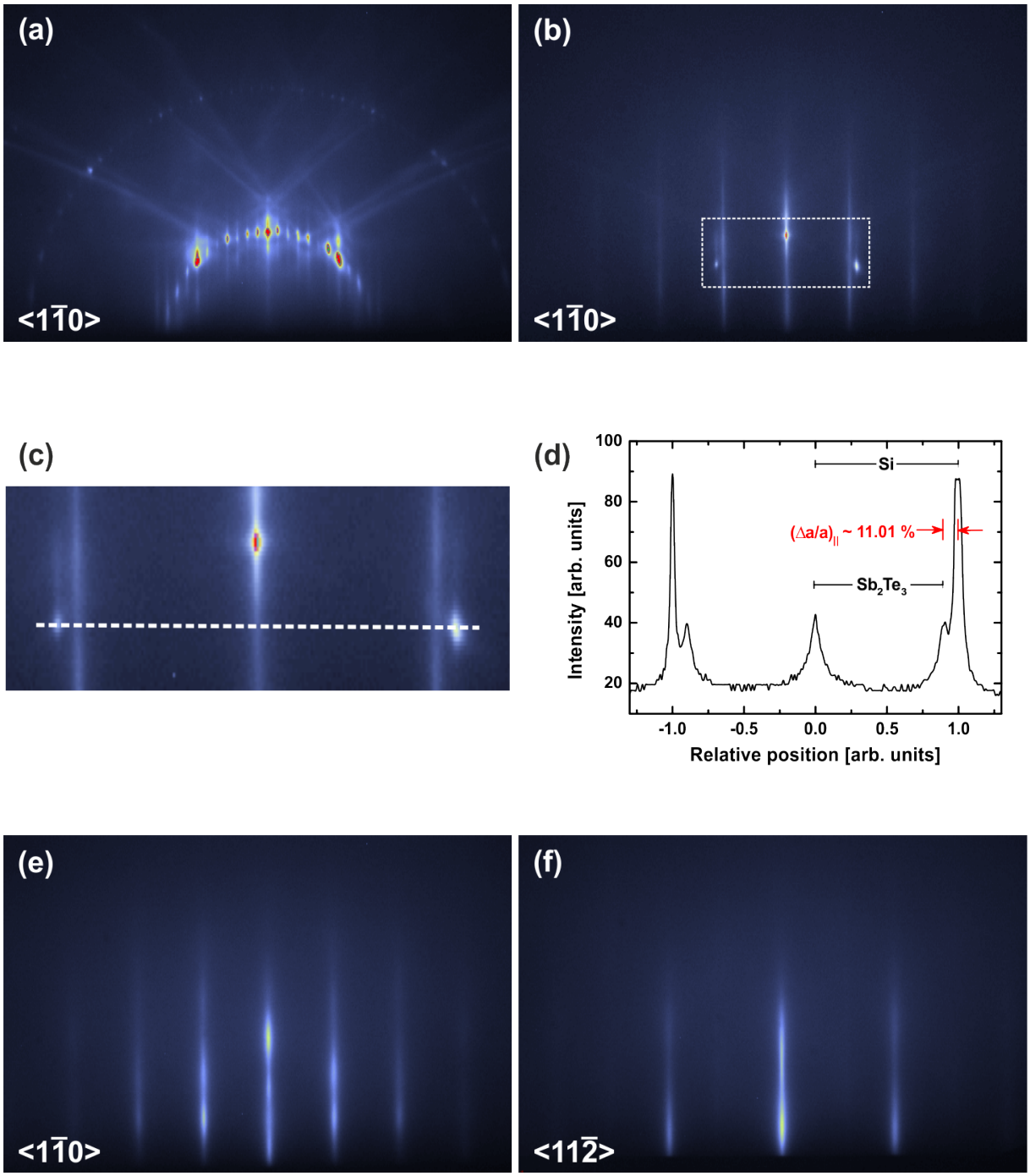

Figure 5.2: RHEED evolution during various stages of growth along <1$\bar{1}$0> azimuth of (a) the Si(111) 7×7 surface; (b) deposition of <1 nm of Sb_2Te_3; (c) a zoom of the rectangular section shown in (b); (d) line profile (dotted line in (c)) during initial stages of Sb_2Te_3 growth; (e) and (f) are the final surface of Sb_2Te_3 epitaxial layer along <1$\bar{1}$0> and <11$\bar{2}$>, respectively. The final surface shows a 1×1 reconstruction

pattern appears for rotation of every 60°, indicating a six-fold symmetry and the presence of 1×1 reconstruction.

The RHEED pattern shows intensity modulations along the streaks, which might be due to the following two reasons. For the case of rough films, whose surfaces have multi-level terraces with different widths, the RHEED pattern displays intensity modulation along the streaks with strong intensity close to the Bragg points and weak intensity close to the off-Bragg regions [139]. The other possibility might be the presence of a fiber oriented film. In this case, the out-of-plane orientation is unique, while the in-plane orientation is randomly distributed, resulting in a fibre-like crystal. It is possible that the different domains have different heights and consequently the diffraction pattern arises from interferences perpendicular to the surface which give rise to intensity modulation along the streaks [140].

5.2 Surface Morphology

The streaky RHEED pattern cannot be taken as a conclusive evidence for surface morphology, as large atomically flat islands might contribute to streaky pattern. XRR investigation is therefore accomplished. Figure 5.3 shows a typical XRR curve of Sb_2Te_3 deposited on Si(111). Oxidation

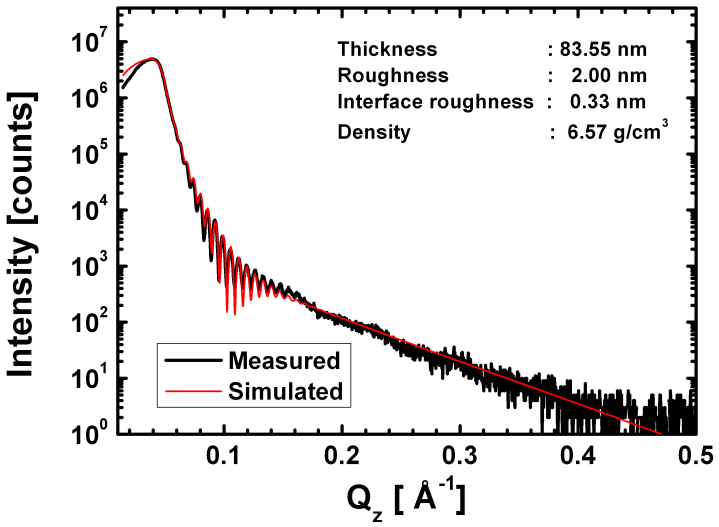

Figure 5.3: X-ray reflectivity of Sb_2Te_3 grown on Si(111). Kiessig fringes are observed, implying a smooth surface morphology

of the Sb_2Te_3 film is possible upon exposure to air. However, we expect a rather thin oxide on top, and the XRR curve was fitted with only a single layer (Sb_2Te_3) on the substrate (Si). From the analysis of the XRR curve, we obtained a film density of about $\sim$6.57 g/cm^3 which is close to the bulk density of Sb_2Te_3 [57]. The interface roughness is about $\sim$0.33 nm indicating a smooth interface between the layer and the substrate. The surface roughness of the film is found to be

about ∼2 nm. Thickness as determined from the Kiessig fringes is about ∼83.55 nm.

A series of samples were grown at different T_{sub} to investigate surface roughness changes with temperature. Figure 5.4 shows epitaxial Sb_2Te_3 (a-d) layers grown at different T_{sub}. At low growth temperatures (T_{sub} = 200 °C), large number of islands with crystallite size of the order of 100-150 nm are present with a rms roughness of 2.13 nm (see figure 5.4 (a)). As the growth temperature is increased (T_{sub} = 210, 220 °C), the crystallite size (200-300 nm) increases with the reduction in the concentration of islands and its roughness (see figure 5.4 (b, c)). At high temperature (T_{sub}= 240 °C), large flat islands are observed with crystallite size of the order of 500-700 nm with rms roughness of <1 nm. These analysis suggest that, the growth at high T_{sub} is more favourable for fabricating smooth epilayers with reduced concentration of islands.

5.3 X-ray Diffraction

Figure 5.5 shows a specular $\omega - 2\theta$ XRD scan to determine the out-of-plane orientation of the Sb_2Te_3 epitaxial film. The sharp features at q_z= 2.000, 4.002 and 6.004 Å^{-1} correspond to the Si(111), (222) and (333) substrate reflections respectively. The remaining 11 peaks correspond to a set of Bragg reflections along 'c' direction and their respective peak positions are assigned in hexagonal coordinates (00.L) as shown in figure 5.5 (a)[1]. There are no additional out-of-plane reflections, indicating unique orientation of the crystal in this direction. Figure 5.5 (b) shows a zoom of the specular rod close to Si(111) reflection. Laue oscillations are observed indicating high-crystalline quality of the film. From the spacing of the interference fringes, a thickness of about 24 nm is estimated. The out-of-plane lattice constant along 'c' direction is found to be about 30.4034 Å from the specular rod scan. This is about ∼0.18% smaller than the bulk lattice parameter, which is reported to be about 30.4580 Å[57].

Figure 5.6 shows the symmetric (a) and asymmetric (b) RSMs close to Si(111) and Si(224) reflections respectively, where $Q_{||}||[11\bar{2}]$ and $Q_{\perp}||[111]$. The RSMs are measured using an analyzer crystal to have better resolution. The lattice peak position of Si(111) in symmetric RSM is observed at $Q_{||}$= 0, $Q_{\perp}$= 2.00 Å^{-1}. While the Sb_2Te_3(00.9) lattice peak is observed at $Q_{||}$= 0, $Q_{\perp}$= 1.8465 Å^{-1}. Both the peak positions are observed at $Q_{||}$= 0 indicating that there is no lattice tilt between the film and substrate and the film CTR lie perfectly along the Si CTR. Analysis of the peak positions of the asymmetric RSM shows that the Si(224) reflection is at $Q_{||}$=1.8867, $Q_{\perp}$=5.3380 Å^{-1}. Apart from the main Si peak, four other peaks are observed and they all lie along the same $Q_{||}$ value at 1.697 Å^{-1}, while the $Q_{\perp}$ values of the four peaks are at 3.393, 4.170, 4.731 and 5.774 Å^{-1} corresponding to a d-spacing of 1.467, 1.395, 1.250 and 1.044 Å respectively. These d-spacing matches closely with the bulk values of $Sb_2Te_3(0\bar{1}.19)$,(01.20),(01.23) and $(0\bar{1}.28)$ reflections. For a single crystalline sample, only the (01.20) and (01.23) reflections would be available, the two more reflections indexed in red (see figure 5.6 (b)) arise from the 180° rotational domains or twins. The dashed line in the figure 5.6 (b) shows complete relaxation line. From the out-of-plane lattice constant and the d-spacings of the asymmetric reflections, the in-plane lattice constant of Sb_2Te_3 is found to be about 4.2804 Å, which is 0.38% larger than

[1] Sb_2Te_3 exhibits hexagonal crystal structure with a space group $R\bar{3}m$. The reflection conditions for diffraction maxima ($-h + k + l$= 3n, where n is an integer) along [00.l] direction is l = 3n.

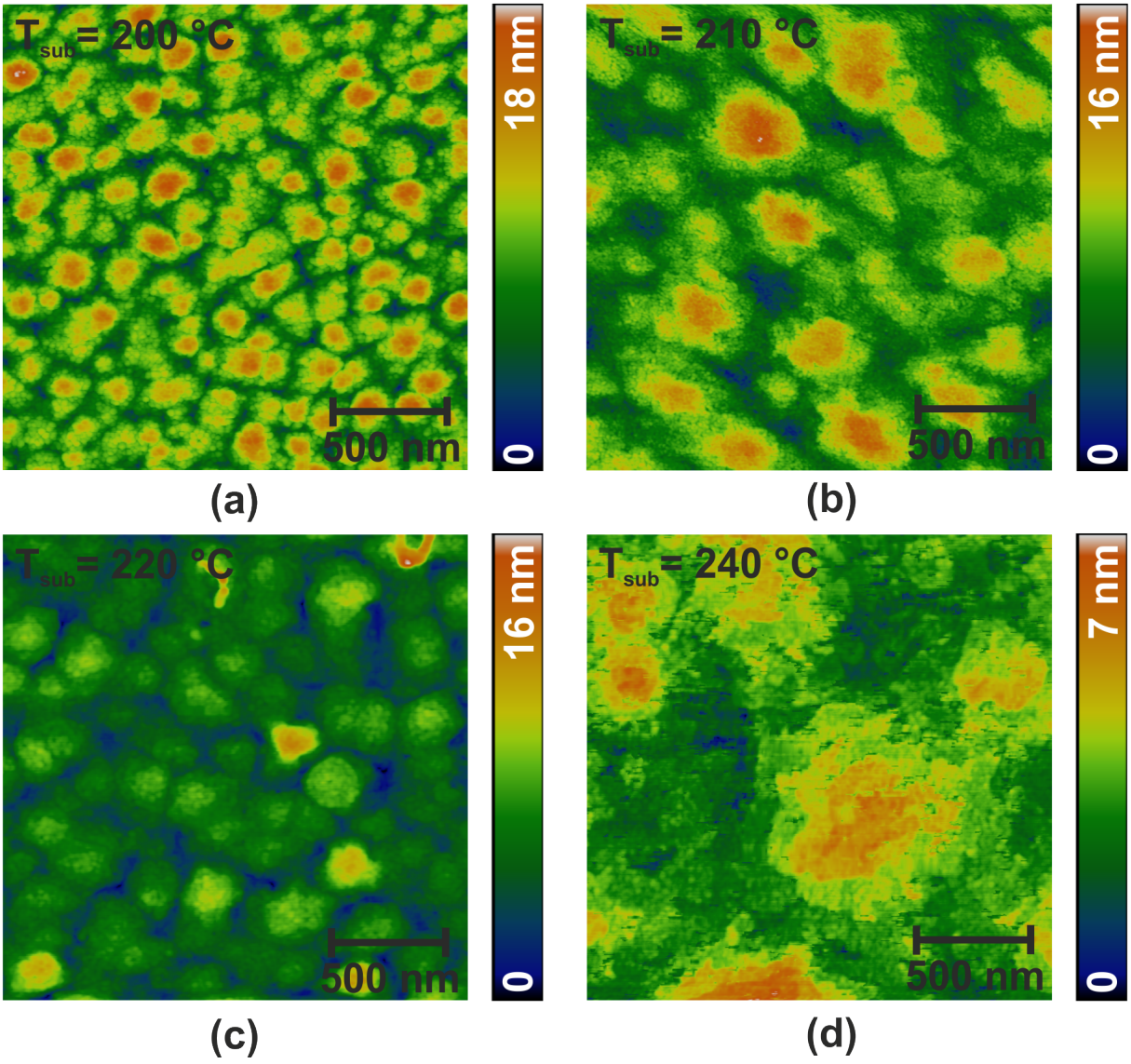

Figure 5.4: Surface morphology as observed by AFM: (a) T_{sub}= 200 °C, rms roughness= 2.42 nm, (b) T_{sub}= 210 °C, rms roughness= 2.13 nm, (c) T_{sub}= 220 °C, rms roughness= 1.66 nm, (d) T_{sub}= 240 °C, rms roughness= 0.92 nm

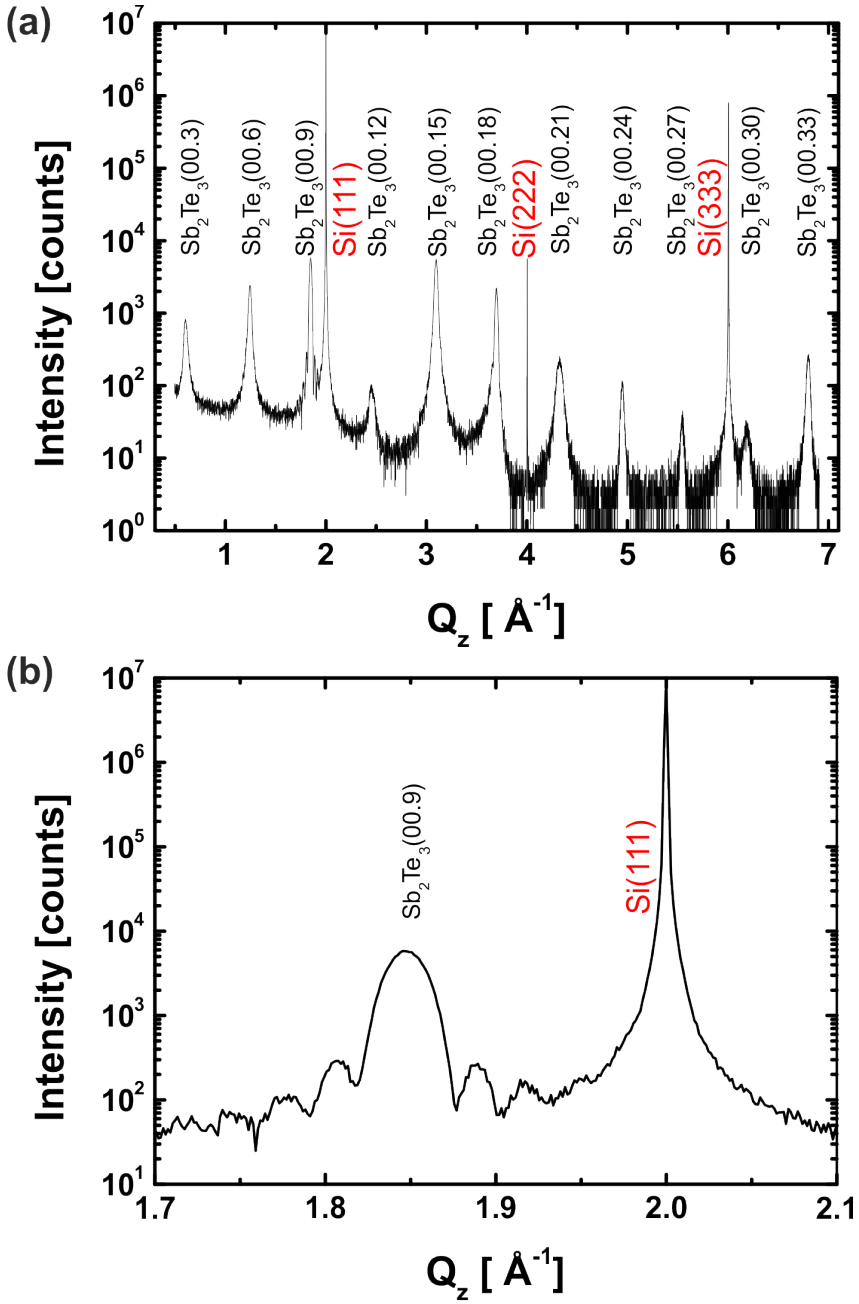

Figure 5.5: $\omega - 2\theta$ scan of Sb_2Te_3 grown on Si(111). The film grows along 'c' direction out-of-plane. (a) Wide range diffraction pattern along the specular CTR with the film reflections indexed in black and the substrate reflections in red, (b) Laue oscillations observed along Sb_2Te_3 reflection inidicate thickness of about ∼24 nm

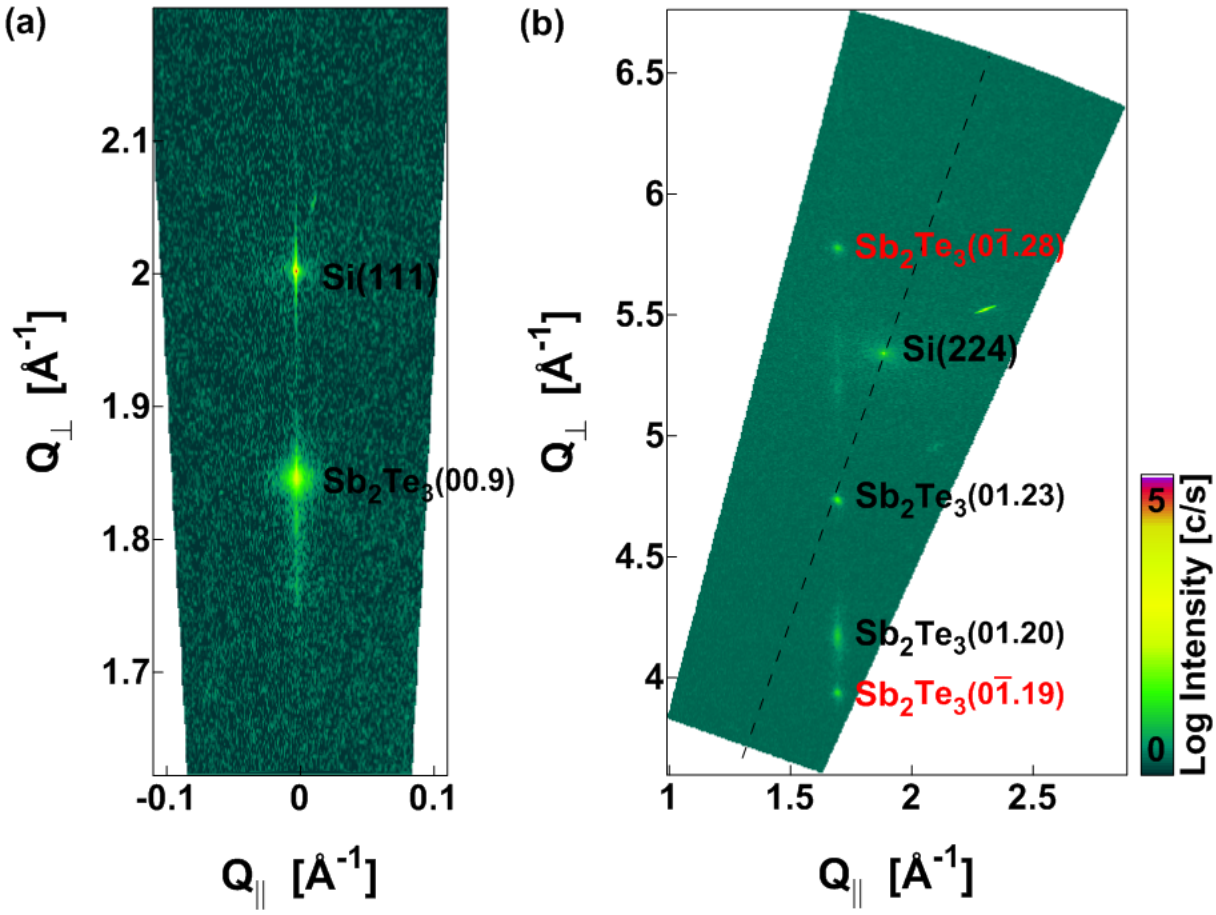

Figure 5.6: RSMs around the symmetric Si(111) (a) and the asymmetric Si(224) (b) Bragg peaks with $Q_\perp$||Si[111] and $Q_{||}$||Si[11$\bar{2}$]

the bulk lattice parameter (4.264 Å)[57]. This indicates that the film is slightly tensely strained in-plane.

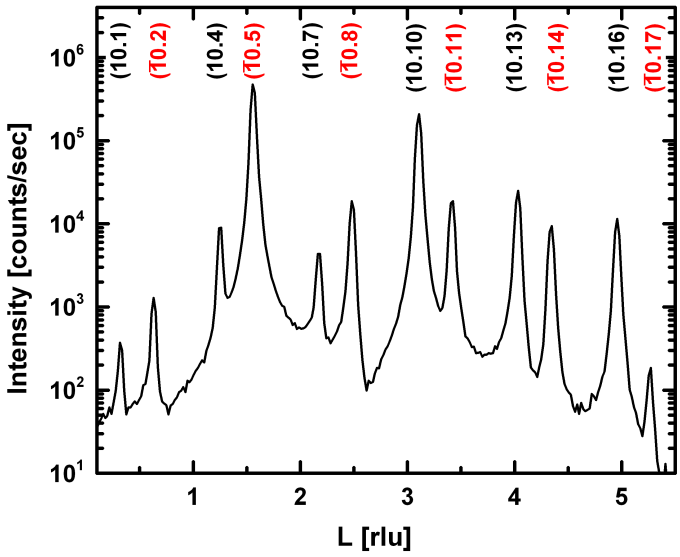

Figure 5.7: (10.L) CTR of Sb_2Te_3 grown on Si(111). Twin reflections marked in red are observed in addition to the main reflections

Figure 5.7 shows the (10.L) CTR scan performed in grazing incidence geometry. As seen from the asymmetric reciprocal map, this scan also shows the presence of twins, which are indexed in red. Apart from the twin reflections present in the CTR, there are no other polycrystalline features observed indicating the unique out-of-plane orientation of the film. The presence of only certain peaks which obey the condition for diffraction maxima of a hexagonal crystal system ($-h + k + l = 3n$, where n is an integer), also further indicates that the grown Sb_2Te_3 epilayer is hexagonal.

5.3.1 Azimuthal Scan

To investigate the in-plane symmetry of the Sb_2Te_3 film, the substrate was aligned to peak with the maximum intensity observed in the (10.L) CTR scan, which is $(\bar{1}0.5)$ reflection. Azimuthal scan around this peak is shown in figure 5.8. Peaks are observed every 60°, indicating a six-fold symmetry. However, by carefully looking at it, 3 peaks are visible on either side from the main diffraction peak. In total 7 peaks are present. The peak positions are fitted using a Gaussian function as shown in the figure 5.8 (b). Where the blue curves are the Gaussian fits of individual peaks and the red curve is the combined fit of all the peaks. In terms of azimuthal angle, the first two subpeaks are separated by an angle of 6.5° from the central one and the second set by 16°, whereas the third set by 30°. This indicates a strong mosaicity of the film in-plane and a

preferential rotation of the domains at certain angles. Apart from the 6-fold symmetry observed

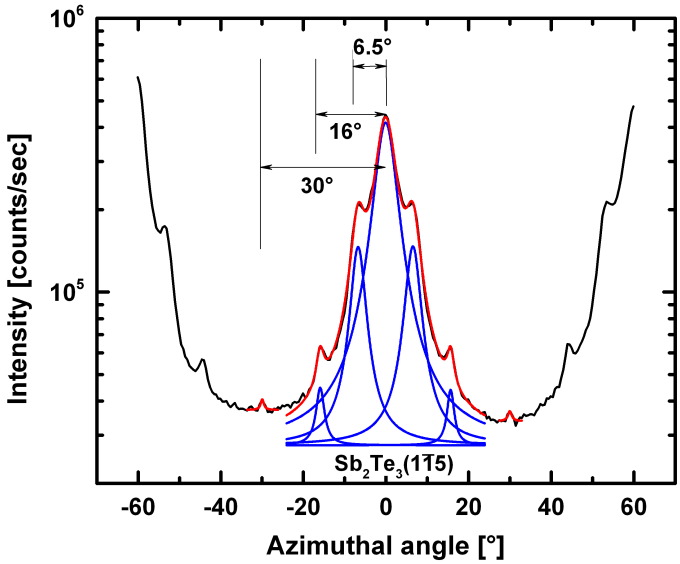

Figure 5.8: Azimuthal scan around the Sb_2Te_3 reflection: each peak consists of 7 sub-peaks. The first pair of peaks are separated by 6.5°, the second pair by 16° and the third pair of peaks by 30° from the central reflection. Every 60° an intense peak is observed indicating twins

from the azimuthal scan, rotation domains appear at smaller angles. Narayan et al. [123], proposed that the epitaxy of thin films having large mismatch with respect to the substrate are expected to exhibit domain matching epitaxy, in which the film aligns itself along different orientations on the substrate in order to accommodate for the large in-plane misfits [120,123,141,142]. Grey et al., [143] formulated an equation to determine the angle of rotation for growth on highly mismatched substrates based on the lattice mismatch between the adsorbate and substrate. The angle of rotation of the domain lattice with respect to the substrate lattice is given by:

$$\cos\theta = r_{AS}\sin^2\psi_S\sqrt{1 - r_{AS}^2\sin^2\psi_S} \tag{5.1}$$

Where θ is the rotation angle, r_{AS} is the ratio of the absorbate to substrate lattice parameters and ψ_S is the high-symmetry rotation angle of the domain lattice with respect to the adsorbate. θ can be expressed similarly in terms of $r_{SA} = 1/r_{AS}$ and the rotation of the domain with respect to the substrate (ψ_A) as:

$$\cos\theta = r_{SA}\sin^2\psi_A\sqrt{1 - r_{SA}^2\sin^2\psi_A} \tag{5.2}$$

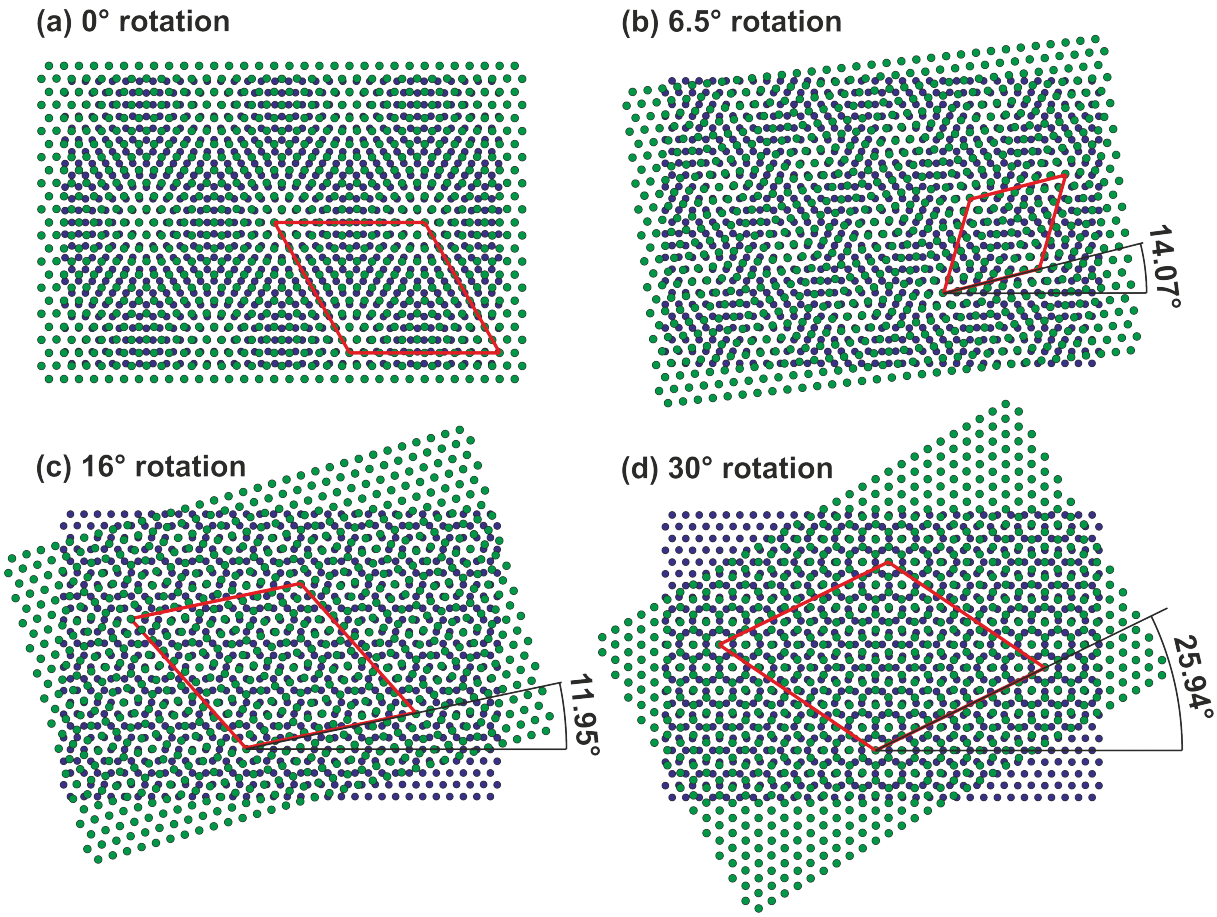

Figure 5.9: Moiré pattern for domains rotated by (a) 0°, (b) 6.5°, (c) 16° and (d) 30°. Blue dots represents the lattice points of the substrate and green that of the adsorbate. Red rhombus corresponds to the unit cell observed in the moiré pattern. The domain structures in the moiré pattern are rotated by (a) 0°, (b) 14°, (c) 12° and (d) 26° with respect to the substrate

In the case of Sb_2Te_3 growth on Si(111), both the substrate and adsorbate have triangular lattices with high-symmetry rotation angles (ψ_S, ψ_A) of 30°, 60° and 90°. The solutions for equation 5.1 for 30°, 60° and 90° high symmetry rotation gives θ values of 3.21°, 8.68° and 25.65°, respectively. Equation 5.2 give θ value of 3.69° and 13.89° for high symmetry rotation angles of 30° and 60°, respectively.

Figure 5.9 shows the moiré pattern expected for the experimentally observed rotation angles of the adsorbate with respect to the substrate. Green and blue lattice points corresponds to the adsorbate and substrate, respectively. Figure 5.9 (a) shows the unrotated domain. 11 lattice points of Sb_2Te_3 coincides with 12 lattice points of the substrate. Figure 5.9 (b) shows the 6.5° rotated domain with the moiré pattern rotated by 14°. Figure 5.9 (c) and (d) are the 16° and 30° rotational domains with the moiré patterns rotated by 12° and 26°, respectively.

For the growth of epitaxial Sb_2Te_3 on Si(111) substrates, both the solutions of the equations proposed by Grey et al.,[143] neither match with the experimentally observed rotation angles, nor rotates the moiré pattern by the high symmetry angles. A different theoretical approach is thus necessary to predict the observed rotation angles, however it is beyond the scope of this work.

5.3.2 In-plane Reciprocal Space Map

Along with out-of-plane diffraction, in-plane RSMs gives the over all picture of the crystal structure and its orientation. Figure 5.10 shows the $H\overline{K}$ RSM taken at L=0 under grazing incidence geometry. The Si substrate reflections in cubic coordinates are indexed in red and the layer reflections in hexagonal coordinates are given in black. Strong polycrystalline features are observed as can be seen in the figure, with the intenstiy ratio of the peak and background in the ring of about 16%. As discussed in the previous section 5.3.1, due to the large misfit of the

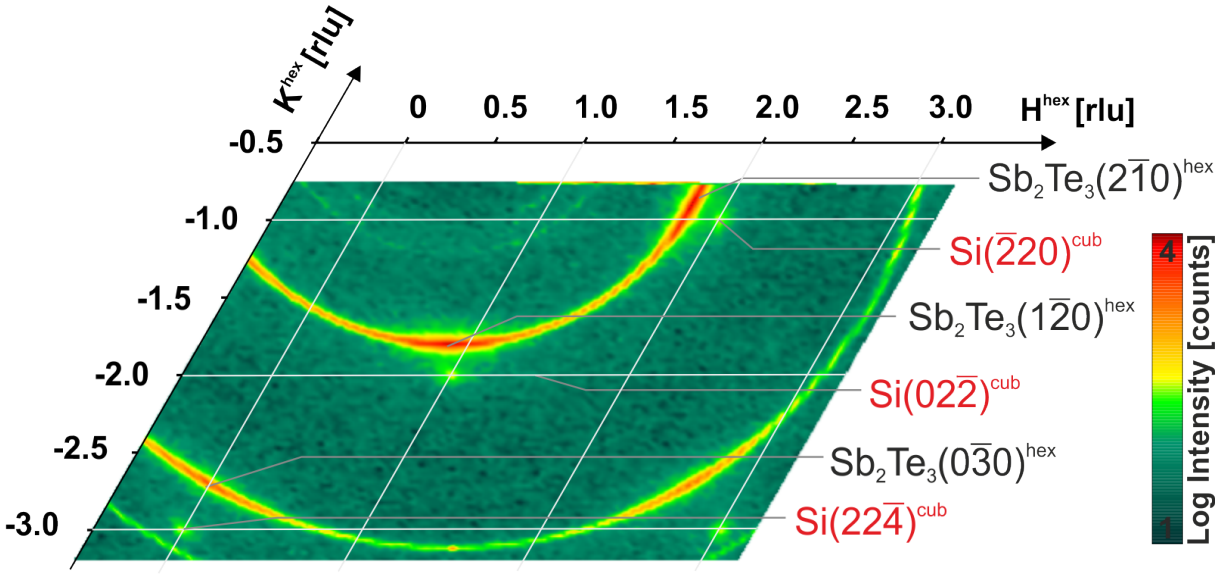

Figure 5.10: In-plane $H\overline{K}$ RSM at L=0. Strong in-plane mosaicity is observed

film with respect to the substrate, a strong in-plane mosaicity is observed in the reciprocal map. The first and second intense rings are at a d-spacing of ∼2.13 Å, ∼1.23 Å corresponding to the scattering vectors of $q_{2\bar{1}0}$ and q_{300} respectively. However, there is a weak outer ring at larger scattering vector, which is at a d-spacing of ∼1.069 Å and corresponds to $q_{2\bar{4}0}$. For an azimuthal rotation of every 60° strong intense peaks are observed indicating a six fold symmetry of the epilayer.

5.4 Conclusion

Epitaxial layers of Sb_2Te_3 were grown on largely mismatched Si(111) substrates with an Sb:Te flux ratio of 2:5. Unlike GeTe, Sb_2Te_3 does not show any incubation stage during nucleation in

RHEED and directly display the abrupt changes from Si(111) to Sb_2Te_3 diffraction pattern with clear streaks indicative of a smooth surface morphology. This was further confirmed by XRR investigation of the epilayer indicating surface roughness as low as 2 nm. The density of the epilayer is found to be close to the bulk value. AFM measurements show a decrease in surface roughness of the epilayer with increase in T_{sub}, probably due to better atomic mobility on the surface at higher substrate temperatures.

XRD measurements show that the epilayer is exclusively [00.1] oriented, aligning its high symmetry in-plane directions with the ones of the Si(111) substrate i.e., Sb_2Te_3<11.0> || Si<$\bar{1}$01> and Sb_2Te_3<10.0> || Si<$\bar{2}$11>. Laue oscillations observed close to the epilayer reflection suggest high crystalline quality of the film. Scan along the (10.L) CTR show the presence of twins. Azimuthal scans and in-plane RSMs indicate a strong twist. The in-plane diffraction peaks demonstrate the presence of roational domains at three different angles (6.5°, 16° and 30°) from the main reflection. The roational domains are expected due to the large lattice misfit of the epilayer with respect to the substrate. Results obtained on the growth of Sb_2Te_3 on Si(111) may prove to be useful in the design and fabrication of high quality GeTe/Sb_2Te_3 superlattices.

6 Epitaxial Growth of GST

Non-volatile memories based on GeTe-Sb_2Te_3 (GST) alloys lying along the technologically relevant pseudobinary line are considered to be the most promising candidate for the replacement of conventional charge based storage technologies[71,144–148]. A novel concept for a low power consumption phase change memory is based on alloys with a controlled stacking sequence that exhibit lower switching energies, enhanced cyclability, lower atomic migration, better stability and thinner cells than their monolithic polycrystalline counterparts[15,149,150]. The faster switching mechanism of these alloys requires a detailed understanding of the structural changes during phase transitions. However thin films of GST used for switching studies are prepared by sputtering, which results in polycrystalline textured layers. Orientational disorder in polycrystalline films complicate the interpretation of the results. MBE offers the possibility to fabricate thin films with high structural quality.

6.1 Growth of GST

GST thin films were grown using Ge, Sb and Te dual filament effusion cells. The cell temperature of the sources were set such that the flux ratio of Ge:Sb:Te is around 2:2:5. Typical growth rate of GST at room temperature is about ∼0.9 nm/min. The growth is initiated by opening all the three shutters (Ge, Sb, Te) simultaneously. Depending on the substrate and its orientation, the growth proceeds with either a smooth surface morphology or island growth. Figure 6.1 shows the different growth regimes of GST on Si(111), GaSb(111) and GaSb(001). The growth rate of the films were determined from thickness of the film by XRR and side-view SEM. At low enough temperatures (<100 °C) the film grows amorphous as evidenced by the *in-situ* RHEED showing a diffuse background (figure 6.1 (a)). At slightly higher temperatures, the adatoms are not mobile enough on the surface so that the layer does not align along preferred orientations resulting in a polycrystalline film with random orientations and the RHEED shows diffraction rings (figure 6.1 (b)). Depending on the substrate and its orientation, the epitaxial growth (as determined by the streaky (see figure 6.1 (c)) or 3D crystalline RHEED pattern) of GST starts between 150-180 °C and extends till 240-260 °C. At higher temperatures (>250 °C) hardly any growth is observed.

Figure 6.2 shows the RHEED pattern observed on various lattice matched and highly mismatched substrates and on different orientation. Each row corresponds to the growth on substrate mentioned in the top left corner of the RHEED image in the left column. The column on the left corresponds to the initial surfaces of the substrate, the center column shows the intermediate stage after initiating the growth, while the right column displays the final GST surface. The bulk lattice mismatch of GST with respect to GaSb, InAs and Si are 1.38, 0.77 and 10.70 % respectively. Due to the lower lattice mismatch, epitaxy of high quality single

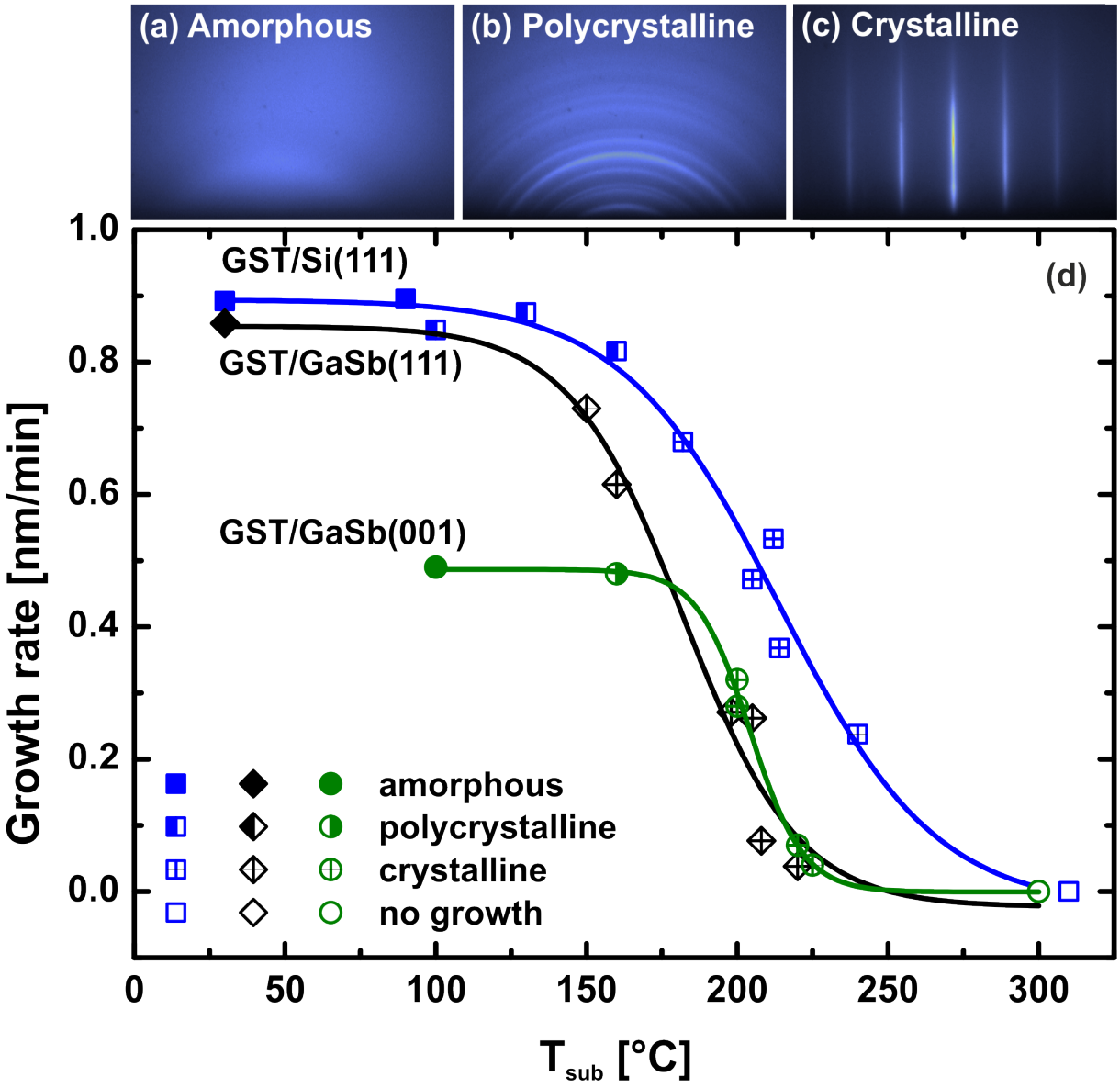

Figure 6.1: RHEED pattern of (a) amorphous, (b) polycrystalline and (c) crystalline surfaces; (d) growth rate versus T_{sub} for GST grown on different substrates and orientation. Different growth regimes: amorphous, polycrystalline, epitaxial and no growth are observed

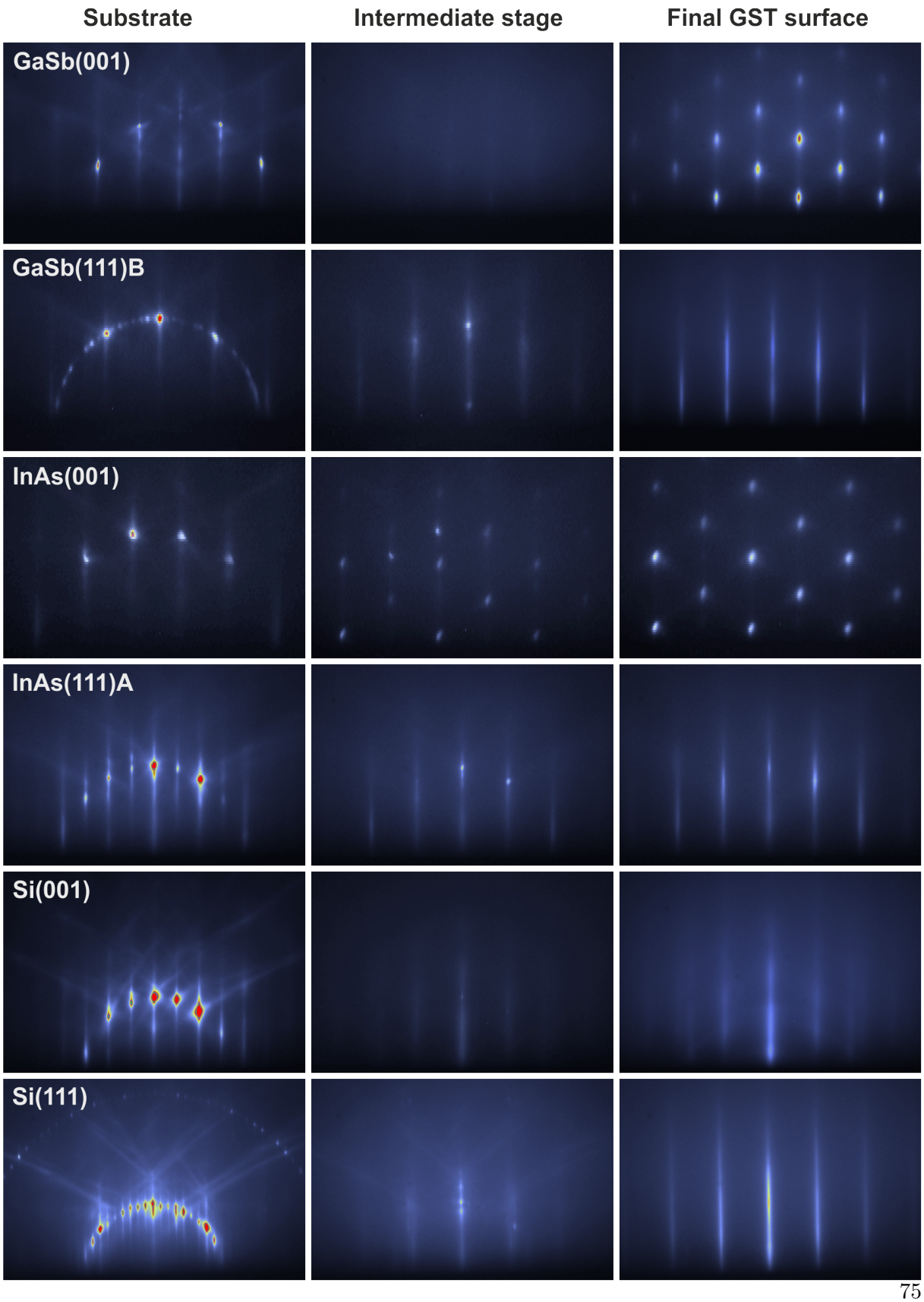

Figure 6.2: Surface morphology as observed by RHEED for the growth of GST on different substrates along $<1\bar{1}0>$ azimuth. Left column represents the initial surface, center column the intermediate stage after initiating the growth and right column shows the final GST surface

crystalline film is most favourable in the case of GaSb and InAs. Previous work[113,114] shows that epitaxial growth of GST on GaSb(001) substrate displays an incubated epitaxy during the initial stages of growth, where an amorphous-to-crystalline transition is observed. However after the incubation stage, the film shows a transmission 3D RHEED pattern indicative of rough surface morphology. Careful analysis by GIXRD scan indicates a four fold and six fold

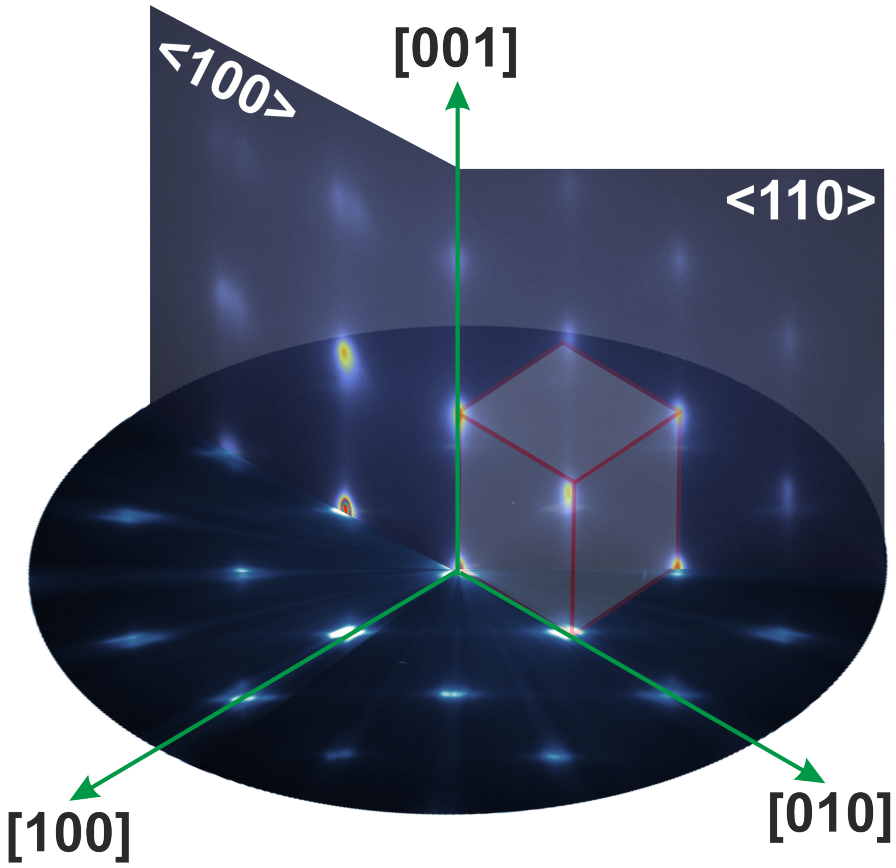

Figure 6.3: Reciprocal lattice of a GST film grown on InAs(001) constructed from RHEED scans along different azimuths.

symmetry implying two epitaxial orientations, with either the [001] or the [111] axis of the film parallel to [001] direction[114]. Shayduk et al.,[116] reported that the in-plane mosaicity caused by rhombohedral distortion along the [111] direction causes broadening of in-plane reflections and hence by strategically aligning the distortion perpendicular to the substrate surface, high quality epitaxial layer can be grown. The preferential growth along the [111] direction is obtained using a suitable substrate orientation. Shayduk et al., showed that the growth on GaSb(111) oriented substrates is more promising and the film exhibits a streaky RHEED pattern indicative of a smooth crystalline surface morphology as can be seen in the figure 6.2[113].

GST growth on slightly lower mismatch substrate than GaSb, namely InAs shows the same

behaviour on different substrate orientations i.e., growth on InAs(001) show a 3D RHEED pattern indicative of island growth, while the film grows as a smooth epitaxial layer on InAs(111) substrates. However, no incubated epitaxy of GST is observed when grown on InAs(001) substrate as seen in figure 6.2 (correspondent to InAs(001) row). The film starts to grow with the formation of 3D islands right from the beginning of the growth. The crystal structure of the GST alloys grown on InAs(001) becomes apparent upon combining RHEED patterns acquired along different azimuths as shown in figure 6.3. The circular in-plane pattern was constructed from a

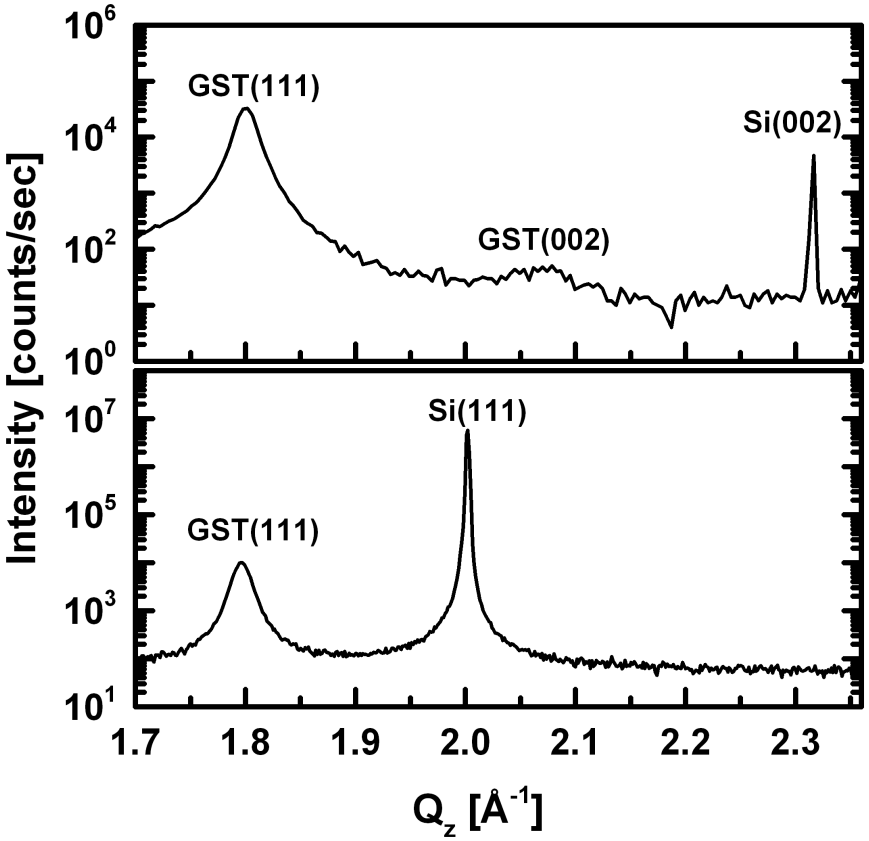

Figure 6.4: Specular $\omega - 2\theta$ XRD scans show that GST grows along [111] direction on both Si(001) and Si(111) substrates. However a weak polycrystalline orientation along [001] is also observed on Si(001)

set of RHEED scans obtained during the continuous rotation of the substrate [151]. The quasi-3D rendering reveals the body-centred cubic reciprocal lattice of the GST alloy, in agreement with the real space face-centred rocksalt like structure expected for the metastable cubic phase. Intensity streaks along the face or body diagonal directions of the unit cell indicate disorder and

prelude to the eventual formation of facets along these directions. The epitaxial relations for the growth of GST on InAs are GST[001]||InAs[001] and GST[111]||InAs[111]. From the above four growth examples, it is possible to conclude that the growth behaviour is influenced by the substrate orientation rather than the substrate material.

A peculiar phenomenon is observed for the growth of GST on highly lattice mismatched substrate such as Si (∼10.7 %). In contrast to the growth of GST on GaSb(001) and InAs(001) substrates, epitaxy on Si(001) exhibits a streaky RHEED pattern indicative of a smooth surface morphology 6.2. There is no amorphous-to-crystalline transition at the beginning of growth. However, the growth of GST on Si(111) is similar to the other (111) oriented substrates i.e., it exhibits a streaky RHEED pattern. It is interesting to note that, on highly mismatched substrates, the film grows as a smooth epitaxial layer irrespective of the substrate orientation, whereas on closely lattice matched (001) substrates, a 3D surface morphology is observed. A detailed understanding is necessary to explain this unexpected phenomenon.

Specular $\omega - 2\theta$ XRD scans plotted in figure 6.4 show that there are two out-of-plane orientations namely [001] and [111] for the GST growth on Si(001), however the intensity of the (002) peak is very weak implying that the predominant out-of-plane orientation is along the [111] direction i.e., GST[111]||Si[001] with a weak contribution of GST[001]||Si[001]. Contrary to the case of GaSb and InAs[117], the growth behaviour in this case is mainly influenced by the substrate material and its mismatch, rather than the substrate orientation. The epitaxy of GST on Si(001) is better in terms of surface morphology in comparison to the growth on GaSb(001) and InAs(001) substrates as seen from the RHEED pattern (see figure 6.2). Unlike the case of growth on GaSb and InAs substrates, where the substrate affect the reliable determination of composition due to the comparable atomic weights of the deposited material, Si does not pose such a problem due to its lower atomic weight than any of the three used GST alloy components namely Ge, Sb and Te. Due to the technological relevance of Si, further growth experiments were performed on Si(111) substrates.

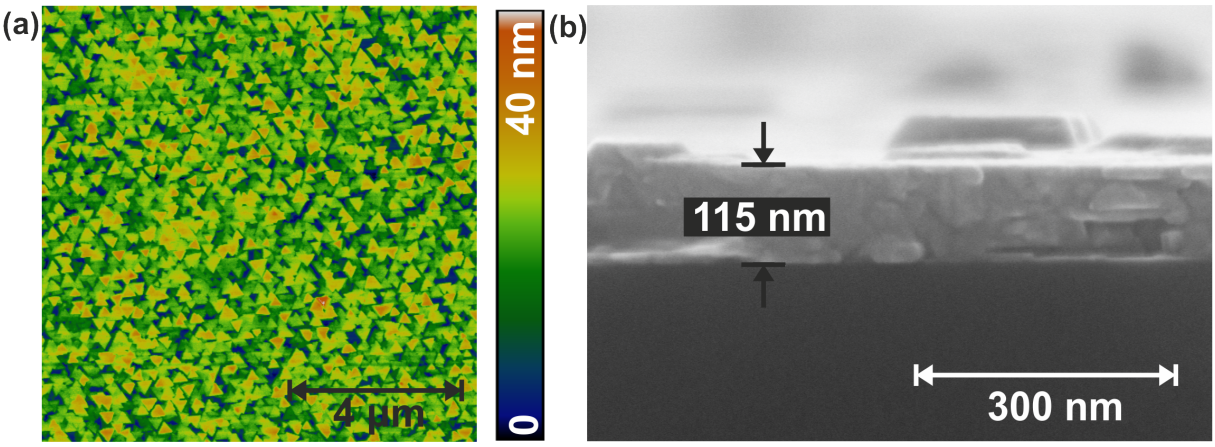

Figure 6.5: Surface morphology of GST grown on Si(111) as observed by AFM (a) having a root mean square roughness of ∼5.85 nm and cross sectional SEM (b)

Streaky RHEED pattern indicates a smooth surface morphology, however large atomically

flat islands will also produce a streaky RHEED pattern as already pointed out for the case of GeTe grown on Si(111). Hence to investigate the actual surface morphology, AFM and SEM measurements were done on the sample. Figure 6.5 (a) shows the AFM of GST grown on Si(111). Large flat traingular islands (crystallite size of 150-200 nm) with a rms surface roughness of about ∼5.85 nm are observed. Two orientations of the triangular features rotated by 180° around surface normal with respect to each other are observed on the surface. This indicates the presence of twinning and will be discussed later in section 6.5.1. The cross sectional SEM (figure 6.5 (b)) shows that the layer is closed and of 115 nm thickness; the triangular islands are flat and protrude above the closed GST layer.

6.2 Growth Issues Related to Temperature Control

The substrates are heated radiatively by a resistive wire heater and the substrate temperature is measured by a non-contact thermocouple placed few millimetres behind the substrate. Hence, the thermocouple does not sense the real substrate temperature. The thermocouple measures the heat arising from the resistive substrate heater, substrate, substrate holder and the source cell temperatures, resulting in poor coupling of the thermocouple with the substrate. Further complications arise if the deposited films have larger absorption bands in spectral regions where the substrate is transparent. In this case, the film surface gets heated up faster than the substrate and the thermocouple fails to sense the increase in surface temperature. This leads to serious problems if the deposited material has a narrow epitaxial growth window and its composition is highly dependent on the growth temperature. In our compact MBE systems designed by Createc for performing *in-vivo* GIXRD studies, temperature inaccuracies of about ±30 °C at typical growth temperatures of around 200 °C are reported[116,152].

A set of three GST epitaxial films, grown under equal nominal substrate temperature conditions (220 °C as given by the thermocouple reading) and fluxes, showed significantly different compositions, namely: $Ge_{25}Sb_{19}Te_{56}$, $Ge_{27}Sb_{17}Te_{56}$, $Ge_{33}Sb_{12}Te_{55}$. Even under identical growth conditions the Ge and Sb concentration is highly inconsistent from sample to sample. The above samples were monitored by QMS during growth. Though all the atomic/molecular species are monitored simultaneously during growth, for our analysis we consider GeTe as it is the only heteromolecule observed and is also stable as seen from the QMS. Monitoring the GeTe signal gives an insight into the fluctuations of both Ge and Te signals simultaneously. Analysis of the desorption signals acquired during growth displayed a completely different GeTe desorption: 27, 30 and 39 % of the maximum desorption for the above three samples, respectively. Interestingly the composition fluctuation is not random, but strongly dependent on desorption which in turn is a function of substrate/surface temperature. With increase in GeTe desorption the Ge (Sb) composition increases (decreases), while the Te composition remains almost constant and independent of the growth temperatures. The switching speed of GST alloys is strongly dependent on the composition of the alloy and increases with increase in Sb content[153]. For device applications it is useful to provide uniform switching speed and hence homogeneous composition. Therefore, it is necessary to accurately control the growth temperatures, which in turn relates to the composition.

6.2.1 Determination of Growth Temperature from QMS Desorption

Since the thermocouple temperature is unreliable for growth studies, we use the GeTe desorption signal as observed by the QMS for calibration from growth run to growth run. Figure 6.6 shows the growth rate (in green) obtained from a set of samples grown at different substrate temperatures (measured by thermocouple). Blue curve corresponds to the GeTe desorption versus T_{sub}. The desorption curve is obtained by ramping down the substrate at 0.1 °C/min from maximum desorption to minimum desorption. Regions of very low desorption usually

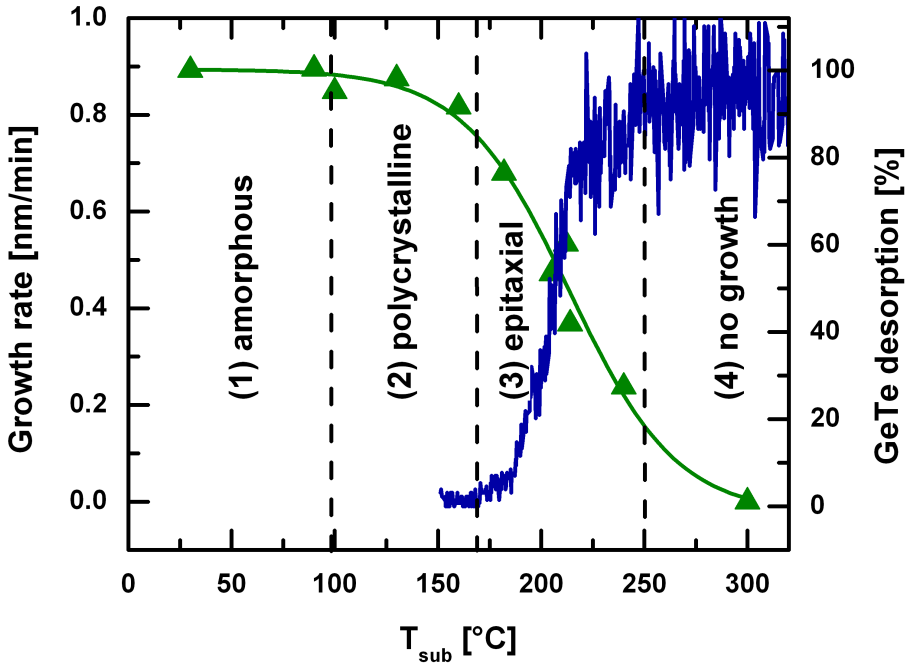

Figure 6.6: Growth rate (green)/GeTe desorption (blue) versus thermocouple temperature for GeTe growth on Si(111). The four growth regimes are marked as follows: (1) amorphous, (2) polycrystalline, (3) epitaxial and (4) no growth

exhibit polycrystalline pattern from RHEED, while the growth rate is very low for regions of almost maximum desorption. The growth window lying between the polycrystalline and no growth regime, is suitable for the growth of epitaxial films. As a thumb of rule, 20% desorption is set to achieve high growth rate as well as good epitaxial film. Experimentally it is found that the desorption curve shifts up to ±30 °C from sample to sample and hence, it is necessary to find the temperature corresponding to the required desorption point for each growth run. This is accomplished using the same procedure used to obtain the desorption curve of figure 6.6, and described in more details in the next section.

6.2.2 Growth at Constant Thermocouple Temperature

Figure 6.7 shows the typical line-of-sight QMS signal observed for GeTe during GST growth on Si(111) substrate and the recorded thermocouple temperature. The origin of the time axis corresponds to the simultaneous opening of all the shutters at T_{sub} = 300 °C, which is high enough to ensure no sticking of the impinging species and thus maximum desorption Φ_{max} (see figure 6.7). The substrate temperature is ramped down at $0.1°C$/sec to enable the sticking of the atoms/molecules onto the substrate, which can be observed by the corresponding decrease in GeTe desorption. The temperature at which the desorption starts to decrease is labelled by $T_{\Phi_{max}}$. The substrate temperature is further decreased till almost zero desorption is measured and subsequently increased to obtain a 20% desorption signal. The growth is then sustained at constant thermocouple temperature.

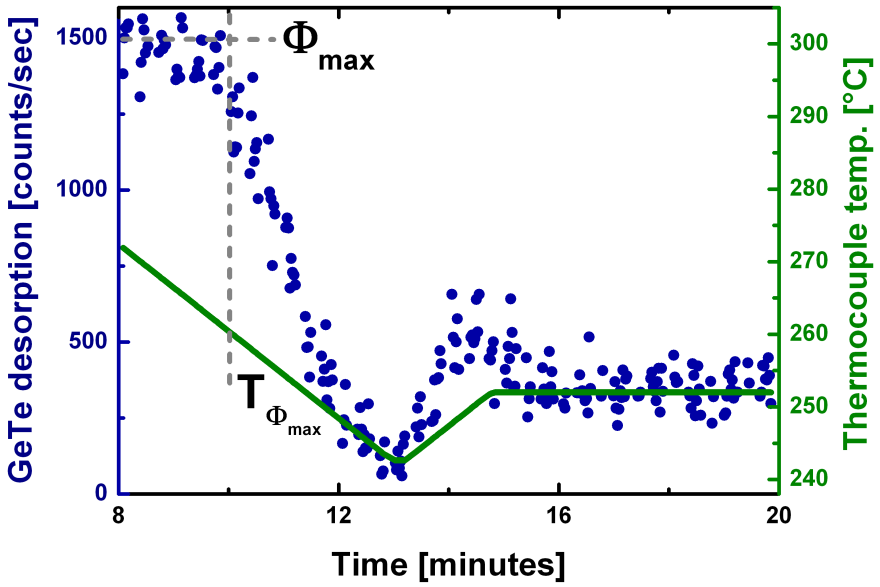

Figure 6.7: GeTe desorption (blue) and thermocouple temperature (green) as a function of time during the initial stages of the growth procedure. Φ_{max} is the maximum desorption and $T_{\Phi_{max}}$ is the temperature at which the desorption starts to decrease

However, if growth is performed at constant thermocouple temperature, an increase in desorption as shown in figure 6.8 is observed. The blue curve shows the desorption and the green line represents the thermocouple temperature versus time. The thermocouple temperature is highly stable, whereas the desorption increases from 20% to almost 60%. A 40% change in desorption reflects a considerable composition gradient.

The change in desorption can be attributed to the change in surface temperature. The failure of the thermocouple to monitor the increase in surface temperature is ascribed to the bad cou-

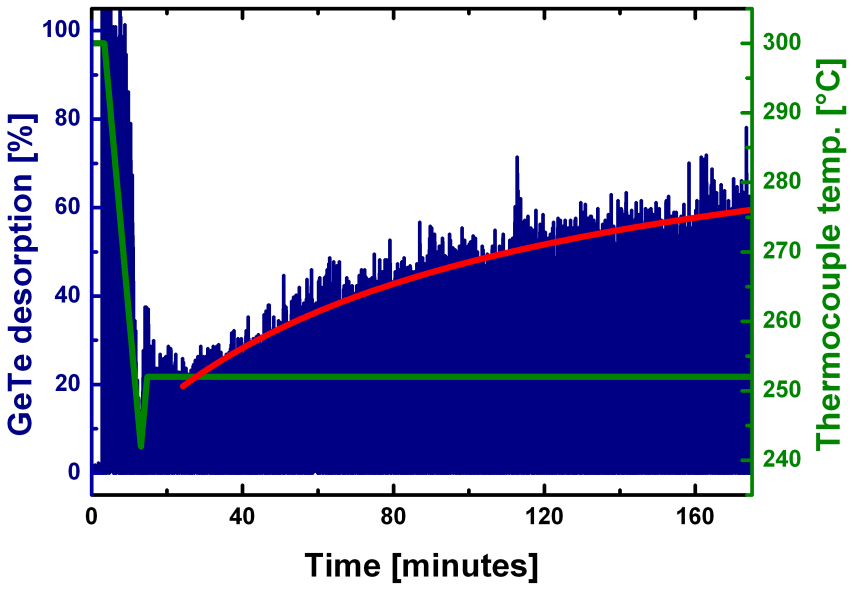

Figure 6.8: GeTe desorption (blue) and thermocouple temperature (green) as a function of time. Red curve is the fit of the increase in desorption during growth

pling (non-contact mode) with the substrate[154–156]. At typical growth temperatures of GST (200 -250 °C) common pyrometry cannot be used, as stray light from the mass spectrometer filament and ionisation gauge might hamper the accurate measurement of the substrate temperatures.

In our experiment, a rough estimate of 20-30 °C temperature increase can be deduced from the desorption versus temperature curve of the first 14 minutes deposition shown in figure 6.7. The change in surface temperature during the growth can be either of the following two reasons. (1) Crystalline GST has a smaller band gap (0.5-0.61 eV)[53] compared to Si which has a band gap of 1.1 eV. That means GST epitaxial films exhibit large absorption bands in the infra-red wavelength region where Si is transparent (>1.1 μm). So, the additional infra-red radiation with energy lying between the band gaps of the film and substrate will be absorbed by the film resulting in an increase in surface temperature. (2) Upon deposition, the emissivity of the surface changes due to various reasons such as different material system than the substrate, change in surface morphology upon growth and increase in film thickness. Shanabrook et al.,[155] based on MBE growth studies of narrow band gap materials (GaSb, InAs) on wider band gap material (GaAs) found that the band gap mismatch plays the dominant role in the increase of surface temperature, while emissivity changes upon deposition contribute very less. The situation is similar to our case, where GST has a smaller band gap than Si.

6.2.3 Growth at Constant Desorption

Increase in desorption accompanied by increase in surface temperature is expected to cause composition gradient in the film. To achieve homogeneous film composition along the growth direction, it is necessary to control the surface temperature and hence desorption. The increase in desorption is fitted (red curve in figure 6.8) using a function,

$$\Phi = \frac{\Phi_{max} t}{K_m + t}$$

where Φ is the desorption flux, t is time and K_m is the time at half the maximum desorption. From the initial part of the growth curve i.e., during the temperature ramp down, the temperature for the corresponding desorption can be extrapolated and the change in temperature as a function of time can be plotted. In order to keep the desorption and hence surface temperature constant, the thermocouple temperature should be ramped down with a function inverse to the change in desorption. This temperature ramp is controlled using the Emeralt programming software by Createc.

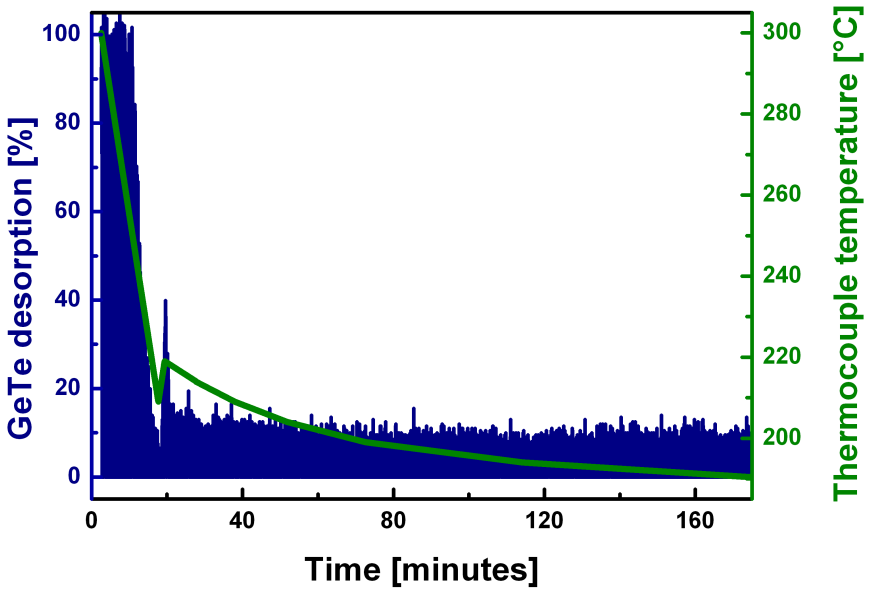

Figure 6.9: GeTe desorption (blue) and thermocouple temperature (green) as a function of time for growth at constant desorption

Figure 6.9 shows the growth at constant desorption by strategically decreasing the substrate temperature (as sensed by the thermocouple) to compensate for the increase in desorption. As the desorption is constant, the sticking of the Ge, Sb, Te atoms is expected to be constant throughout the growth duration and hence homogeneous composition along the film thickness

is achieved. Samples presented after this section are grown using this procedure (constant desorption during growth).

6.3 Compositional Analysis of GST Grown with Different Parameters

As discussed previously, within the narrow epitaxial growth window, the composition of the epilayer is strongly dependent on desorption, which in turn is direclty related to the surface temperature. In order to achieve control over GST composition, it is necessary to study in detail its change with desorption.

6.3.1 Growth at 2:2:5 Flux Ratio

A set of samples grown using 2:2:5 flux ratio were deposited at different desorption regimes. Simultaneously a line-of-sight QMS was used to monitor all the desorbing species. Figure 6.10

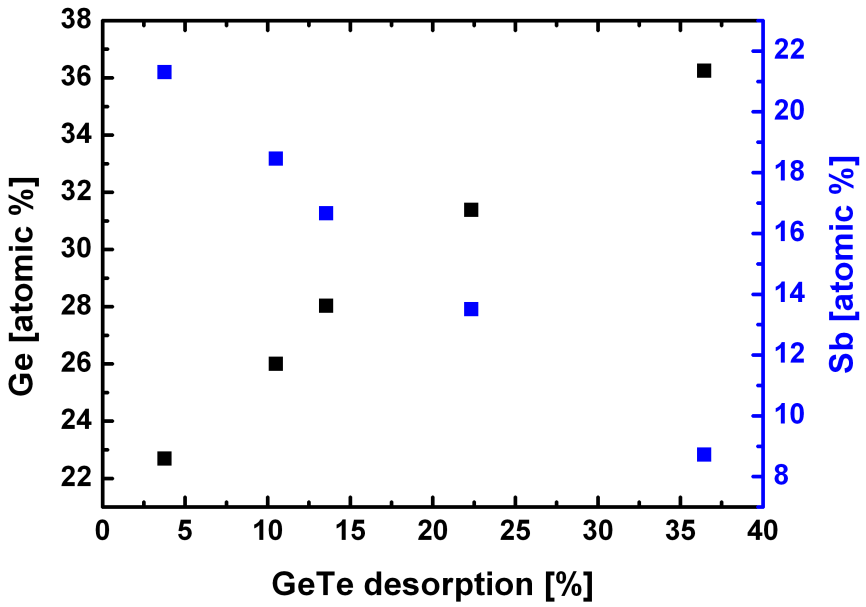

Figure 6.10: GeTe desorption percentage as a function of change in Ge (black) and Sb (blue) composition

shows the change in Ge and Sb composition (mesasured *via* XRF) with respect to desorption. With increase in desorption, Sb concentration decreases while Ge increases and Te remains almost constant. The change in composition with respect to desorption can be calibrated for this flux and it is possible to roughly estimate the composition of the GST film by measuring the percentage of desorption during growth.

GST exhibits a metastable NaCl type of crystal structure with Te atoms occupying one sublattice and Ge/Sb/vacancies occupying the other one[39,40]. Thus, from the compositional analysis, one can infer that the Te sublattice is completely filled independently of the surface temperature used for growth. However, a strong competition between the Ge and Sb atoms in occupying the other sublattice is revealed.

Figure 6.11 shows the composition of the samples in the GST ternary diagram. The red dashed line indicates the GeTe-Sb_2Te_3 pseudobinary line, while the violet dashed line shows the trend of composition variation with increase in desorption. The end point on the ternary diagram corresponds to the composition of the epitaxially grown GeTe found to be about $Ge_{0.46}Te_{0.54}$ (see 4.5). Interestingly the composition of the samples grown at different desorption regimes

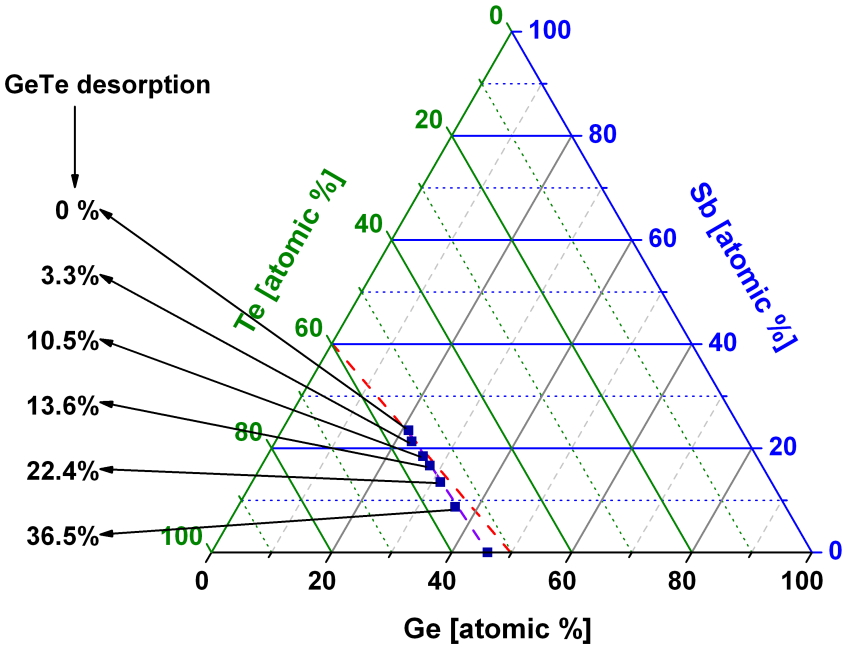

Figure 6.11: Composition of samples in the Ge-Sb-Te ternary diagram for samples grown using 2:2:5 flux. Red dashed line indicates the GeTe-Sb_2Te_3 pseudobinary line

vary almost along the pseudobinary line. In fact a slight offset is visible and the composition of the films varies along a straight line towards the more stable GeTe composition i.e., $Ge_{0.46}Te_{0.54}$.

Figure 6.12 (a) shows the specular $\omega - 2\theta$ XRD scan of the GST samples shown in figure 6.11. A clear trend in the shift of the GST peak is observed. With increase in Ge concentration, the peak positions move towards low Q_z values, indicating an increase in the out-of-plane lattice spacing. Figure 6.12 (b) shows the out-of-plane lattice constant with respect to Sb (blue) and Ge (black) atomic percentage and their corresponding linear fits of the composition versus lattice constant. Contrary to what was reported by Matsunaga et al.,[157] for sputtered films, in the case of epitaxial layers with increase in Ge (Sb) concentration, the out-of-plane lattice constant increases (decreases) linearly. For growths under similar flux conditions and under the

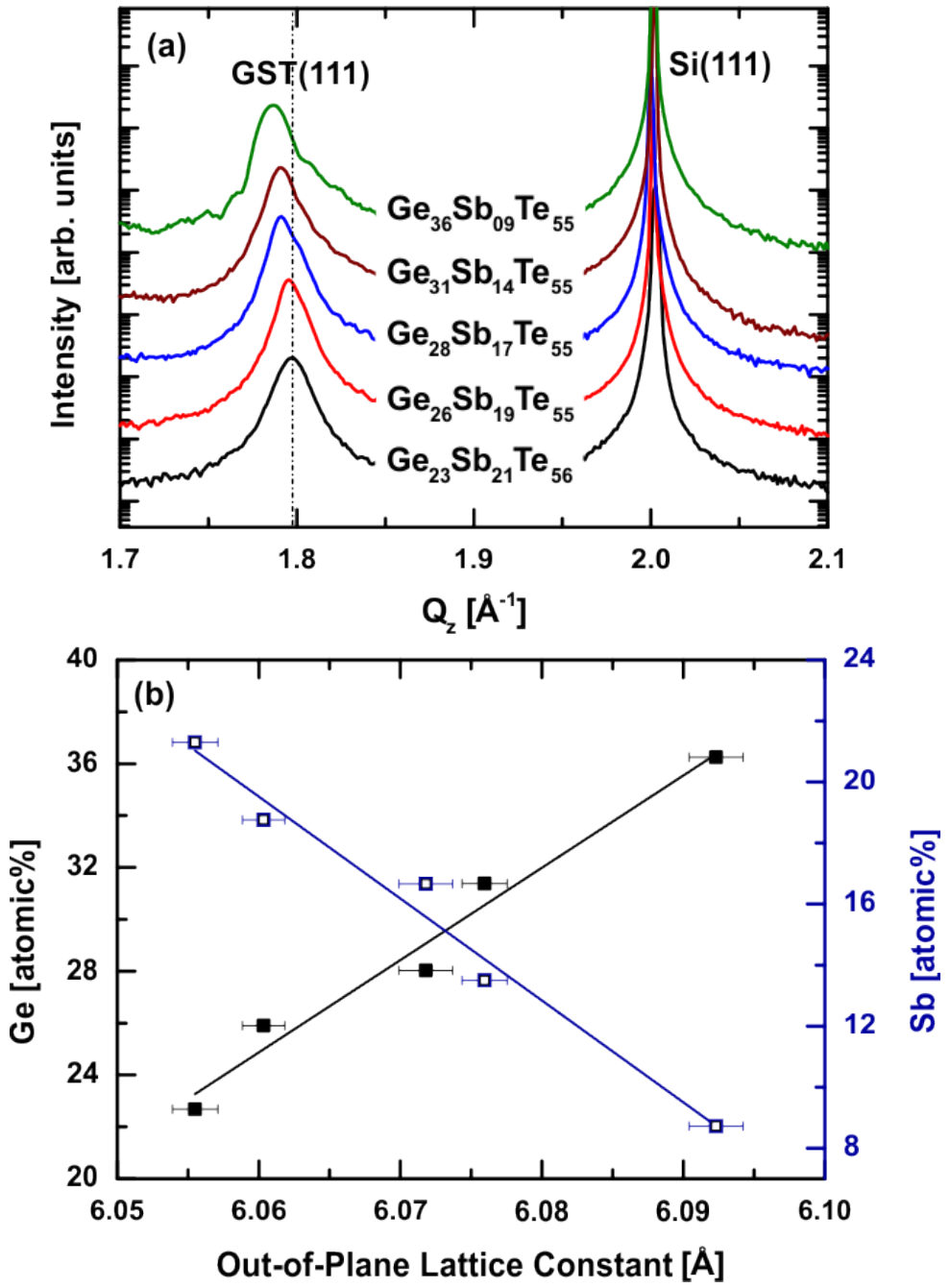

Figure 6.12: (a) Specular $\omega - 2\theta$ XRD scan for samples with different composition. (b) Ge (black) and Sb (blue) atomic % with respect to out-of-plane lattice constant

assumption that the layers are fully relaxed, the GST out-of-plane lattice constant can be used as a measure of the composition.

6.3.2 Growth at 2:3:5 Flux Ratio

In the previous section (6.3.1) it was shown that setting the fluxes to 2:2:5 ratio, the composition of the grown GST almost lies on the GeTe-Sb_2Te_3 pseudobinary line. An interesting issue is to understand what happens, if the initial flux does not give rise to a nominal composition along the pseudobinary line. To this end, one of the source fluxes namely Sb was increased by 1.5 times over the previous value, which gives a flux ratio of 2:3:5. As in the previous case, a series of samples were grown at different desorption regimes, including an amorphous sample for calibration purpose. Figure 6.13 shows the Ge, and Sb composition of samples grown at different GeTe desorption values. Unlike the samples grown at 2:2:5 flux, the sample composition does not seem to vary in a linear fashion with change in desorption, as can be seen in the figure 6.13. To note, even at high desorption regime (30% GeTe desorption), a significant amount of Sb is still present in the film, while in the case of 2:2:5 flux the Sb concentration drops down considerably.

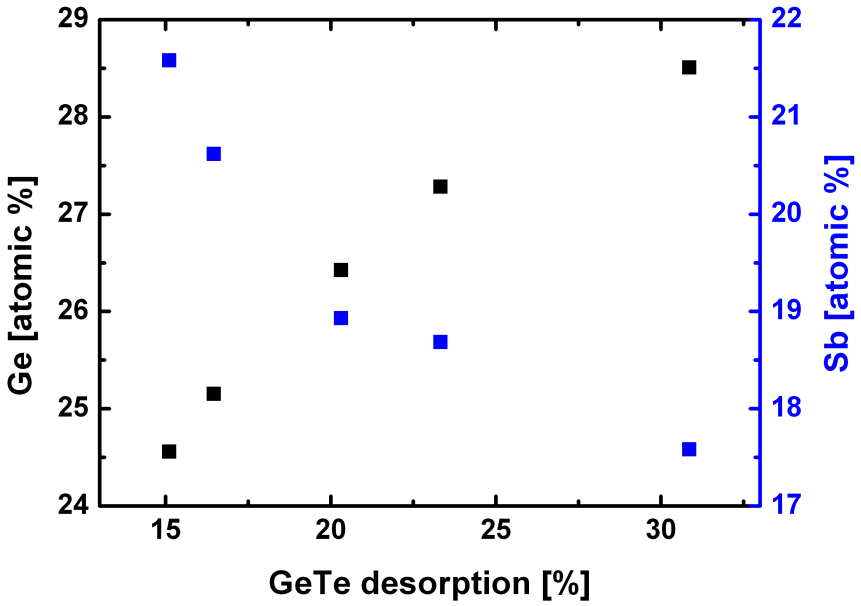

Figure 6.13: GeTe desorption percentage as a function of change in Ge (black) and Sb (blue) composition

Figure 6.14 shows the ternary diagram depicting the concentration of the GST films grown using 2:3:5 flux. The standalone point which corresponds to a concentration of $Ge_{20}Sb_{30}Te_{50}$ is the room temperature amorphous sample. All other points in the ternary diagram refer to the

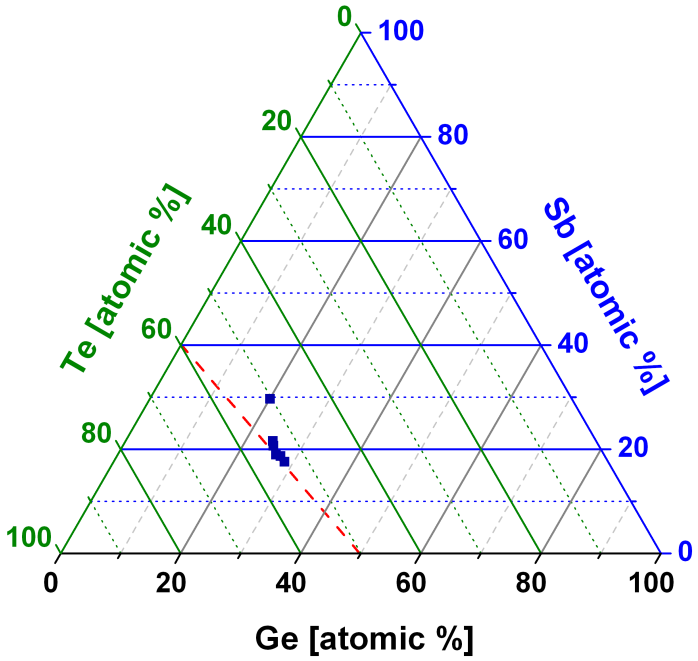

Figure 6.14: Composition of samples in the Ge-Sb-Te ternary diagram for samples grown using 2:3:5 flux. Red dashed line indicates the GeTe-Sb_2Te_3 pseudobinary line

epitaxially grown GST films. As soon as the film starts to grow in the epitaxial window, the composition of the film falls along the pseudobinary line and does not vary much with change in desorption. From this we can conclude that, if a sufficient amount of Sb flux is supplied, even at higher desorptions it can be incorporated in the film. This is suitable to compensate for the large drop in Sb content (as observed in previous case) when grown at higher desorption regimes.

6.3.3 Growth at 3:2:5 Flux Ratio

Ge flux was increased to 1.5 times, such that the supplied flux ratio is 3:2:5. A set of samples at different desorption regimes was grown. The composition of the grown films is shown in the ternary diagram along with the corresponding GeTe desorption (figure 6.15). The amorphous sample is represented by zero GeTe desorption. The composition of the epitaxial films in this case is out of the pseudobinary tie line and a large deviation in the composition with change in desorption is evident. To note, unlike the previous set of samples (grown using 2:2:5 and 3:2:5 fluxes) where Te concentration almost remained constant with change in desorption, in this case Te varies considerably and at higher desorption regimes, there is almost 6-8% deviation from the samples grown at lower desorption regime. This set of experiments prove that, increased Ge flux is not suitable for fabricating GST films with composition along the pseudobinary line.

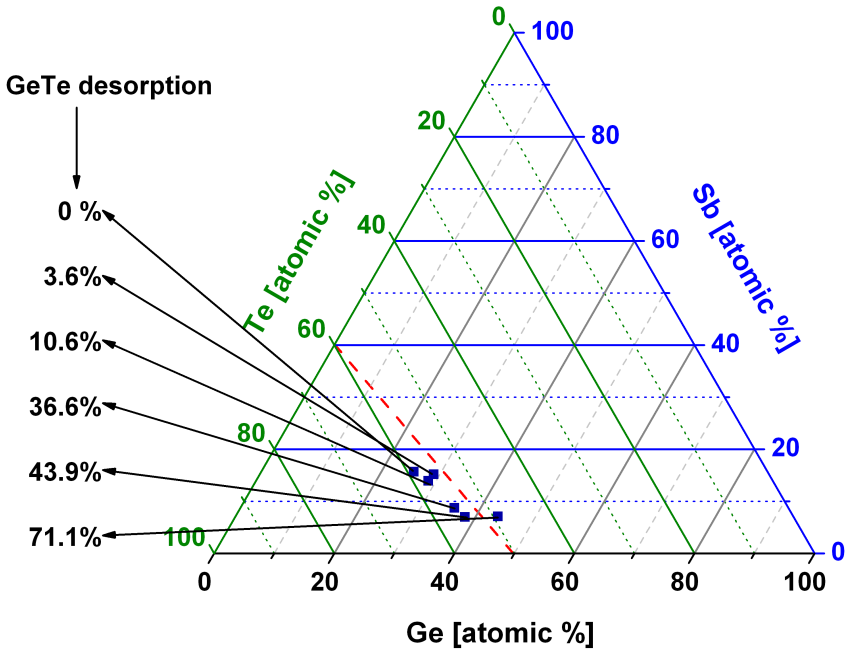

Figure 6.15: Composition of samples in the Ge-Sb-Te ternary diagram for samples grown using 3:2:5 flux. Red dashed line indicates the GeTe-Sb_2Te_3 pseudobinary line

6.3.4 Growth at 3:3:94 Flux Ratio

In this set of experiments the Te flux was increased to a huge amount such that the GST flux ratio is set to 3:3:94 ratio. Te was increased with the assumption that, the excess Te should desorb from the surface as not enough Ge/Sb atoms are available to account for the excess Te flux (as Te occupies one sublattice in a GST crystal and Ge/Sb/vacancies occupy the other).

Figure 6.16 shows the composition of the samples grown at different GeTe desorption. The sample with very high Te content (0% GeTe desorption) corresponds to the amorphous grown sample. Te concentration of the epitaxial samples decrease almost 30% when compared to the room temperature value and it remains almost constant even for different desorption percentages. The composition of these samples do not lie on the pseudobinary line. However, it is interesting to note that only small variation of Ge/Sb content with change in desorption is found. Even for desorption changes greater than 50%, the Ge/Sb concentration varies by less than 3 atomic percent. Though the experiment was performed at very high Te flux, it might give an indication to understand, how the composition varies if the initial Te flux is less than 65 atomic percent (the stable value for Te content presented in this section). In that case it is assumed that, the large deviations in composition with respect to change in desorption can be avoided and samples can still be fabricated close to the GST pseudobinary line.

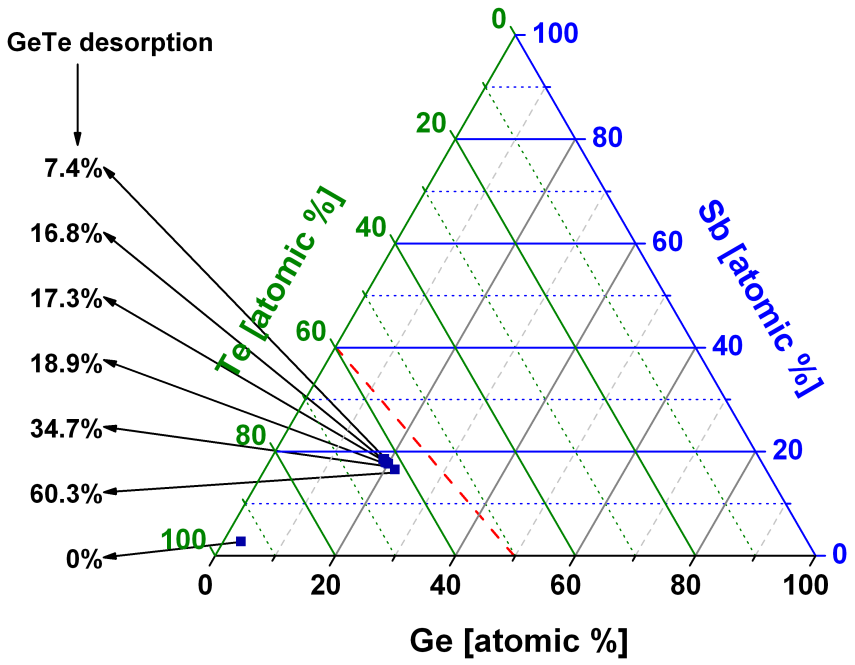

Figure 6.16: Composition of samples in the Ge-Sb-Te ternary diagram for samples grown using 3:3:94 flux. Red dashed line indicates the GeTe-Sb_2Te_3 pseudobinary line

6.4 Incommensurate Peaks and Vacancy Ordering

RHEED during the growth of GST on Si(111) shows streaky diffraction pattern indicative of smooth crystalline growth and specular $\omega - 2\theta$ xrd scans show that the growth occurs along the [111] direction i.e., GST[111]||Si[111]. Figure 6.17 shows the radial scan along [111] direction. The sharp peaks at Q_z = 2.00, 4.00, 6.01 $Å^{-1}$ are the substrate reflections and are marked in red. Apart from the Si reflections, there are 3 narrow peaks and 4 broader peaks attributed to the epilayer at 1.80, 3.60, 5.40 $Å^{-1}$ and 1.52, 3.32, 4.84, 5.12 $Å^{-1}$ respectively. The peaks at 1.80, 3.60 and 5.40 $Å^{-1}$ are multiple order Bragg reflections of the GST epilayer corresponding to (111), (222) and (333) planes respectively. However the broader peaks at 1.52, 3.32, 4.84 and 5.12 $Å^{-1}$ are not Bragg reflections as they are not the resultant of integer order reflections of the first peak. The peaks do not correspond to any other GST reflections. Ge, Sb and Te layers were separately grown on Si(111) as reference to ensure that the peaks are not the resultant of atomic segregation.

The appearance of non-Bragg peaks might indicate that these satellite peaks are incommensurate reflections of the GST epilayer arising from structures with larger lattice parameters. Incommensurability in crystals can be attributed to the presence of orientational, displacive, occupational, compositional or layer thickness modulations[158,159]. Layer thickness modulations can be neglected in our system, as no superlattice layers are grown. Orientational modulation is observed if materials of different structure are grown one above another. This can also be neglected,

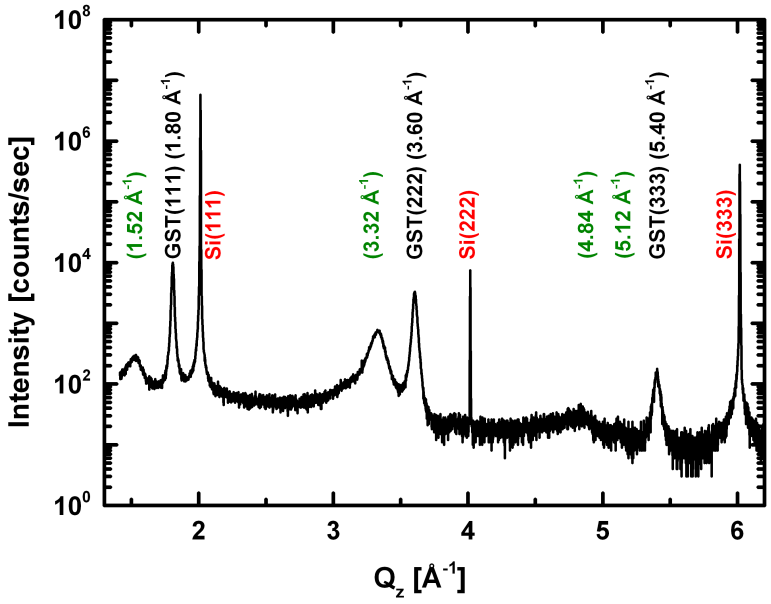

Figure 6.17: Specular $\omega - 2\theta$ XRD scan of GST grown on Si(111)

as the epilayer preferentially grows along the substrate orientation i.e., GST[111]||Si[111].

Compositional modulation can be due to various factors such as substrate rotation during growth in the case of fluxes with non-uniform distributions on the sample surface [160] or source flux modulations during growth. In our case, the growth is performed without rotation on 20×20 mm^2 wafer and within this region, the flux distribution on the sample is fairly uniform and can be neglected. It is more difficult to evaluate the flux stabilities during growth considering that no beam flux monitor is available in the MBE chamber. The usual growth time varies from 30 minutes to 300 minutes depending on the required film thickness. Thinner samples (growth time 30 minutes) also exhibit these satellite peaks and hence flux modulation within the very narrow growth time can be neglected. The last mechanism to consider is the displacive (martensite [161]) or occupational modulation of the individual Ge, Sb atoms or vacancies in the Ge/Sb sublattice.

Incommensurate peaks can be due to long range ordering along the [111] direction and are henceforth called as superstructural peaks (SSP). Their relative position to the GST peaks can be found from the following relation.

$$Q_z = \frac{2\pi}{d} = \frac{2\pi\sqrt{h^2 + k^2 + l^2}}{a}$$

Along the [111] direction, $h = k = l$, so the above equation can be written as

$$l_{ssp} = \frac{aQ_z}{2\pi\sqrt{3}}$$

Where a is the lattice constant of GST found from specular CTR and l_{ssp} is the l value of the SSP along the [111] direction. l_{ssp} corresponding value to the four superstructural peaks are found to be about 0.84, 1.84, 2.69 and 2.84. Interestingly the l_{ssp} values of the SSPs are at a

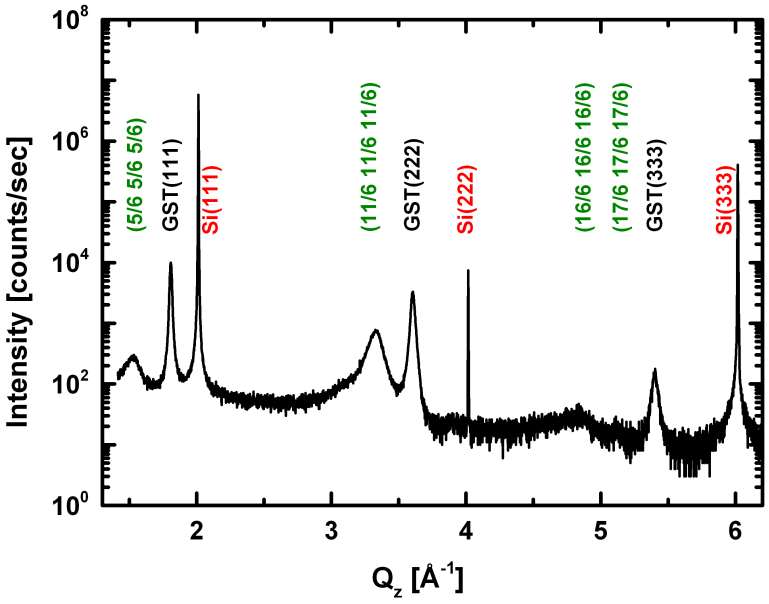

Figure 6.18: Specular $\omega - 2\theta$ scan of GST grown on Si(111). Superstructural reflections (green) along with GST (black) and substrate reflections (red) are labelled

constant difference from the l-value of the GST reflection. l_{ssp} in terms of fast decimals can be approximated into fractionals and the corresponding reflections of the four incommensurate peaks can be assigned in terms of fractional approximation as (5/6, 5/6, 5/6), (11/6, 11/6, 11/6), (16/6, 16/6, 16/6) and (17/6, 17/6, 17/6) respectively. The assigned peak positions are shown in figure 6.18. The fractions imply that the superstructure unit cell along the [111] direction is almost six times the unit cell of GST. This can be ascribed to some kind of structural modulation occuring every 6 unit cells.

Interestingly these SSPs are observed only for growth along the [111] direction and no such peaks are observed for growth along the [001] direction. Extensive x-ray analysis shows that these SSPs are not observed along in-plane directions such as [110] or [11$\bar{2}$]. Figure 6.19 (a) and (b) shows the comparison of specular $\omega - 2\theta$ XRD scans for GST grown on GaSb and InAs and on (001) and (111) orientations, respectively.

GST has a slightly lower lattice constant than GaSb and InAs. Hence the peak positions of GST should appear at slightly larger scattering vectors than the substrate reflections. Substrate and epilayer peaks are clearly resolved on (001) substrates, while they almost overlaps with the substrate peak for the growth on (111) substrates. This is due to the rhombohedral distortion observed in GST along [111] direction[116,162] resulting in slightly larger out-of-plane lattice pa-

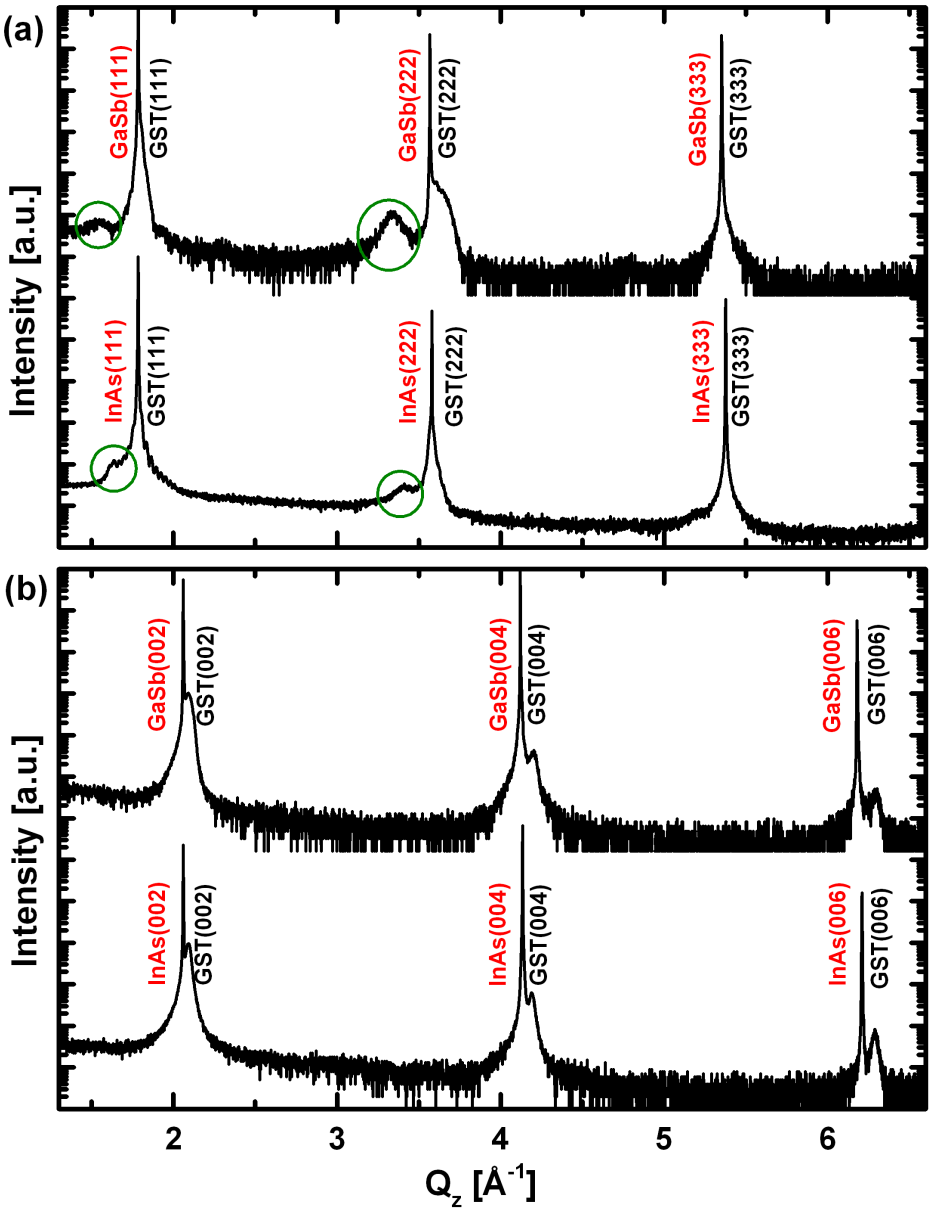

Figure 6.19: Comparison of GST grown on GaSb, InAs and on (001) and (111) orientations. Incommensurate reflections are observed for layers grown along [111] direction

rameter than the in-plane lattice parameter for growth along the [111] direction. Apart from the main layer reflections, there are additional reflections at lower scattering vector for growth along [111] direction, whereas for growth along [001] direction we do not observe any SSPs. These results imply that the superstructual reflections are present only along the [111] direction.

As discussed earlier GST exhibits a metastable NaCl type crystal structure with the 4(a) site fully occupied by Te atoms and the 4(b) site randomly occupied by Ge or Sb atoms along with a certain percentage of vacancies. At high temperatures (258-370 °C) cubic to hexagonal structural phase transition occurs[163–165]. Sun et al., assumed that the atomic arrangement of the cubic and hexagonal GST should be closely related to each other as the cubic to hexagonal transformation is rather quick and only a slight atomic rearrangement might be expected during this transition[49]. Based on this assumption, they used the stable GST structural phase proposed by Petrov (Te-Sb-Te-Ge-Te-Te-Ge-Te-Sb-)[46] and Kooi (Te-Ge-Te-Sb-Te-Te-Sb-Te-Ge-)[47] along with a model in which Ge/Sb can be mixed in the same layer(Te-Sb/Ge-Te-Sb/Ge-Te-Te-Sb/Ge-Te-Sb/Ge-) and performed *ab-initio* calculations based on density functional theory to determine the phase stability of different atomic arrangements. They reported that the structure proposed by Kooi and De Hosson possesses the lowest total energy and hence the most stable stacking. Based on the Petrov and Kooi sequences, Sun et al., rebuilt the cubic structure in terms of hexagonal stacking with (111) planes along the 'c' direction with vacancies placed in between the Te-Te layers and also at Ge/Sb layers. Their results show that metastable cubic GST is highly ordered and the stacking sequence along the [111] direction is similar to the hexagonal structure along the 'c' direction. Thus the metastable state does not have a cubic structure, but is rather a mixture of -Te-Ge-Te-Sb-Te- and -Te-Sb-Te-Ge- units bonded alternatively in space possessing rocksalt symmetry. The results evidence that the vacancies are highly ordered. Work by Zhou et al.[45], confirms their results and explains that the vacancies are in fact geometric voids that lie between the weakly bonded Te-Te layers and the metastable structure along the [111] direction is:

$$-Te-Ge-Te-Sb-Te-v-Te-Sb-Te-Ge-$$

Recent work by Zhang et al.[166], based on density functional theory also shows that metal-insulator transition in GST favours the ordering of vacancies in specific layers. Most of the work mentioned above anticipates the formation of ordered vacancy layers or geometrical void between the Te-Te layers.

Diffraction from vacancy layers should occur from planes perpendicular to [111] direction and not on other directions as shown by our measurements. Because in all other crystallographic planes a mixture of Ge/Sb/Te/v atoms will be expected and hence diffraction measurements will not show the ordering along other directions. Thus we conclude that the SSPs might result from vacancy ordering along the [111] direction. The SSPs have a larger full width at half maximum compared to the basic GST peaks indicating that the diffracting planes for these superstructural reflections might possess an incomplete vacancy layer.

6.4.1 Superstructures in Samples Grown using 2:2:5 Flux Ratio

XRD scans along the specular CTR were performed for the series of samples grown using 2:2:5 flux. The intensity of the SSP close to GST(333) reflection is very weak and in some cases it is almost close to the background signal. Fitting of the SSP close to the GST(333) reflection is difficult in most of the cases. Hence, in the table 6.1 only the peaks observed for scattering vectors less than 4 $Å^{-1}$ are shown. SSP1 and SSP2 given in the table correspond to the superstructural reflections 1 and 2 close to the GST(111) and (222) reflections respectively and l_{SS1} , l_{SS2} are the l values of the SSPs found from the scattering vector Q_z and observed GST lattice parameter a.

Composition	**SSP1** [$Å^{-1}$]	**GST(111)** [$Å^{-1}$]	**SSP2** [$Å^{-1}$]	**GST(222)** [$Å^{-1}$]	l_{SSP1}	l_{SSP2}
$Ge_{23}Sb_{21}Te_{56}$	1.521	1.796	3.315	3.593	0.846 (5/6)	1.844 (11/6)
$Ge_{26}Sb_{19}Te_{55}$	1.550	1.795	3.345	3.591	0.863 (6/7)	1.863 (13/7)
$Ge_{28}Sb_{17}Te_{55}$	1.564	1.791	3.361	3.585	0.872 (7/8)	1.875 (15/8)
$Ge_{31}Sb_{14}Te_{55}$	1.604	1.791	3.403	3.581	0.895 (9/10)	1.900 (19/10)
$Ge_{36}Sb_{09}Te_{55}$	1.684	1.786	3.460	3.571	0.943 (15/16)	1.937 (31/16)

Table 6.1: Superstructural peak positions for samples grown using 2:2:5 flux

Table 6.1 shows that as the concentration of Ge (Sb) increases (decreases), the peak shifts to lower scattering vector or higher out-of-plane lattice constant. However, it is the inverse in case of the SSPs as it move towards higher scattering vector. The GST and SSP move closer and closer towards each other as the Ge concentration increases. This implies that both the size of the superstructural unit cell as well as the basic GST unit cell along [111] direction increases with increase in Ge concentration.

Specular $\omega - 2\theta$ XRD pattern of four of the samples grown using 2:2:5 flux are shown in figure 6.20. The substrate reflections are indexed in red, while the GST reflections are indexed in black. The l_{SSP} values found from the peak positions were converted into fractional approximations and are indexed in green. We could observed that GST and SSPs move toward each other with increase in Ge concentration. The observed superstructural ordering increases from 6 GST unit cells for $Ge_{23}Sb_{21}Te_{56}$ to about 16 GST unit cells for $Ge_{36}Sb_{09}Te_{55}$.

6.4.2 Superstructures in Samples Grown using 2:3:5 Flux Ratio

We had previously discussed in section 6.3.2 that at higher Sb flux, the compositional changes are minimal with respect to growth temperatures. Superstructural peak positions for those samples are evaluated from specular CTR scan along the [111] rod and given in table 6.2.

The GST peak positions do not vary much as the compositional variation of the GST epitaxial layers are minimal with change in growth temperatures. The SSPs follow the same pattern and though the peak position shifts to larger scattering vector with increase in Ge content, the shift is minimal compared to the samples grown under 2:2:5 flux.

The l values of the SSPs increase steadily with increase in Ge content and are converted to fractional approximations in order to find the size of the superstructural unit cell with respect

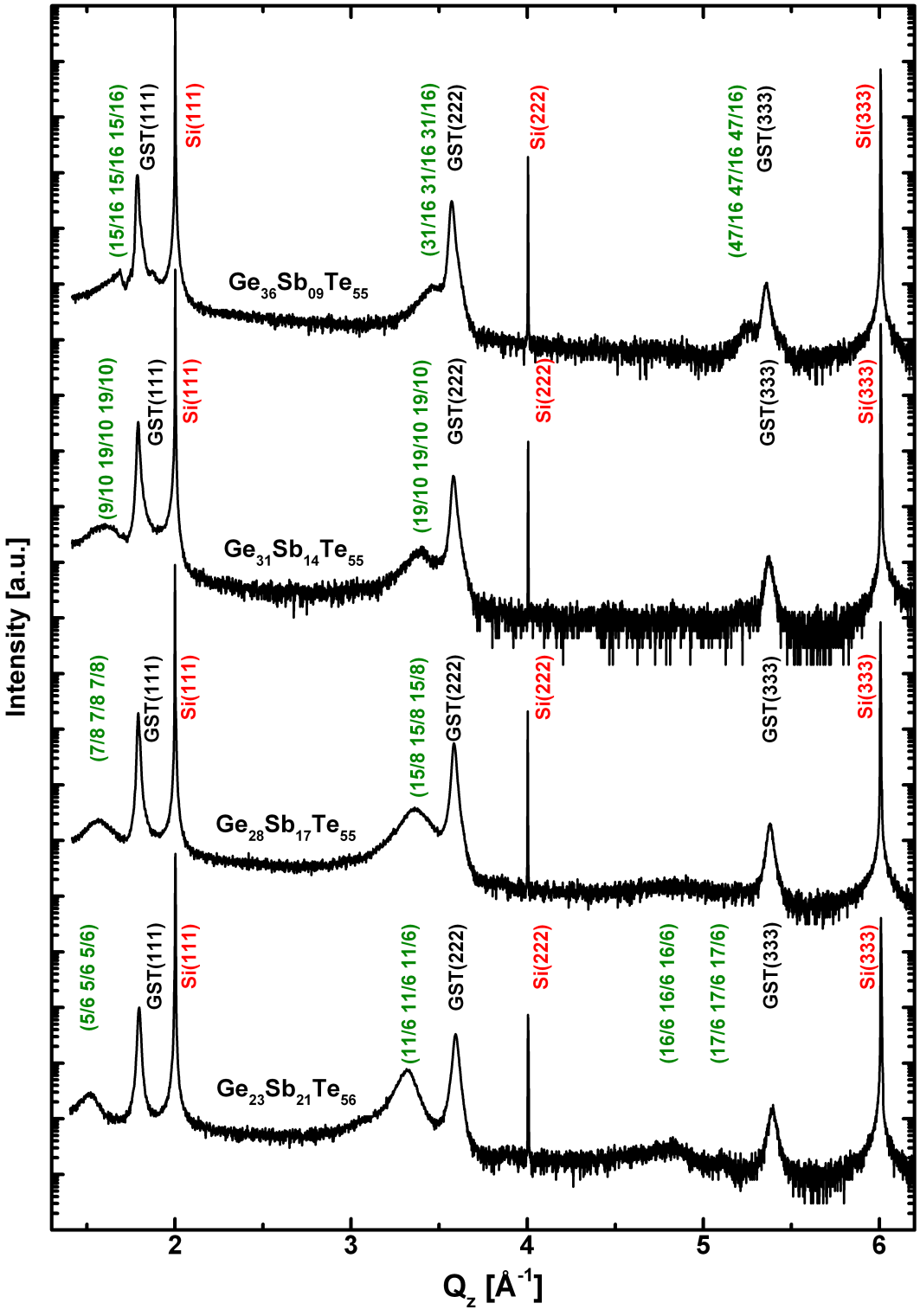

Figure 6.20: Specular $\omega - 2\theta$ XRD scan of GST grown on Si(111) using 2:2:5 flux. The compositions are given in the left bottom corner and the superstructural reflections (green) are represented in terms of fractional approximations. The superstructural cell size increases/decreases with increase in Ge/Sb content

Composition	**SSP1** [Å^{-1}]	**GST(111)** [Å^{-1}]	**SSP2** [Å^{-1}]	**GST(222)** [Å^{-1}]	l_{SSP1}	l_{SSP2}
$Ge_{24}Sb_{22}Te_{54}$	1.543	1.795	3.342	3.587	0.859 (6/7)	1.862 (13/7)
$Ge_{25}Sb_{21}Te_{54}$	1.551	1.795	3.344	3.588	0.864 (6/7)	1.864 (13/7)
$Ge_{26}Sb_{19}Te_{55}$	1.550	1.793	3.334	3.586	0.864 (6/7)	1.865 (13/7)
$Ge_{27}Sb_{19}Te_{54}$	1.556	1.793	3.346	3.584	0.868 (7/8)	1.867 (15/8)
$Ge_{28}Sb_{18}Te_{54}$	1.587	1.793	3.370	3.582	0.885 (8/9)	1.881 (17/9)

Table 6.2: Superstructural peak positions for samples grown using 2:3:5 flux

to GST unit cell. The fractional approximations are also given in table 6.2. As in the previous case, the intensity of the SSP close to GST(333) reflection are very weak and almost close to the background signal. Hence they are not given in table 6.2. Interestingly the size of the superstructural unit cell are almost the same i.e., 7 GST unit cells per superstructural unit cell along the [111] direction except for the last two samples with high Ge content, for which the superstructural peak corresponds to the size of 8 and 9 basic GST unit cells, respectively. Comparison of the samples grown using 2:2:5 flux and 2:3:5 flux show that the superstructural unit cell is identical for samples having similar composition.

6.4.3 Superstructures in Samples Grown using 3:2:5 Flux Ratio

It is trivial now to pay attention to those samples grown using higher Ge content. The composition of the samples and their corresponding superstructural peak positions are given in table 6.3 for scattering vectos up to 4 Å^{-1}.

Composition	**SSP1** [Å^{-1}]	**GST(111)** [Å^{-1}]	**SSP2** [Å^{-1}]	**GST(222)** [Å^{-1}]	l_{SSP1}	l_{SSP2}
$Ge_{29}Sb_{14}Te_{57}$	1.558	1.793	3.357	3.587	0.869 (7/8)	1.872 (15/8)
$Ge_{29}Sb_{15}Te_{56}$	1.578	1.795	3.374	3.587	0.879 (7/8)	1.881 (15/8)
$Ge_{36}Sb_{09}Te_{55}$	1.652	1.794	3.439	3.584	0.921 (11/12)	1.919 (23/12)
$Ge_{38}Sb_{07}Te_{55}$	-	1.794	-	3.586	-	-
$Ge_{44}Sb_{07}Te_{49}$	-	1.794	-	3.571	-	-

Table 6.3: Superstructural peak positions for samples grown using 3:2:5 flux

For samples with higher (lower) Ge (Sb, Te) concentration, the superstructural peaks almost vanish and only the GST reflections are visible and the specular $\omega - 2\theta$ scan is similar to the GeTe profile. The change in lattice parameter of GST is very minimal and hardly follows any relation with the change in composition. However the compositional changes are large with an increase in Ge content of about 15% , Sb content by about 7% and Te content by 8%. So, the disappearance of these SSPs might either be influenced by one of these materials Ge, Sb, Te or a combination of them.

We observed that for the $Ge_{38}Sb_7Te_{55}$ sample the SSP is almost like shoulder to the basic GST peak and it is hard to resolve. For $Ge_{44}Sb_7Te_{49}$ sample, the superstructural reflection

almost completely vanishes. In the next section for the samples grown using higher Te flux, we will further discuss this issue.

6.4.4 Superstructures in Samples Grown using 3:3:94 Flux Ratio

It is intriguing to understand why the SSPs disappeared at high (low) Ge (Sb,Te) concentration for the samples discussed in the previous section 6.4.3. Three parameters (i.e., Ge, Sb and Te content) might play a role in the appearance/disappearance of superstructural reflections. We already discussed the SSP evolution for samples grown using higher Ge and Sb fluxes in addition to the 2:2:5 flux. However it is not clear which material influences the formation of these superstructural peaks. In this section, we analyse $\omega - 2\theta$ XRD scans of samples grown at very high Te flux, almost 30 times the Ge, Sb fluxes. For the sake of uniformity with previous sections, in table 6.4 we present only those peaks that are close to the GST(111) and GST(222) reflections. The compositions are almost similar with very little variation in the Ge, Sb and Te content and the lattice parameter variation is also minimal ($< \pm 0.01$Å). However there is a large change in the position of the superstructural reflections, with an observed trend of the position of the peaks moving towards higher scattering vector values with decrease in Te content (Ge and Sb content variation does not follow a clear trend with change in position of the SSPs).

Composition	**SSP1** [Å^{-1}]	**GST(111)** [Å^{-1}]	**SSP2** [Å^{-1}]	**GST(222)** [Å^{-1}]	l_{SSP1}	l_{SSP2}
$Ge_{19}Sb_{18}Te_{63}$	1.423	1.819	3.245	3.632	0.783 (7/9)	1.785 (16/9)
$Ge_{19}Sb_{18}Te_{63}$	1.415	1.813	3.234	3.626	0.780 (7/9)	1.783 (16/9)
$Ge_{19}Sb_{18}Te_{63}$	1.427	1.812	3.243	3.623	0.788 (8/10)	1.789 (18/10)
$Ge_{20}Sb_{18}Te_{62}$	1.434	1.811	3.249	3.623	0.792 (8/10)	1.793 (18/10)
$Ge_{19}Sb_{19}Te_{62}$	1.441	1.816	3.260	3.632	0.794 (8/10)	1.794 (18/10)
$Ge_{22}Sb_{17}Te_{61}$	1.506	1.813	3.324	3.627	0.830 (10/12)	1.832 (22/12)

Table 6.4: Superstructural peak positions for samples grown using 3:3:94 flux

Figure 6.21 shows the typical specular CTR for samples grown using high Te flux. We observe that unlike the other set of samples, the samples with high Te content have more prominent SSPs and multiple order of the SSPs are present. With decrease in Te content more and more peaks are visible and clearly resolvable. The peak positions are fitted and the corresponding l_{SSP} values are found. The peak positions in terms of l_{SSP} are converted from decimals to fractional approximations to find the size of the superstructural unit cell. The fractional approximations of the superstructural reflections are given in figure 6.21 (green). The size of the supercell along the [111] direction increases from 9 to almost 12 basic GST unit cells.

Our assumptions of SSP originating from vacancy ordering are further strengthened with the observation of a large number of SSPs for samples grown with a high Te content. As the vacancy layers are expected to be inserted between the weakly bonded Te-Te layers, the presence of high concentration of Te atoms means more number of vacancy layers and its ordering along [111] direction. Recently Zhang et al., based on DFT calculations on disordered GST systems showed that metal-insulator transition favours the formation of ordered vacancy layers along the

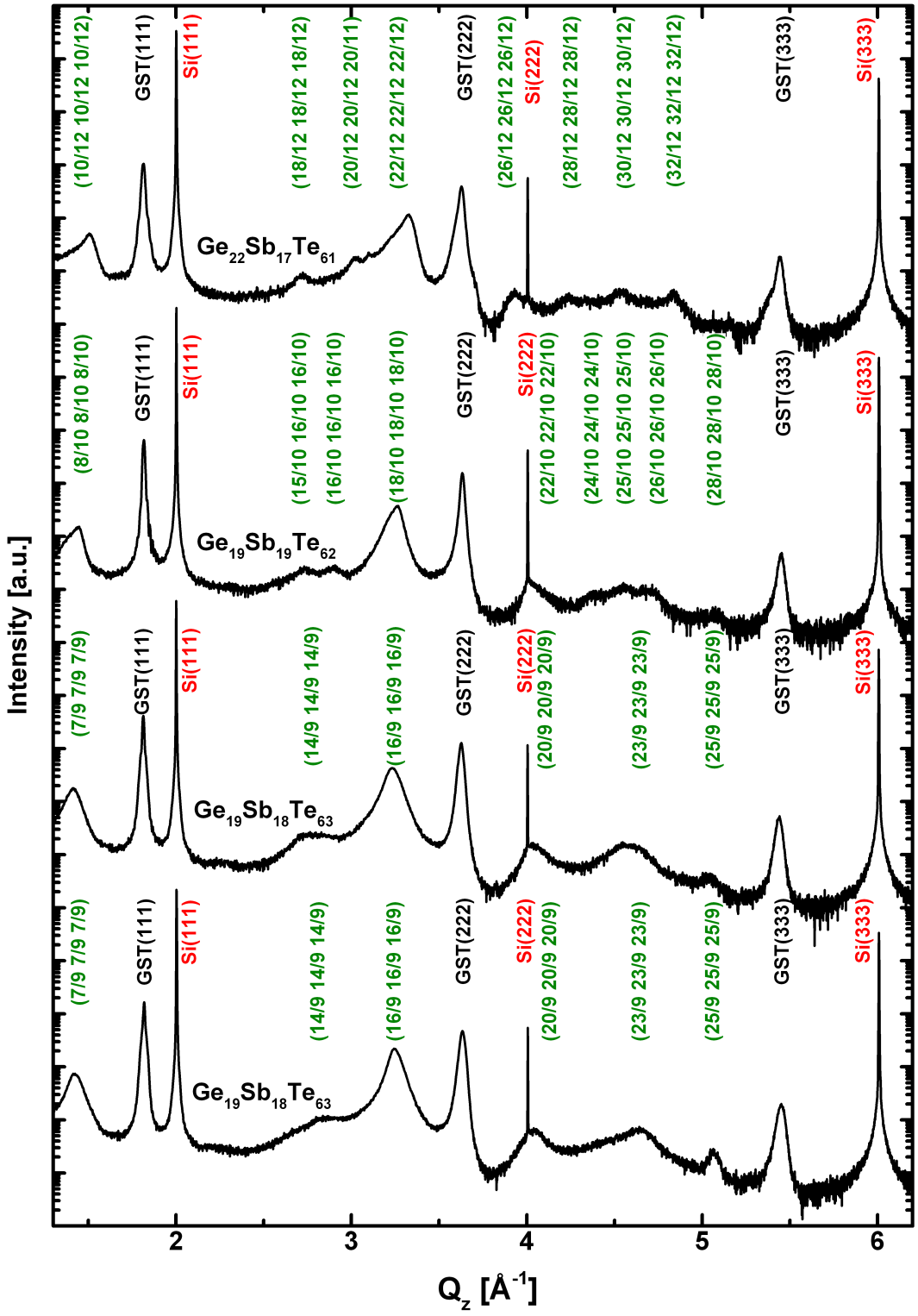

Figure 6.21: Specular $\omega - 2\theta$ XRD scan of GST grown on Si(111) using 3:3:94 flux. The compositions are given in the left bottom corner and the superstructural reflections (green) are represented in terms of fractional approximations. The superstructural peak becomes more predominant with decrease in Te concentration

[111] direction. Our results on superstructural peaks agree well with the theoretical works that vacancy layers are highly ordered and lie along the [111] direction[45,49,166].

6.5 *In-situ* Grazing Incidence X-Ray Diffraction

GST preferentially grows along the [111] direction on both Si(111) and Si(001) substrates. However, for the growth of GST on Si(001), a partial ordering of GST[001] along Si[111] direction is observed from the specular $\omega - 2\theta$ XRD scan. In-plane alignment of the epilayer with respect to the substrate is investigated in this section by *in-situ* grazing incidence synchrotron XRD.

6.5.1 GST Growth on Si(111)

The effusion cell base/hotlip temperatures of Ge, Sb and Te were set to (1097/1117), (470/620) and (340/476) °C respectively, such that the flux ratio is 2:2:5. The film was grown at 20% GeTe desorption and the film composition is estimated to be $Ge_2Sb_2Te_5$. Figure 6.22 shows the RSM at L = 0.1 rlu. The map was obtained by aligning the axes H and K to the high symmetry directions of the substrate i.e., H || Si[$\bar{2}$11] and K || Si[111], where H and K are represented in surface coordinates. The GST reflections are broad along the azimuthal direction. This is due to a slight twist of the epilayer with respect to the substrate. Apart from the intense GST peaks, a weak poly ring is observed. The intensity of the ring is almost 2-3 orders of magnitude less, indicating <1% of the film is polycrystalline. The map shows that the GST high symmetry in-plane directions orient themselves with those of the Si substrate i.e., GST[11$\bar{2}$] || Si[11$\bar{2}$] and GST[1$\bar{1}$0] || Si[1$\bar{1}$0]. GST peaks are observed every 60°, indicating a six-fold surface symmetry.

In-plane and out-of-plane scans were performed close to Si($\bar{2}$02) (figure 6.23 (a)) and Si(222) (figure 6.23 (b)) reflections to investigate the mismatch with respect to the substrate. Along the in-plane direction the lattice mismatch is about 9.93%, while it is 12.44% along the [111] direction. This indicates that the epilayer is distorted with the distortion found to be along the [111] direction.

Figure 6.24 shows an out-of-plane KL RSM, where the axis K is parallel to [$\bar{1}\bar{1}$2] direction. Sharp Bragg diffraction spots distributed along streaks parallel to the surface normal are observed. The presence of sharp CTRs indicate smooth surface of the GST epilayer. The film and substrate CTRs are well separated indicating the complete relaxation of the film. The substrate reflections (indexed in red) are given in cubic coordinates. At K = 0.9, L = 0.9 rlu GST peak is not expected as it should appear at K = -0.9 and L = 0.9 rlu. However a strong intensity along the crystal truncation rod at this point is visible. This peak can be explained by the rotation of the GST(111) netplanes by 180° around the surface normal. The intensity of this peak is almost equal to the primary reflections indicating about 50% twins. The twins in the KL RSM are indexed by a subscript ´twin´. No other additional reflections in the RSM are visible which indicates that the preferential growth direction is as that of the substrate orientation i.e., GST[111] || Si[111]. The in-plane and out-of-plane lattice constants vary with change in composition. Hence the above discussion is meant for that particular sample with composition of $Ge_2Sb_2Te_5$ and for a rigorous analysis of change in in-plane and out-of-plane lattice parameter with respect to film composition dedicated experiments have to be performed.

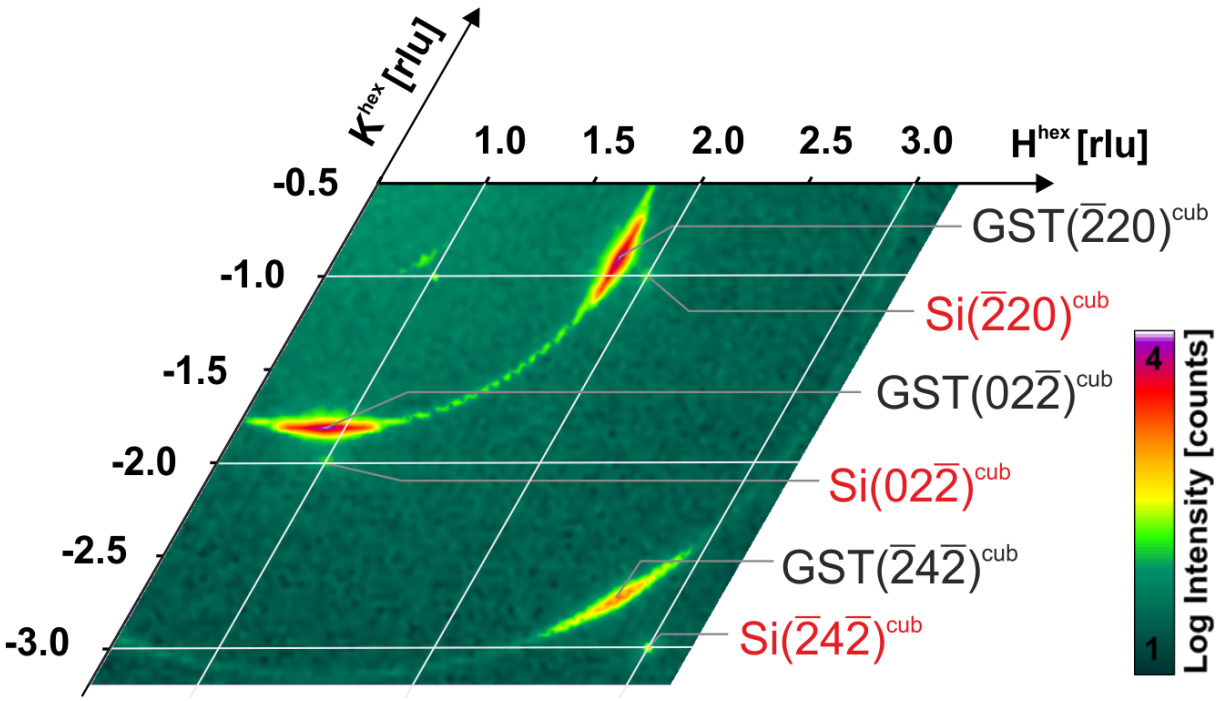

Figure 6.22: $H\overline{K}$ RSM measured by grazing incidence geometry. The substrate (red) and epilayer (black) reflections are given in bulk coordinates. A weak polycrystalline pattern is observed in addition to the twin reflections

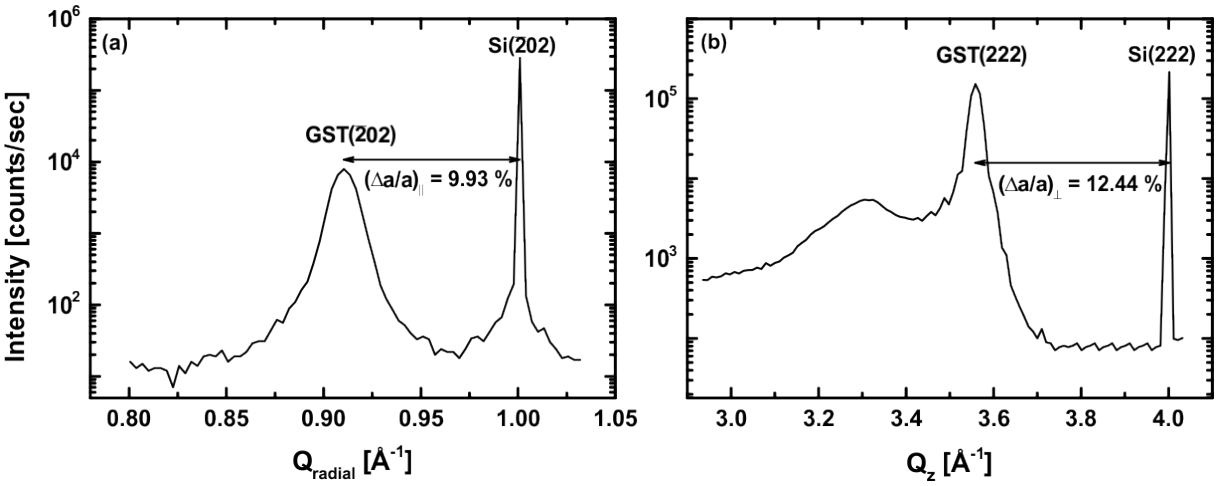

Figure 6.23: In-plane (a) and out-of-plane (b) XRD scans close to Si($\overline{2}$02) and Si(222) reflections respectively measured after the growth of GST on Si(111). The in-plane and out-of-plane lattice mismatch with respect to substrate are 9.93 and 12.44% respectively indicating a rhombohedral distortion along the [111] direction

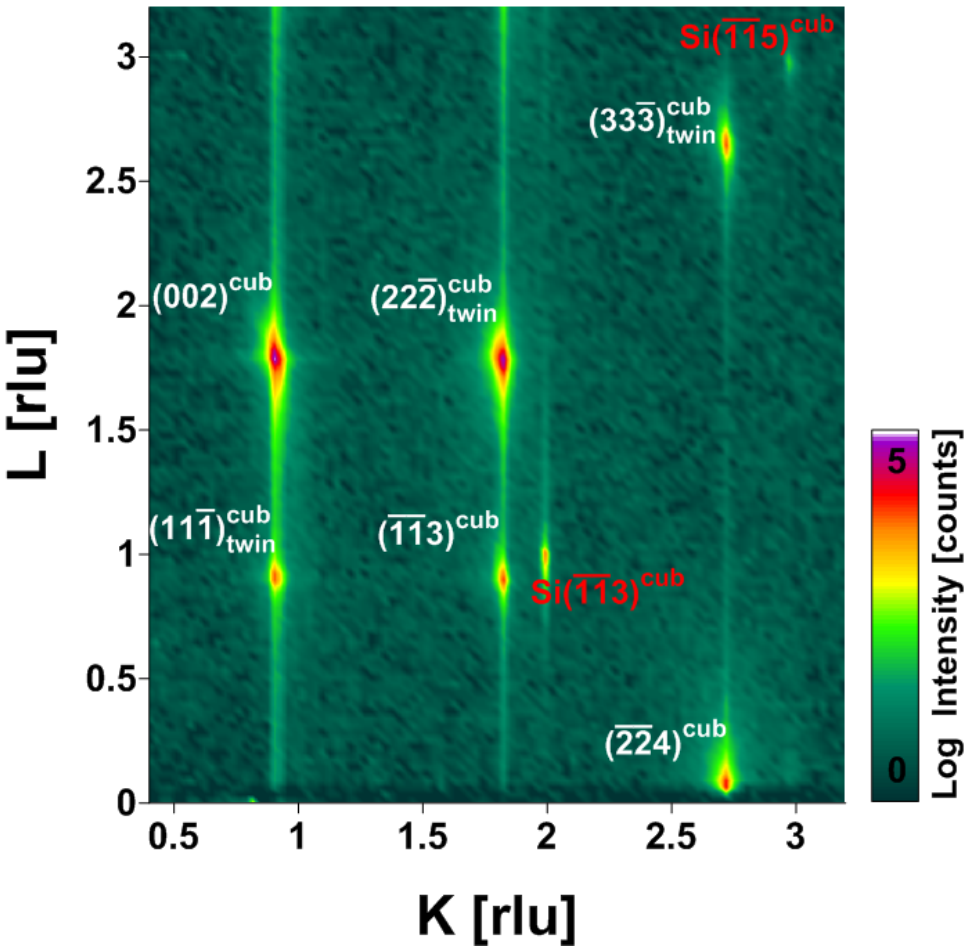

Figure 6.24: KL out-of-plane map measured in grazing incidence geometry after the growth of GST on Si(111). The axes K || Si[$\overline{1}\overline{1}$2] and L || Si[111] are given in surface coordinates, while the substrate (red), epilayer (white) and its twin reflections are given in cubic coordinates

6.5.2 GST Growth on Si(001)

For the sake of comparison with the growth on Si(111), the growth parameters for GST grown on Si(001) are kept unchanged. The estimated composition of the epilayer is $Ge_2Sb_2Te_5$. From the specular CTR (see figure 6.4), it is evident that the film predominantly grows along the [111] direction. It is interesting to know how the surface evolves structurally during the growth of GST on Si(001). Figure 6.25 (a) shows a series of L scans performed during the growth. The peak at L = 6.92 rlu corresponds to the Si(004) reflection, whereas GST(222) is observed at 5.34 rlu and the SSP at L = 4.96 rlu. The final thickness of the samples were determined by XRR and from the average growth rate, the time scale along the y-axis is converted to thickness. Each scan took 366 seconds and at the average growth rate of 0.64 nm/min, one scan corresponds to about 3.9 nm. So, the thickness error of this map is <3.9 nm. Peak position analysis during the growth indicates that during the initial growth stage, the out-of-plane lattice mismatch $(\Delta a/a)_\perp$

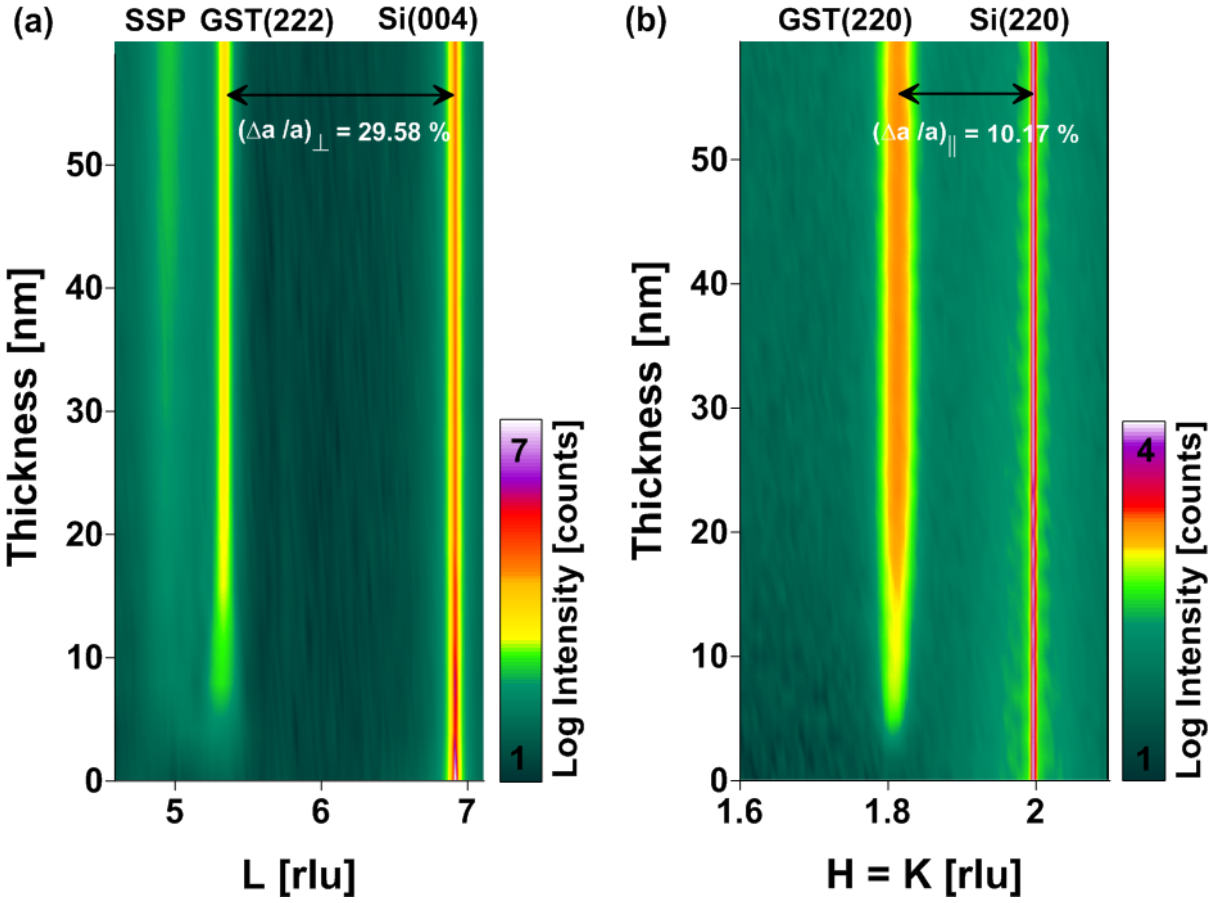

Figure 6.25: *In vivo* XRD studies during the growth of GST on Si(001). (a) out-of-plane scan around Si(004) reflection and (b) H=K scan (|| [110]) around Si(220) reflection

is about 30.07% and after about 24 nm thickness, the layer completely relaxes and reaches a final

value of ∼29.58%. The SSPs are observed right from the beginning of the growth (though of less intensity during the initial stages of nucleation) indicating that possible source fluctuations over time may not be the origin of the incommensurate reflections.

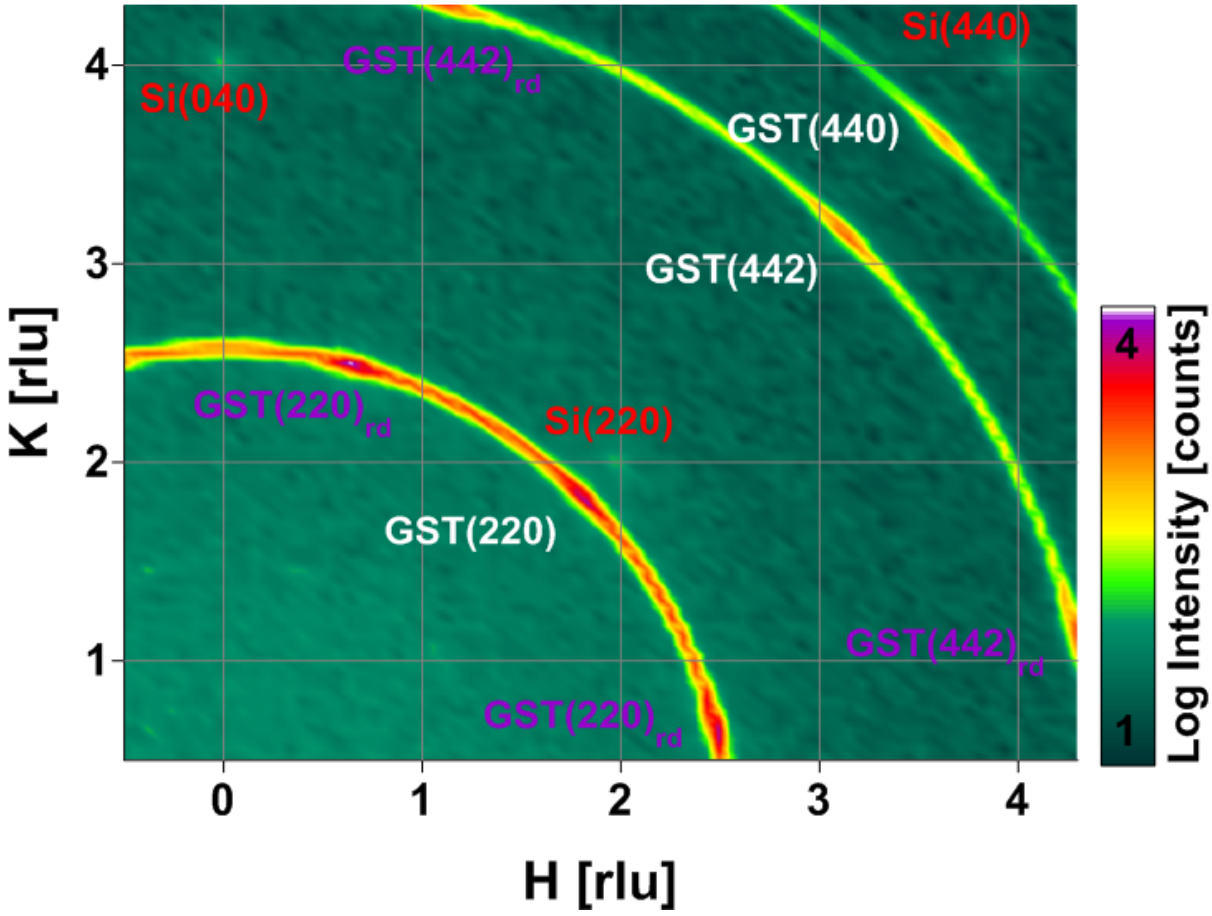

Figure 6.26: In-plane HK RSM of GST/Si(001) with the substrate reflections given in red, epilayer reflections in white and its 30° rotational domains in purple with subscript 'rd'. H and K are in cubic coordinates. Polycrystalline rings with intensity maxima every 30° are evident, indicating a 12 fold symmetry due to rotational domains

Figure 6.25 (b) shows a set of in-plane scans between 1.6 and 2.1 rlu. The peaks at 2 and 1.82 rlu correpond to the Si(220) and GST(220) reflections respectively. The in-plane scans are rather quick compared to the out-of-plane scans, and in this case each scan corresponds to about 155 seconds corresponding to a growth rate of 1.65 nm/scan. So, the thickness error shown in the map is within the limit of 1.65 nm. The lattice mimatch varies from around 10.54% to about 10.17% with respect to Si, from the initial stages of growth to a total relaxation around 25 nm. It is interesting to note that unlike GeTe, the GST in-plane peak position moves to higher scattering vector indicating a decrease in in-plane lattice parameter as the growth proceeds. On the contrary, it should be expected that the in-plane lattice parameter of GST

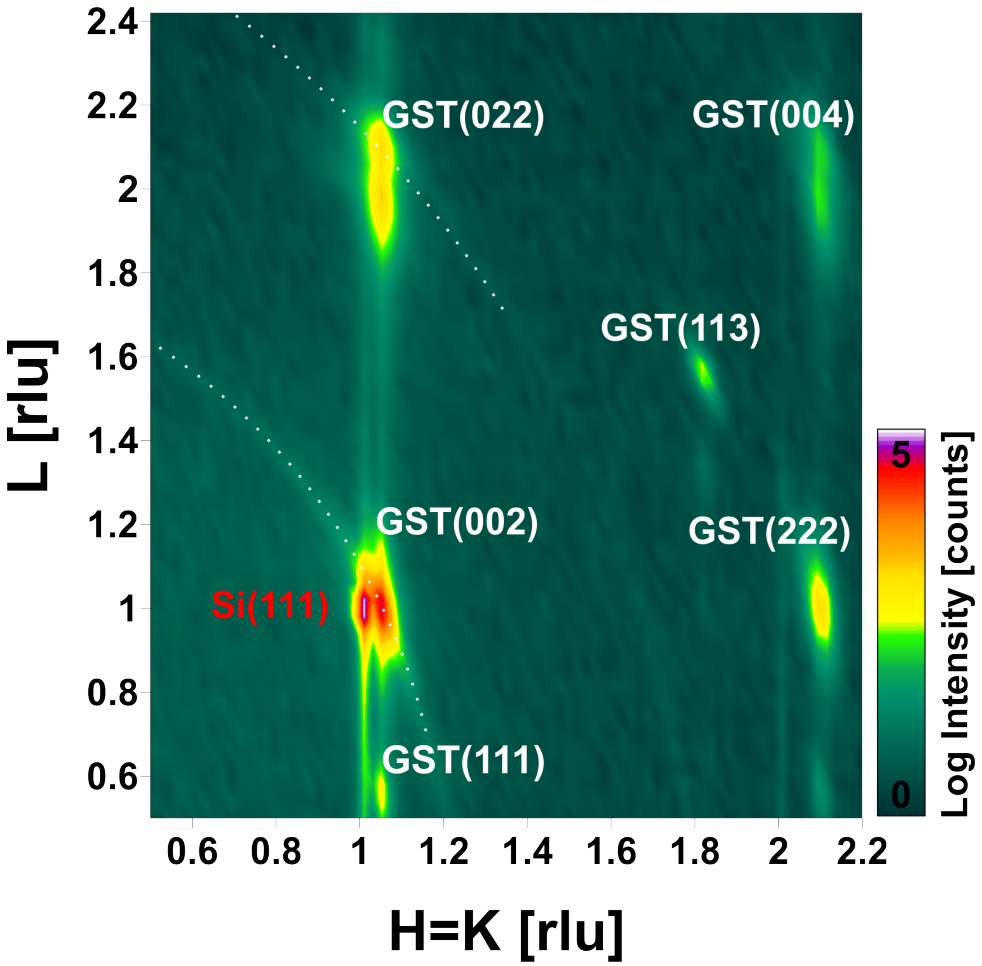

Figure 6.27: GST/Si(001): Out-of-plane RSM with both the axes and peak positions in cubic coordinates. A weak polycrystalline ring (indicated by dotted lines) is observed out-of-plane

should be compressively strained during nucleation to accommodate for the misfit and as it relaxes, it should go to lower scattering vector as the growth proceeds. No *in-vivo* growth studies were performed in this case and hence the effect of substrate orientation cannot be studied to understand this phenomenon.

Figure 6.26 shows an in-plane RSM. A strong polycrystalline feature is observed in-plane. The substrate reflections are indexed in red, while the layer reflections are in white. The first ring at low scattering vector corresponds to GST(220) netplanes, while the second and third ring correspond to GST(442) and (440) netplanes respectively. Every 30° around the surface normal, an intensity maximum is observed indicating a twelve fold symmetry. This indicates the presence of rotational domains. Rotational domains are expected if epilayer and substrate have different surface symmetry (see discussion in section 4.3.1)[122]. In our case, GST epilayer grown along [111] direction has a 6 fold symmetry and the Si[001] substrate has a four fold symmetry. 30° rotational domains are expected for the growth of epilayer with 6 fold symmetry on a substrate with 4 fold symmetry[122,124]. Figure 6.26 shows the 30° GST rotational domains indexed in purple.

Figure 6.27 shows the out-of-plane map with H = K || [110] direction and L || [001] direction. Weak polycrystalline rings along with broad peaks are observed indicating poor crystalline quality of the film. The substrate and epilayer reflections are indexed in red and white respectively. Though a weak polycrystalline feature is observed, the film predominantly grows along the [111] direction. In addition to the Si CTRs at H, K = 1 and 2 $Å^{-1}$, GST CTRs are observed at 1.05 and 2.10 $Å^{-1}$ indicating good interfacial quality of the epilayer. However, compared to the GST growth on Si(111) (see figure 6.24) the GST CTRs are weaker and in addition the structural quality is poor as can be seen from the broader GST reflections along the CTR. Though, on both substrate orientations the GST film prefers to grow along the [111] direction, the structural and interfacial quality are superior on the Si(111) substrates.

6.6 Conclusions

GST is found to have a very narrow growth window and the composition of the GST films is found to be highly dependent on growth temperature. GeTe desorption during growth is used to calibrate the growth temperature for each sample. An increase in GeTe desorption is observed indicating an increase in surface temperature. We propose to control the increase in surface temperature during growth, by keeping the desorption constant to achieve homogeneous composition along the growth direction.

A series of samples were grown using different initial flux at different desorption regimes. For 2:2:5 and 2:3:5 fluxes, the composition is shown to vary along the pseudobinary line when grown at different GeTe desorption regimes. Growth at higher Sb flux seems to be more promising as the compositional variation is minimal with respect to change in desorption as compared to the 2:2:5 flux. However, growth at high Ge and Te flux does not result in film composition along the technologically relevant GeTe-Sb_2Te_3 pseudobinary line.

Peaks due to incommensurate structure are observed for GST growth along the [111] direction. The peaks are attributed to superstructural ordering that results from unit cells larger than the GST unit cell along the [111] direction. These peaks become more predominant for compositions

with high Te content. From these results along with the theoretical work from other groups, we expect that these peaks might arise from vacancy ordering along the [111] direction.

Synchrotron grazing incidence studies show a slightly larger out-of-plane lattice parameter than the in-plane lattice parameter. This indicates the presence of distortion of the GST epilayer, with the distortion along the [111] direction. Growth on Si(111) shows single crystalline diffraction patterns with the presence of 180° twins. However polycrystalline features are observed for the growth of GST on Si(001) indicating that the growth on Si(111) is superior to the growth on Si(001). Along with the RHEED and synchrotron XRD measurements, we confirm that the growth on (111) oriented substrates seems to be more promising in terms of better surface morphology and crystalline quality.

7 Summary and Outlook

Phase change memories utilize the strong optical and electrical contrast between the amorphous and crystalline phases. Thin films of GST are usually prepared as polycrystalline layers which complicate the detailed understanding of switching mechanism and the structural transition associated with it. This study is necessitated by the desire to fabricate single crystalline GST films. Further, ordered metamaterials based on GeTe-Sb_2Te_3 superlattice like structures are shown to exhibit switching at lower energies compared to the monolithic polycrystalline counterparts[15]. MBE offers the ability to produce ordered materials that might have the advantage of the reduced switching energies. With this intention, the thesis is organized into three major topics. The first task is to understand the epitaxial growth of binary alloys which lie at the two ends of the GeTe-Sb_2Te_3 pseudobinary tie line, i.e., GeTe and Sb_2Te_3, followed by the growth of ternary GST alloys with composition along the GeTe-Sb_2Te_3 pseudobinary tie line.

7.1 Summary

1. Epitaxial growth of GeTe is achieved on highly lattice mismatched Si(111) and Si(001) substrates. Interestingly it was observed that the substrate orientation does not influence the growth direction of the GeTe epilayer, as GeTe prefers to grow along the [111] orientation on both (111) and (001) oriented Si substrates. RHEED evolution during growth shows the presence of an amorphous-to-crystalline transition on both substrate orientations. specular $\omega - 2\theta$ XRD scan of the amorphous stage during GeTe growth on Si(111) show peaks at half Bragg positions, indicating a superstructure which is twice the GeTe unit cell. However the superstructural peaks disappear when the amorphous-to-crystalline transition occurs. Epitaxy of GeTe on Si(111) shows the presence of rotational and twin domains with each maxima comprising of five symmetrically arranged peaks having a maximum separation of about 14°. Whereas the growth on Si(001) shows a twelve fold symmetry, indicating rotational domains every 30°.

   In-vivo out-of-plan XRD studies during the growth of GeTe on Si(111) show that the lattice mismatch increases rapidly during the nucleation stage and decreases above a thickness of 3 nm. While, in-plane scans during growth show peaks only after a thickness of 3 nm. This indicates that during the nucleation stage growth along different orientation is favoured, however after a critical thickness, the growth along the [111] direction seems to be predominant and the film prefers to grow along the [111] orientation. Azimuthal RHEED scans during growth show a diffuse four fold surface symmetry during the amorphous stage before turning to six fold surface symmetry, when the amorphous-to-crystalline transition occurs. This further adds up to our hypothesis that during the nucleation stage, a different orientation other than the [111] is preferred. The in-plane and out-of-plane lattice mismatch

of GeTe on Si(111) are 9.17% and 13.48% along [$\bar{2}$11] and [111] directions respectively, indicating a distortion along the [111] direction. XRF analysis of epitaxial GeTe films grown on Si(111) show a composition $Ge_{0.46}Te_{0.54}$ irrespective of the substrate temperatures. The QMS was calibrated from the XRF results to perform *in-situ* compositional analysis with an error percentage of <5%.

2. Epitaxial Sb_2Te_3 thin films were fabricated on largely lattice mismatched Si(111) substrates. XRR measurements show an abrupt interface and smooth surface morphology. Growths at higher substrate temperature were shown to exhibit reduced surface roughness of the film.

   Specular $\omega-2\theta$ XRD scans show that the epilayer is exclusively [00.1] oriented, aligning the high symmetry in-plane directions with the ones of the substrate i.e., Sb_2Te_3<11.0>||Si< $\bar{1}$01 > and Sb_2Te_3<10.0>||Si< $\bar{2}$11 >. In-plane azimuthal XRD scans show a strong twist as well as the presence of twins rotated by 180°.

3. GST growth on closely lattice matched substrates such as GaSb and InAs show that the epilayer retains the surface orientation during growth. However, it is contradictory on the growth of highly mismatched substrate such as Si, as the epilayer prefers to align its high symmetry out-of-plane direction along the [111] direction irrespective of the substrate orientation i.e., (111) or (001) surface. Synchrotron XRD studies show that the growth of GST on Si(111) is superior in terms of crystalline quality as compared to the growth on Si(001). For the growth on Si(001), polycrystalline rings are observed both in-plane and out-of-plane, as well as a weak out-of-plane orientation along the [001] direction.

   Composition of epitaxial GST films is shown to be largely dependent on substrate temperatures and a narrow epitaxial growth window of about 50 °C complicates the accurate control and reproducibility of the GST films. The problems are further aggravated by the use of a non-contact thermocouple to measure the substrate temperature, which fails to sense the increase in surface temperature over time. A new technique to control the growth by monitoring GeTe desoprtion is proposed and implemented in this thesis which might facilitate uniform composition along the growth direction.

   Films grown at different desorption regimes using 2:2:5 flux ratio show that, the composition of the films vary along the pseudobinary line from Sb_2Te_3 to GeTe with increase in GeTe desorption. An increase in supplied Sb flux by 1.5 times show that the composition does not vary much in desorption as compared to the growth under 2:2:5 flux ratio. Interestingly as soon as the film starts to grow in the epitaxial growth window, the composition of the samples falls along the pseudobinary tie line. However growth at high Ge or Te flux does not meet the requirement of growth along the technologically important pesudobinary line.

   Specular $\omega - 2\theta$ XRD scans of GST grown on closely lattice matched (GaSb, InAs) and highly mismatched (Si) substrates show that incommensurate peaks are observed for the growth along the [111] and not on the [001] direction. This indicates the presence of superstructural ordering along the [111] direction. These superstructural peaks become more predominant for compositions with high Te content. From these results along with

the theoretical work from other groups, we expect the incommensurate superstructural peaks might to be the resultant of vacancy ordering along the [111] direction.

7.2 Outlook

Though a sufficient amount of work was dedicated to investigate the MBE growth of GeTe-Sb_2Te_3 based phase change materials, there remains a lot of unsolved questions and areas of improvement in understanding and optimizing the epitaxy of phase change materials. On the basis of the results gathered within this thesis, the following experiments are envisioned:

1. The amorphous-to-crystalline transition or the so-called incubation stage during the epitaxy of GeTe on Si(111) and Si(001) might be interesting in terms of the structural point of view to understand why the growth always proceeds along the [111] direction irrespective of the substrate orientation. A superstructural unit cell along the [111] direction is observed during this incubation stage and there is no clear explanation, why the superstructural peak appears at the amorphous phase and disappears once the amorphous-to-crystalline transition takes place. Electron backscatter diffraction (EBSD) might help in knowing the preferred surface orientation (if any) of the initial incubation stage, however oxidation of the film might be a problem. With the movement of the GST MBE chamber back into the institute where EBSD facilities are available, this can be considered.

2. Though incommensurate superstructural peaks are expected to arise from vacancy ordering between Te-Te layers, the proof given in this work is not conclusive. Ge or Sb layer ordering is equally probable along the [111] direction. Detailed high resolution TEM studies or simulation of XRD pattern for various atomic arrangements might be necessary to conclusively establish the atomic arrangements of epitaxial GST along the [111] direction.

3. Phase change memories based on GeTe-Sb_2Te_3 superlattices are known to exhibit faster switching speeds and lower switching energies compared to their monolithic counterparts. Knowledge on the epitaxial growth of GeTe and Sb_2Te_3 should be used to fabricate and study the GeTe/Sb_2Te_3-based superlattices. Preliminary studies show smooth surface morphology and high cystalline quality of the superlattice grown on Si(111).

4. The growth work presented in this thesis was performed using three different atomic sources (i.e., Ge, Sb and Te). Usually PCMs are prepared via sputtering from molecular sources. It might be interesting to implement the epitaxy from molecular targets (such as GeTe, Sb_2Te_3, $Ge_2Sb_2Te_5$) and study the produced samples in terms of structural perfection and compositional control for comparison.

Program Code

The shutter in front of the QMS is closed every 20 seconds to monitor the real time change in background signals. For the QMS to be used for qualitative and quantitative analysis, it is necessary to remove the background from the desorption signal. The following Java^{TM} program is used to isolate the desorption signal and the background signal.

```
import java.io.BufferedReader;
import java.io.BufferedWriter;
import java.io.FileReader;
import java.io.FileWriter;
import java.util.StringTokenizer;

public class Main

{

public static void main(String[ ] args)

{

try

{

String strFile = "input file location";
String strFile1 = "output file location";
BufferedReader br = new BufferedReader(new FileReader(strFile));
BufferedWriter bw = new BufferedWriter(new FileWriter(strFile1));
String strLine = " ";
StringTokenizer st = null;
int lineNumber = 0, tokenNumber = 0;
float x1=1000;

while((strLine = br.readLine()) != null)

{

lineNumber++;
st = new StringTokenizer(strLine);
```

```
while(st.hasMoreTokens())

{

tokenNumber++;

if(lineNumber<2)

{

String x=st.nextToken();
String a=st.nextToken();
String b=st.nextToken();
String c=st.nextToken();
String d=st.nextToken();
String e=st.nextToken();
String f=st.nextToken();
String g=st.nextToken();
String h=st.nextToken();

System.out.println(" Line Number" + lineNumber + "\t" + a + "\t\t" + b +
"\t\t" + c + "\t\t" + d + "\t\t" + e + "\t\t" + f + "\t\t" + g + "\t\t" + h);

bw.write(a);
bw.write(",");
bw.write(b);
bw.write(",");
bw.write(c);
bw.write(",");
bw.write(d);
bw.write(",");
bw.write(e);
bw.write(",");
bw.write(f);
bw.write(",");
bw.write(g);
bw.write(",");
bw.write(h);
bw.newLine();
bw.flush();

}

else
```

```
{

String x=st.nextToken();
float a= Float.valueOf(st.nextToken());
float b= Float.valueOf(st.nextToken());
float c= Float.valueOf(st.nextToken());
float d= Float.valueOf(st.nextToken());
float e= Float.valueOf(st.nextToken());
float f= Float.valueOf(st.nextToken());
float g= Float.valueOf(st.nextToken());
float h= Float.valueOf(st.nextToken());

if((a>x1)&&(a<(x1+10000)))

{

System.out.println("Line Number" + lineNumber + "\t" + a + "\t\t" + b +
\t\t" + c + "\t\t" + d + "\t\t" + e + "\t\t" + f + "\t\t" + g + "\t\t" + h);

String str1 = Float.toString(a);
String str2 = Float.toString(b);
String str3 = Float.toString(c);
String str4 = Float.toString(d);
String str5 = Float.toString(e);
String str6 = Float.toString(f);
String str7 = Float.toString(g);
String str8 = Float.toString(h);

bw.write(str1);
bw.write(",");
bw.write(str2);
bw.write(",");
bw.write(str3);
bw.write(",");
bw.write(str4);
bw.write(",");
bw.write(str5);
bw.write(",");
bw.write(str6);
bw.write(",");
bw.write(str7);
bw.write(",");
bw.write(str8);
bw.newLine();
```

```
bw.flush();
}
else
if(a>x1)
{
x1=x1+40000;
}
}
}
tokenNumber = 0;
}
bw.close();
}
catch(Exception e)
{
System.out.println(" Exception while reading csv file: " +e);
}
}
}
```

List of Acronyms

2D	2-Dimensional
3D	3-Dimensional
AFM	Atomic Force Microscopy
BD	Blu-ray Disc
BEP	Beam Equivalent Pressure
BESSY	Berliner Elektronenspeicherring-Gesellschaft für Synchrotronstrahlung
CD	Compact Disc
CTR	Crystal Truncation Rod
DCM	Double Crystal Monochromator
DI	Deionized
DRAM	Dynamic Random Access Memory
DVD	Digital Versatile Disc
EXAFS	Extended X-Ray Absorption Fine Structure
FWHM	Full Width at Half Maximum
GB	Giga Byte
GIXRD	Grazing Incidence X-Ray Diffraction
GST	GeTe-Sb_2Te_3
KMC	Kristallmonochromator
MB	Mega Byte
MBE	Molecular Beam Epitaxy
MOCVD	Metalorganic Chemical Vapour Deposition
PCM	Phase Change Materials
PCRAM	Phase Change Random Access Memory
QMS	Quadrupole Mass Spectrometer
RHEED	Reflection High-Energy Electron Diffraction
rms	Root Mean Square
RSM	Reciprocal Space Map
SEM	Scanning Electron Microscopy
SSP	Superstructural Peak
UHV	Ultra High Vacuum
XRD	X-Ray Diffraction
XRF	X-Ray Fluorescence
XRR	X-Ray Reflectivity

Publication List

Peer Reviewed Publications

- F. Katmis, R. Calarco, K. Perumal, P. Rodenbach, A. Giussani, M. Hanke, A. Proessdorf, A. Trampert, F. Grosse, R. Shayduk, R. Campion, W. Braun and H. Riechert, *Insight into the growth and control of single-crystal layers of Ge-Sb-Te phase-change material*, Crystal Growth & Design **11**, 4606-4610 (2011)
- P. Rodenbach, K. Perumal, F. Katmis, W. Braun, R. Calarco and H. Riechert, *Epitaxy of single crystal phase change materials on Si(111)*, MRS Proceedings, **1338**, r05-10-5 (2011)
- M. Krbal, A. V. Kolobov, P. Fons, J. Tominaga, S. R. Elliott, J. Hegedus, A. Giussani, K. Perumal, R. Calarco, T. Matsunaga, N. Yamada, K. Nitta and T. Uruga, *Crystalline GeTe-based phase-change alloys: Disorder in order*, Physical Review B, **86**, 045212 (2012)
- A. Proessdorf, F. Grosse, K. Perumal, W. Braun and H. Riechert, *Anisotropic interface induced formation of Sb nanowires on GaSb(111)A substrates*, Nanotechnology, **23**, 235301 (2012)
- P. Rodenbach, R. Calarco, K. Perumal, F. Katmis, M. Hanke, A. Proessdorf, W. Braun, A. Giussani, A. Trampert, H. Riechert, P. Fons and A. V. Kolobov, *Epitaxial phase-change materials*, Physica Status Solidi - Rapid Research Letters, **6**, 415-417 (2012)
- P. Rodenbach, A. Giussani, K. Perumal, M. Hanke, M. Dubslaff, H. Riechert, R. Calarco, M. Burghammer, A. V. Kolobov and P. Fons, *Recrystallization of an amorphized epitaxial phase-change alloy: A Phoenix arising from the ashes*, Applied Physics Letters, **101**, 061903 (2012)
- Y. Takagaki, A. Giussani, K. Perumal, R. Calarco and K. -J. Friedland, *Robust topological surface states in Sb_2Te_3 layers as seen from the weak antilocalization effect*, Physical Review B, **86**, 125137 (2012)
- A. Giussani, K. Perumal, M. Hanke, P. Rodenbach, H. Riechert and R. Calarco *On the epitaxy of germanium telluride thin films on silicon substrates*, Physica Status Solidi B, **249**, 1939-1944 (2012)

Non-Peer Reviewed Publications

- W. Braun, F. Katmis, K. Perumal and R. Shayduk, *Molecular beam epitaxy of GST controlled by quadrupole mass spectrometry*, European\Phase Change and Ovonics Symposium (2010)

- ◇ A. Giussani, K. Perumal, P. Rodenbach, M. Hanke, W. Braun, R. Calarco and H. Riechert, *Structure and composition of Ge-Sb-Te thin films grown by molecular beam epitaxy on Si(111) substrates*, European\Phase Change and Ovonics Symposium (2011)
- ◇ K. Perumal, W. Braun, H. Riechert and R. Calarco, *Desorption Kinetics of GeTe deposited on Si(111)*, European\Phase Change and Ovonics Symposium (2012)

Conference Contributions

- ◇ K. Perumal, A. Giussani, P. Rodenbach, M. Hanke, W. Braun, R. Calarco and H. Riechert, *In-situ growth control of epitaxial Ge-Sb-Te films on Si(111) using a line-of-sight quadrupole mass spectrometer*, MRS Spring Meeting, San Francisco (2012)
- ◇ R. Calarco, K. Perumal, A. Giussani, P. Rodenbach, M. Hanke and H. Riechert, *Growth morphology and structure of GeTe-Sb_2Te_3 heterostructures grown on Si(111) substrates*, MRS Spring Meeting, San Francisco (2012)
- ◇ P. Rodenbach, P. Fons, A. Giussani, K. Perumal, M. Dubslaff, M. Hanke, R. Calarco and H. Riechert, *Structural order of laser switched single crystal $Ge_2Sb_2Te_5$*, MRS Spring Meeting, San Francisco (2012)
- ◇ K. Perumal, P. Rodenbach, M. Hanke, A. Giussani, W. Braun, R. Calarco and H. Riechert, *Epitaxial phase change materials: Structure and composition*, BESSY User Meeting, Berlin (2012)
- ◇ K. Perumal, R. Calarco, F. Grosse, W. Braun, H. Riechert, *Growth of epitaxial $Ge_{.}46Te{-}.54$ on Si(111)*, International Symposium on Compound Semiconductors, Berlin (2011)
- ◇ K. Perumal, W. Braun and R. Calarco, *Epitaxial growth of GeTe on Si(111) and in-situ compositional analysis*, DPG Spring Meeting, Dresden (2011)
- ◇ P. Rodenbach, K. Perumal, F. Katmis, W. Braun, R. Calarco and H. Riechert, *High quality epitaxy of phase change materials on lattice matched and mismatched substrates*, MRS Spring Meeting, San Francisco (2011)
- ◇ K. Perumal, emphAn introduction to phase change materials, DAAD Wise Meeting, Berlin (2010)

Berlin, den July 17, 2013 Karthick Perumal

Bibliography

[1] G. E. Moore. Cramming more components onto integrated circuits. *Electronics*, 38(8), 1965.

[2] International Technology Roadmap for Semiconductors. Technical report, 2011.

[3] N. Papandreou, H. Pozidis, T. Mittelholzer, G. F. Close, M. Breitwisch, C. Lam, and E. Eleftheriou. Drift-tolerant multilevel phase-change memory. *2011 3rd IEEE International Memory Workshop (IMW)*, pages 1–4, May 2011.

[4] C. D. Wright, Y. Liu, K. I. Kohary, M. M. Aziz, and R. J. Hicken. Arithmetic and biologically inspired computing using phase change materials. *Advanced Materials*, 23: 3408–13, August 2011.

[5] T. Ohta. Phase-change optical memory promotes the DVD optical disk. *Journal of Optoelectronics and Advanced Materials*, 3(3):609–626, 2001.

[6] L. Bo, R. Hao, and G. Fu-Xi. Crystallization of $Ge_2Sb_2Te_5$ phase-change optical disk media. *Chinese Physics*, 11(3):293, 2002.

[7] J. Siegel, A. Schropp, J. Solis, C. N. Afonso, and M. Wuttig. Rewritable phase-change optical recording in $Ge_2Sb_2Te_5$ films induced by picosecond laser pulses. *Applied Physics Letters*, 84(13):2250, 2004.

[8] T. A. Kiyama, M. Umo, H. Kitaura, K. Narumi, R. Kojima, K. Nishiuchi, and N. Yamada. Rewritable dual-layer phase-change optical disk utilizing a blue-violet laser. *Japanese Journal of Applied Physics*, 40:1598–1603, 2001.

[9] T. Ohta, M. Birukawa, N. Yamada, and K. Hirao. Optical recording; phase-change and magneto-optical recording. *Journal of Magnetism and Magnetic Materials*, 242-245:108–115, April 2002.

[10] T. Nishihara, A. Tsuchino, Y. Tomekawa, H. Kusada, R. Kojima, and N. Yamada. Rewritable triple-layer phase-change optical disk providing 100 Gbyte capacity. *Japanese Journal of Applied Physics*, 50(6):062503, June 2011.

[11] A.V. Kolobov, P. Fons, A.I. Frenkel, A.L. Ankudinov, J. Tominaga, and T. Uruga. Understanding the phase-change mechanism of rewritable optical media. *Nature Materials*, 3(10):703, 2004.

[12] A.V. Kolobov, M. Krbal, P. Fons, J. Tominaga, and T. Uruga. Distortion-triggered loss of long-range order in solids with bonding energy hierarchy. *Nature Chemistry*, 3(4):311–316, March 2011.

[13] T Siegrist, P Jost, H Volker, M Woda, P Merkelbach, C Schlockermann, and M Wuttig. Disorder-induced localization in crystalline phase-change materials. *Nature materials*, 10 (3):202–208, January 2011.

[14] J. Tominaga, P. Fons, A. V. Kolobov, T. Shima, T. C. Chong, R. Zhao, H. K. Lee, and L. Shi. Role of Ge switch in phase transition: Approach using atomically controlled GeTe/Sb_2Te_3 superlattice. *Japanese Journal of Applied Physics*, 47(No. 7):5763–5766, July 2008.

[15] R. E. Simpson, P. Fons, A. V. Kolobov, T. Fukaya, M. Krbal, T. Yagi, and J. Tominaga. Interfacial phase-change memory. *Nature Nanotechnology*, 6:501–505, 2011.

[16] E. F. Steigmeier and G. Harbeke. Soft phonon mode and ferroelectricity in GeTe. *Solid State Communications*, 8:1275–1279, 1970.

[17] W. D. Johnston and D. E. Sestrich. The MnTe-GeTe phase diagram. *Journal of Inorganic and Nuclear Chemistry*, 19:229–236, October 1961.

[18] H. Wiedemeier and P. A. Siemers. The thermal expansion of GeS and GeTe. *Zeitschrift für anorganische und allgemeine Chemie*, 431:299–304, June 1977.

[19] T. Chattopadhyay, J. X. Boucherle, and H. G. von Schnering. Neutron diffraction study on the structural phase transition in GeTe. *Journal of Physics C: Solid State Physics*, 20 (1):1431, March 1987.

[20] J. P. Gaspard, A. Pellegatti, F. Marinelli, and C. Bichara. Peierls instabilities in covalent structures I . Electronic Structure , cohesion and the Z = 8 - N rule. *Philosophical Magazine B*, 77(3):727, 1998.

[21] A. V. Kolobov, J. Tominaga, P. Fons, and T. Uruga. Local structure of crystallized GeTe films. *Applied Physics Letters*, 82(3):382, 2003.

[22] A. V. Kolobov, P. Fons, J. Tominaga, A. L. Ankudinov, S. N. Yannopoulos, and K. S. Andrikopoulos. Crystallization-induced short-range order changes in amorphous GeTe. *Journal of Physics: Condensed Matter*, 16(44):S5103–S5108, November 2004.

[23] P. Fons, A. Kolobov, M. Krbal, J. Tominaga, K. Andrikopoulos, S. Yannopoulos, G. Voyiatzis, and T. Uruga. Phase transition in crystalline GeTe: Pitfalls of averaging effects. *Physical Review B*, 82(15):2–6, October 2010.

[24] J. Y. Raty, J. P. Gaspard, C. Bichara, C. Bergman, R. Bellissent, and R. Ceolin. Reentrant Peierls distortion in IV-VI compounds. *Physica B: Condensed Matter*, 276-278: 473–474, March 2000.

[25] J. Y. Raty, J. P. Gaspard, M. Bionducci, R. Ceolin, and R. Bellissent. On the structure of liquid IV-VI semiconductors. *Journal of Non-Crystalline Solids*, 250-252:277–280, 1999.

[26] J. Y. Raty, V. Godlevsky, Ph. Ghosez, C. Bichara, J. P. Gaspard, and J. R. Chelikowsky. Evidence of a reentrant Peierls distortion in liquid GeTe. *Physical Review Letters*, 85(9): 1950–1953, 2000.

[27] G. Lucovsky and R. M. White. Effects of resonance bonding on the properties of crystalline and amorphous semiconductors. *Physical Review B*, 8(2):660, 1973.

[28] A. Schlieper, Y. Feutelais, S. G. Fries, and B. Legendre. Thermodynamic evaluation of the Germanium-Tellurium system. *Calphad*, 23(1):1–18, 1999.

[29] B. Vengalis. Phase segregation in tellurium-saturated GeTe. *Physica Status Solidi (b)*, 471:471–476, 1983.

[30] J. C. Woolley and P. Nikolic. Some properties of GeTe-PbTe alloys. *Journal of The Electrochemical Society*, 112(1):82–84, 1965.

[31] R. Tsu, W. E. Howard, and L. Esaki. Optical properties of GeTe. *Solid State Communications*, 5:167–171, 1967.

[32] S. K. Bahl and K. L. Chopra. Amorphous versus crystalline GeTe films III. Electrical properties and band structure. *Journal of Applied Physics*, 41(5):2196–2212, 1970.

[33] L. Vadkhiya, G. Arora, A. Rathor, and B. L. Ahuja. Electron momentum density and band structure calculations of α- and β-GeTe. *Radiation Physics and Chemistry*, 80:1316–1322, December 2011.

[34] E. Huber and E. E. Marinero. Laser-induced crystallization of amorphous GeTe: A time-resolved study. *Physical Review B*, 36(3):1595, 1987.

[35] P. Nath and K. L. Chopra. Thermal conductivity of amorphous and crystalline Ge and GeTe films. *Physical Review B*, 10(8):3412, 1974.

[36] E. K. Chua, L. P. Shi, R. Zhao, K. G. Lim, T. C. Chong, T. E. Schlesinger, and J. A. Bain. Low resistance, high dynamic range reconfigurable phase change switch for radio frequency applications. *Applied Physics Letters*, 97(18):183506, 2010.

[37] K. Shportko, S. Kremers, M. Woda, D. Lencer, J. Robertson, and M. Wuttig. Resonant bonding in crystalline phase-change materials. *Nature Materials*, 7(8):653–8, August 2008.

[38] N. Yamada, E. Ohno, N. Akahira, and K. I. Nishiuchi. High speed overwritable phase change optical disk material: MEDIA. *Japanese Journal of Applied Physics*, 26(4):61–66, 1987.

[39] N. Yamada and T. Matsunaga. Structure of laser-crystallized $Ge_2Sb_{2+x}Te_5$ sputtered thin films for use in optical memory. *Journal of Applied Physics*, 88(12):7020–7028, 2000.

[40] T. Nonaka, G. Ohbayashi, Y. Toriumi, Y. Mori, and H. Hashimoto. Crystal structure of GeTe and $Ge_2Sb_2Te_5$ metastable phase. *Thin Solid Films*, 370:258–261, July 2000.

[41] J-H. Eom, Y-G. Yoon, C. Park, H. Lee, J. Im, D-S. Suh, J-S. Noh, Y. Khang, and J. Ihm. Global and local structures of the Ge-Sb-Te ternary alloy system for a phase-change memory device. *Physical Review B*, 73:214202, 2006.

[42] J. Akola and R. O. Jones. Structure of amorphous $Ge_8Sb_2Te_{11}$: GeTe-Sb_2Te_3 alloys and optical storage. *Physical Review B*, 79:134118, April 2009.

[43] T. Matsunaga, H. Morita, R. Kojima, N. Yamada, K. Kifune, Y. Kubota, Y. Tabata, J. J. Kim, M. Kobata, E. Ikenaga, and K. Kobayashi. Structural characteristics of GeTe-rich GeTe-Sb_2Te_3 pseudobinary metastable crystals. *Journal of Applied Physics*, 103(9): 093511, 2008.

[44] T. Matsunaga and N. Yamada. Structural investigation of $GeSb_2Te_4$: A high-speed phase-change material. *Physical Review B*, 69(10):104111, March 2004.

[45] J. Zhou, Z. Sun, Y. Pan, Z. Song, and R. Ahuja. Vacancy or not: An insight on the intrinsic vacancies in rocksalt-structured GeSbTe alloys from *ab initio* calculations. *Europhysics Letters*, 95(2):27002, July 2011.

[46] I. I. Petrov, R. M. Imamov, and Z. G. Pinsker. Structures of $Ge_2Sb_2Te_5$ and $GeSb_4Te_7$. *Soviet Physics - Crystallography*, 13(3):339–342, 1968.

[47] B. J. Kooi and J. Th. M. De Hosson. Electron diffraction and high-resolution transmission electron microscopy of the high temperature crystal structures of $Ge_xSb_2Te_{3+x}$ (x=1,2,3) phase change material. *Journal of Applied Physics*, 92(7):3584, 2002.

[48] T. Matsunaga, N. Yamada, and Y. Kubota. Structures of stable and metastable $Ge_2Sb_2Te_5$, an intermetallic compound in GeTe-Sb_2Te_3 pseudobinary systems. *Acta Crystallographica Section B: Structural Science*, 60(Pt 6):685–91, December 2004.

[49] Z. Sun, J. Zhou, and R. Ahuja. Structure of phase change materials for data storage. *Physical Review Letters*, 96(5):055507, February 2006.

[50] X. Q. Liu, X. B. Li, L. Zhang, Y. Q. Cheng, Z. G. Yan, M. Xu, X. D. Han, S. B. Zhang, Z. Zhang, and E. Ma. New structural picture of the $Ge_2Sb_2Te_5$ phase-change alloy. *Physical Review Letters*, 106:025501, 2011.

[51] A. V. Kolobov, P. Fons, J. Tominaga, A. I. Frenkel, A. L. Ankudinov, and T. Uruga. Local structure of Ge-Sb-Te and its modification upon the phase transition. *Journal of Ovonic Research*, 1(1):21–24, 2005.

[52] J-W. Park, S. H. Baek, T. D. Kang, H. Lee, Y-S. Kang, T-Y. Lee, D-S. Suh, K. J. Kim, C. K. Kim, Y. H. Khang, J. L. F. Da Silva, and S-H. Wei. Optical properties of (GeTe, Sb_2Te_3) pseudobinary thin films studied with spectroscopic ellipsometry. *Applied Physics Letters*, 93:021914, 2008.

[53] J-W. Park, S. Eom, H. Lee, J. Da Silva, Y-S. Kang, T-Y. Lee, and Y. Khang. Optical properties of pseudobinary GeTe, $Ge_2Sb_2Te_5$, $GeSb_2Te_4$, $GeSb_4Te_7$, and Sb_2Te_3 from ellipsometry and density functional theory. *Physical Review B*, 80:115209, 2009.

[54] J. M. Yanez-Limon, J. Gonzalez-Hernandez, J. J. Alvardo-Gil, I. Delgadillo, and H. Vargas. Thermal and electrical properties of the Ge:Sb:Te system by photoacoustic and Hall measurements. *Physical review B*, 52(23), 1995.

[55] M. Wuttig and N. Yamada. Phase-change materials for rewriteable data storage. *Nature Materials*, 6(11):824–32, 2007.

[56] S. Karamazov, P. Nesladek, J. Horak, and M. Matyas. Vegard's rule and $Sb_2Te_{3-x}Se_x$ crystals. *Physica Status Solidi (B)*, 194:187, 1996.

[57] T. L. Anderson and H. B. Krause. Refinement of the Sb_2Te_3 and Sb_2Te_2Se structures and their relationship to non-stoichiometric $Sb_2Te_{3-y}Se_y$ compounds. *Acta Crystallographica Section B:*, 30:1307–1310, 1974.

[58] I. Teramoto and S. Takayanagi. Relations between the electronic properties and the chemical bonding of $Sb_xBi_{2-x}Te_{3-y}Se_y$ system. *Journal of Physics and Chemistry of Solids*, 19 (1/2):124–129, 1961.

[59] E. Dönges. Über tellurohalogenide des dreiwertigen antimons und wismuts und über antimon- und wismut(III)-tellurid und wismut(III)-selenid. *Zeitschrift für Anorganische und Allgemeine Chemie*, 265:56, 1951.

[60] J. L. F. Da Silva, A. Walsh, and H. Lee. Insights into the structure of the stable and metastable $(GeTe)_m(Sb_2Te_s)_n$ compounds. *Physical Review B*, 78:224111, December 2008.

[61] K. Tani, N. Yiwata, M. Harigaya, S. Emura, and Y. Nakata. EXAFS study of Sb-Te alloy films. *Journal of Synchrotron Radiation*, 8:749–751, March 2001.

[62] R. Sehr and L. R. Testardi. The optical properties of p-type Bi_2Te_3-Sb_2Te_3 alloys between 2-15 microns. *Journal of Physics and Chemistry of Solids*, 23:1219–1224, 1962.

[63] V. D. Das and N. Soundararajan. Thermoelectric power and electrical resistivity of crystalline antimony telluride (Sb_2Te_3) thin films: Temperature and size effects. *Journal of Applied Physics*, 65(6):2332, 1989.

[64] Y. Kim, A. DiVenere, G. K. L. Wong, J. B. Ketterson, S. Cho, and J. R. Meyer. Structural and thermoelectric transport properties of Sb_2Te_3 thin films grown by molecular beam epitaxy. *Journal of Applied Physics*, 91(2):715–718, 2002.

[65] G. Wang, X. Zhu, J. Wen, X. Chen, K. He, L. Wang, X. Ma, Y. Liu, X. Dai, Z. Fang, J. Jia, and Q. Xue. Atomically smooth ultrathin films of topological insulator Sb_2Te_3. *Nano Research*, 3(12):874–880, November 2010.

[66] Y. Takagaki, A. Giussani, K. Perumal, R. Calarco, and K. Friedland. Robust topological surface states in Sb_2Te_3 layers as seen from the weak antilocalization effect. *Physical Review B*, 86(12):125137, 2012.

[67] S. R. Ovshinsky. Symmetrical current controlling device, 1966.

[68] D-H. Kang, D-H. Ahn, M-H. Kwon, H-S. Kwon, K-B. Kim, K. S. Lee, and B-K. Cheong. Lower voltage operation of a phase change memory device with a highly resistive TiON layer. *Japanese Journal of Applied Physics*, 43(8A):5243–5244, August 2004.

[69] Y. Lu, S. Song, Z. Song, W. Ren, Y. Xiong, F. Rao, L. Wu, Y. Cheng, and B. Liu. Superlattice-like GaSb/Sb_2Te_3 films for low-power phase change memory. *Scripta Materialia*, 66:702–705, May 2012.

[70] D. Loke, T. H. Lee, W. J. Wang, L. P. Shi, R. Zhao, Y. C. Yeo, T. C. Chong, and S. R. Elliott. Breaking the speed limits of phase-change memory. *Science*, 336:1566, June 2012.

[71] B. C. Lee, E. Ipek, O. Mutlu, and D. Burger. In *Proceedings of the International Symposium on Computer Architecture*.

[72] R. E. Simpson, M. Krbal, P. Fons, A. V. Kolobov, J. Tominaga, T. Uruga, and H. Tanida. Toward the ultimate limit of phase change in $Ge_2Sb_2Te_5$. *Nano Letters*, 10:414–9, 2010.

[73] L. Perniola, V. Sousa, A. Fantini, E. Arbaoui, A. Bastard, M. Armand, A. Fargeix, C. Jahan, J-F. Nodin, A. Persico, D. Blachier, A. Toffoli, S. Loubriat, E. Gourvest, G. Betti Beneventi, H. Feldis, S. Maitrejean, S. Lhostis, A. Roule, O. Cueto, G. Reimbold, L. Poupinet, T. Billon, B. De Salvo, D. Bensahel, P. Mazoyer, R. Annunziata, P. Zuliani, and F. Boulanger. Electrical behavior of phase-change memory cells based on GeTe. *IEEE Electron Device Letters*, 31(5):488–490, May 2010.

[74] Y. G. Choi, A. Kovalskiy, B-K. Cheong, and H. Jain. Role of local structure in the phase change of Ge-Te films. *Chemical Physics Letters*, 534:58–61, May 2012.

[75] A. Y. Cho. Film deposition by molecular-beam techniques. *Journal of Vacuum Science and Technology*, 8:S31, September 1971.

[76] J. R. Arthur. Molecular beam epitaxy. *Surface Science*, 500(1-3):189–217, March 2002.

[77] J. A. Venables. *Introduction to surface and thin film processes*. Cambridge University Press, Cambridge, 2000. ISBN 9780511755651.

[78] K. A. Reinhardt and W. Kern. *Handbook of silicon wafer cleaning technology*. William Andrew, Norwich, NY, USA, 2nd edition, 2008. ISBN 9780815515548.

[79] B. Z. Nosho, B. R. Bennett, E. H. Aifer, and M. Goldenberg. Surface morphology of homoepitaxial GaSb films grown on flat and vicinal substrates. *Journal of Crystal Growth*, 236(1-3):155–164, March 2002.

[80] M. Noguchi, K. Hirakawa, and T. Ikoma. Intrinsic electron accumulation layers on reconstructed clean InAs (100) surfaces. *Physical Review Letters*, 66(17):2243–2246, 1991.

[81] K. Kanaya and S. Okayama. Penetration and energy-loss theory of electrons in solid targets. *Journal of Physics D: Applied Physics*, 5:43, 1972.

[82] I. K. Robinson. Crystal truncation rods and surface roughness. *Physical Review B*, 33(6): 3830, 1986.

[83] W. Paul, H. P. Reinhard, and U. von Zahn. Das elektrische massenfilter als massenspektrometer und isotopentrenner. *Zeitschrift für Physik A: Hadrons and Nuclei*, 152(2):143, 1958.

[84] D. R. Denison. Operating parameters of a quadrupole in a grounded cylindrical housing. *Journal of Vacuum Science and Technology*, 8(1):266, January 1971.

[85] E. de Hoffmann and V. Stroobant. *Mass spectrometry: Principles and applications*. John Wiley & Sons, Ltd, third edition, April 2007.

[86] P. E. Miller and M. B. Denton. The quadrupole mass filter: Basic operating concepts. *Journal of Chemical Education*, 63(7):617, July 1986.

[87] R. Averbeck, G. Koblmueller, H. Riechert, and P. Pongratz. Nucleation and growth of GaN observed by *in-situ* line-of-sight mass spectrometry. *Journal of Crystal Growth*, 251: 505–509, April 2003.

[88] G. Koblmüller, P. Pongratz, R. Averbeck, and H. Riechert. Delayed nucleation during molecular-beam epitaxial growth of GaN observed by line-of-sight quadrupole mass spectrometry. *Applied Physics Letters*, 80(13):2281, 2002.

[89] G. Koblmüller, P. Pongratz, R. Averbeck, and H. Riechert. Nucleation phenomena during molecular beam epitaxy of GaN observed by line-of-sight quadrupole mass spectrometry. *Physica Status Solidi (a)*, 194(2):515–519, 2002.

[90] J. Y. Tsao, T. M. Brennan, J. F. Klem, and B. E. Hammons. On-line determination of alloy composition during ternary III/V molecular beam epitaxy. *Applied Physics Letters*, 55(8):777–779, 1989.

[91] K. R. Evans, R. Kaspi, C. R. Jones, R. E. Sherriff, V. Jogai, and D. C. Reynolds. Desorption mass spectrometric control of composition during MBE rowth of AlGaAs. *Journal of Crystal Growth*, 127:523–527, 1993.

[92] C. H. Heyn and M. Harsdorff. Simultaneous reflection high-energy electron diffraction oscillations and mass spectroscopy investigations during molecular beam epitaxy growth of (001) GaAs - smooth surfaces or stoichiometric films? *Journal of Crystal Growth*, 150: 117–122, 1995.

[93] F. G. Celii, Y-C. Kao, and H-Y. Liu. *In-situ* composition monitoring of InGaAs/InP using quadrupole mass spectrometry. *Journal of Vacuum Science & Technology A: Vacuum, Surfaces, and Films*, 14(6):3202, November 1996.

[94] R. Held, B. E. Ishaug, A. Parkhomovsky, A. M. Dabiran, and P. I. Cohen. A rate equation model for the growth of GaN on GaN(0001) by molecular beam epitaxy. *Journal of Applied Physics*, 87(3):1219–1226, 2000.

[95] R. Held, D. E. Crawford, A. M. Johnston, A. M. Dabirian, and P. I. Cohen. *In-situ* control of GaN growth by molecular beam epitaxy. *Journal of Electronic Materials*, 26 (3):272–280, March 1997.

[96] F. M. Mao and J. H. Leck. The quadrupole mass spectrometer in practical operation. *Vacuum*, 37(8/9):669–675, 1987.

[97] A. E. Holme, W. J. Thatcher, and J. H. Leck. An investigation of the factors determining maximum resolution in a quadrupole mass spectrometer. *Journal of Physics E: Scientific Instruments*, 5:429, 1972.

[98] A. E. Holme, W. J. Thatcher, and J. H. Leck. An investigation of the factors affecting the performance of the quadrupole mass spectrometer with particular reference to residual gas analysis. *Vacuum*, 22(8):327–330, 1972.

[99] W. E. Austin and J. H. Leck. Optimization of the operation of the small quadrupole mass spectrometer to give minimum long-term instability. *Vacuum*, 41(7-9):2001–2003, 1990.

[100] J. C. Vickerman and I. S. Gilmore, editors. *Surface analysis: the principal techniques.* John Wiley & Sons, Ltd, 2nd edition, 2009.

[101] W. C. Marra, P. Eisenberger, and A. Y. Cho. X-ray total-external-reflection-Bragg diffraction: A structural study of the GaAs-Al interface. *Journal of Applied Physics*, 50(11):6927, 1979.

[102] B. Jenichen, W. Braun, V. M. Kaganer, A. G. Shtukenberg, L. Däweritz, C-G. Schulz, and K. H. Ploog. Combined molecular beam epitaxy and diffractometer system for *in-situ* x-ray studies of crystal growth. *Review of Scientific Instruments*, 74(3):1267–1273, 2003.

[103] E. M. McMillan. Radiation from a group of electrons moving in a circular orbit. *Physical Review*, 68:144, 1945.

[104] E. M. McMillan. The synchrotron - a proposed high energy particle accelerator. *Physical Review*, 68:143, 1945.

[105] F. R. Elder, A. M. Gurewitsch, R. V. Langmuir, and H. C. Pollock. A 70 Mev synchrotron. *Journal of Applied Physics*, 18:810, 1947.

[106] A. W. Searcy. The vapor pressure of germanium. *Journal of the American Chemical Society*, 74(19):4789–4791, 1952.

[107] R. F. Brebrick. Tellurium vapor pressure and optical density at 370-615 Å. *The Journal of Physical Chemistry*, 72(3):1032–1036, 1968.

[108] J. J. Doolan and J. R. Partington. The vapour pressure of tellurium. *Transactions of the Faraday Society*, 20:342–344, 1924.

[109] P. B. Joyce, T. J. Krzyzewski, P. H. Steans, G. R. Bell, J. H. Neave, and T. S. Jones. Shape and surface morphology changes during the initial stages of encapsulation of InAs/GaAs quantum dots. *Surface Science*, 492:345–353, October 2001.

[110] B. H. Koo, T. Hanada, H. Makino, J. H. Chang, and T. Yao. RHEED investigation of the formation process of InAs quantum dots on (100) InAlAs/InP for application to photonic devices in the 1.55 μm range. *Journal of Crystal Growth*, 229:142–146, 2001.

[111] H. Lee, R. Lowe-Webb, W. Yang, and P. C. Sercel. Determination of the shape of self-organized InAs/GaAs quantum dots by reflection high energy electron diffraction. *Applied Physics Letters*, 72(7):812–814, 1998.

[112] K. Yamaguchi, T. Kaizu, K. Yujobo, and Y. Saito. Uniform formation process of self-organized InAs quantum dots. *Journal of Crystal Growth*, 237-239:1301–1306, April 2002.

[113] R. Shayduk and W. Braun. Epitaxial films for Ge-Sb-Te phase change memory. *Journal of Crystal Growth*, 311:2215–2219, 2009.

[114] W. Braun and R. Shayduk. Epitaxy of Ge-Sb-Te phase-change memory alloys. *Applied Physics Letters*, 94:041902, 2009.

[115] D. E. Savage and M. G. Lagally. Direct observation by reflection high-energy electron diffraction of amorphous-to-crystalline transition in the growth of Sb on GaAs(110). *Applied Physics Letters*, 50(24):1719–1721, 1987.

[116] R. Shayduk, F. Katmis, W. Braun, and H. Riechert. Epitaxial growth and structure of Ge-Sb-Te phase change materials on GaSb. *Journal of Vacuum Science & Technology B*, 28(3):C3E1–C3E5, 2010.

[117] F. Katmis, R. Calarco, K. Perumal, P. Rodenbach, A. Giussani, M. Hanke, A. Proessdorf, A. Trampert, F. Grosse, R. Shayduk, R. Campion, W. Braun, and H. Riechert. Insight into the growth and control of single-crystal layers of Ge-Sb-Te phase-change material. *Crystal Growth & Design*, 11:4606–4610, 2011.

[118] R. E. Simpson, P. Fons, A. V. Kolobov, M. Krbal, and J. Tominaga. Enhanced crystallization of GeTe from an Sb_2Te_3 template. *Applied Physics Letters*, 100(2):021911, 2012.

[119] J. Stoemenos and R. Vincent. Twinning faults in epitaxial films of germanium telluride and GeTe-SnTe alloys. *Physica Status Solidi (A)*, 11(2):545–558, June 1972.

[120] S. Kaneko, K. Akiyama, T. Ito, M. Yasui, M. Soga, Y. Hirabayashi, H. Funakubo, and M. Yoshimoto. Large lattice misfit on epitaxial thin film: Coincidence site lattice expanded on polar coordinate system. *Japanese Journal of Applied Physics*, 49(8):08JE02, August 2010.

[121] G. F. Kuznetsov and S. A. Aitkhozhin. General orientational characteristics of heteroepitaxial layers of $A^{II}B^{VI}$ semiconductors on sapphire and semiconductor substrates with diamond and sphalerite structures ($A^{III}B^{V}$). *Crystallography Reports*, 47(3):514–518, May 2002.

[122] M. Grundmann. Formation of epitaxial domains: Unified theory and survey of experimental results. *Physica Status Solidi (B)*, 248(4):805–824, April 2011.

[123] J. Narayan and B. C. Larson. Domain epitaxy: A unified paradigm for thin film growth. *Journal of Applied Physics*, 93(1):278, 2003.

[124] M. Grundmann, T. Böntgen, and M. Lorenz. Occurrence of rotation domains in heteroepitaxy. *Physical Review Letters*, 105(14):1–4, September 2010.

[125] T. Asano and H. Ishiwara. Epitaxial relations in group-IIa Fluoride/Si (111) heterostructures. *Applied Physics Letters*, 42(6):517–519, 1983.

[126] A. Giussani, P. Zaumseil, P. Rodenbach, G. Weidner, M. A. Schubert, D. Geiger, H. Lichte, P. Storck, J. Wollschläger, and T. Schroeder. Defect structure of Ge(111)/cubic Pr_2O_3(111)/Si(111) heterostructures: Thickness and annealing dependence. *Journal of Applied Physics*, 106:073502, 2009.

[127] H. Zogg and S. Blunier. Molecular beam epitaxial growth of high structural perfection CdTe on Si using a (Ca,Ba)F_2 buffer layer. *Applied Physics Letters*, 49(22):1531–1533, 1986.

[128] R. T. Lechner, G. Springholz, M. Hassan, H. Groiss, R. Kirchschlager, J. Stangl, N. Hrauda, and G. Bauer. Phase separation and exchange biasing in the ferromagnetic IV-VI semiconductor $Ge_{1-x}Mn_xTe$. *Applied Physics Letters*, 97:023101, 2010.

[129] A. Y. Cho. Growth of III-V semiconductors by molecular beam epitaxy and their properties. *Thin Solid Films*, 100:291–317, 1983.

[130] F. Tong, X. S. Miao, Y. Wu, Z. P. Chen, H. Tong, and X. M. Cheng. Effective method to identify the vacancies in crystalline GeTe. *Applied Physics Letters*, 97(26):261904, 2010.

[131] J. Akola and R. Jones. Structural phase transitions on the nanoscale: The crucial pattern in the phase-change materials $Ge_2Sb_2Te_5$ and GeTe. *Physical Review B*, 76(23):1–10, December 2007.

[132] A. M. Farid, H. E. Atyia, and N. A. Hegab. AC conductivity and dielectric properties of Sb_2Te_3 thin films. *Vacuum*, 80(4):284–294, October 2005.

[133] B. Lv, S. Hu, W. Li, X. Di, L. Feng, J. Zhang, L. Wu, Y. Cai, B. Li, and Z. Lei. Preparation and characterization of Sb_2Te_3 thin films by coevaporation. *International Journal of Photoenergy*, Article ID 476589:1–4, 2010.

[134] L. M. Goncalves, P. Alpuim, A. G. Rolo, and J. H. Correia. Thermal co-evaporation of Sb_2Te_3 thin-films optimized for thermoelectric applications. *Thin Solid Films*, 519: 4152–4157, April 2011.

[135] J. Y. Yang, W. Zhu, X. H. Gao, X. A. Fan, S. Q. Bao, and X. K. Duan. Electrochemical aspects of depositing Sb_2Te_3 compound on Au substrate by ECALE. *Electrochimica Acta*, 52(9):3035–3039, February 2007.

[136] I. Y. Erdogan and Ü. Demir. Synthesis and characterization of Sb_2Te_3 nanofilms via electrochemical co-deposition method. *Journal of Electroanalytical Chemistry*, 633:253–258, August 2009.

[137] R. Venkatasubramanian, T. Colpitts, E. Watko, M. Lamvik, and N. El-masry. MOCVD of Bi_2Te_3 , Sb_2Te_3 and their superlattice structures for thin-film thermoelectric applications. *Journal of Crystal Growth*, 170:817–821, 1997.

[138] Z. Aabdin, M. Winkler, D. Bessas, J. König, N. Peranio, O. Eibl, R. Hermann, and H. Böttner. Sb_2Te_3 and Bi_2Te_3 thin films grown by molecular beam epitaxy at room temperature. *MRS Proceedings*, 1329, 2011.

[139] S. Hasegawa. Reflection high-energy electron diffraction. In *Characterization of materials*, number 5. John Wiley & Sons, Inc., 2002. ISBN 9780471266969.

[140] A. Ichimiya and P. I. Cohen. *Reflection high energy electron diffraction.* Cambridge University Press, Cambridge, 1st edition, 2004. ISBN 0521453739.

[141] J. Narayan, P. Tiwari, X. Chen, J. Singh, R. Chowdhury, and T. Zheleva. Epitaxial growth of TiN films on (100) silicon substrates by laser physical vapor deposition. *Applied Physics Letters*, 61(11):1290–1292, 1992.

[142] Y. Liu, M. Ying, X. Du, J. Jia, Q. Xue, X. Han, and Z. Zhang. The 30° rotation domains in wurtzite ZnO films. *Journal of Crystal Growth*, 290(2):631–636, May 2006.

[143] F. Grey and J. Bohr. A symmetry principle for epitaxial rotation. *Europhysics Letters*, 18(8):717–722, 1992.

[144] G. W. Burr, M. J. Breitwisch, M. Franceschini, D. Garetto, K. Gopalakrishnan, B. Jackson, B. Kurdi, C. Lam, L. A. Lastras, A. Padilla, B. Rajendran, S. Raoux, and R. S. Shenoy. Phase change memory technology. *Journal of Vacuum Science & Technology B: Microelectronics and Nanometer Structures*, 28(2):223–262, 2010.

[145] H. S. P. Wong, S. Raoux, S. Kim, J. Liang, J. P. Reifenberg, B. Rajendran, M. Asheghi, and K. E. Goodson. Phase change memory. *Proceedings of the IEEE*, 98(12):2201–2227, 2010.

[146] L. P. Shi, T. C. Chong, X. Q. Wei, R. Zhao, W. J. Wang, H. X. Yang, H. K. Lee, J. M. Li, N. Y. Yeo, K. G. Lim, X. S. Miao, and W. D. Song. Investigation of nano-phase change for phase change random access memory. *Non-Volatile Memory Technology Symposium*, 7(C):76–80, 2006.

[147] S. Lai and T. Lowrey. OUM-A 180 nm nonvolatile memory cell element technology for stand alone and embedded applications. *International Electron Devices Meeting*, pages 36.5.1–36.5.4, 2001.

[148] M. H. R. Lankhorst, B. W. S. M. M. Ketelaars, and R. A. M. Wolters. Low-cost and nanoscale non-volatile memory concept for future silicon chips. *Nature Materials*, 4(4): 347–352, April 2005.

[149] T. C. Chong, L. P. Shi, R. Zhao, P. K. Tan, J. M. Li, H. K. Lee, X. S. Miao, A. Y. Du, and C. H. Tung. Phase change random access memory cell with superlattice-like structure. *Applied Physics Letters*, 88(12):122114, 2006.

[150] K. Makino, J. Tominaga, and M. Hase. Ultrafast optical manipulation of atomic arrangements in chalcogenide alloy memory materials. *Optics Express*, 19(2):1260–1270, January 2011.

[151] W. Braun, H. Möller, and Y. H. Zhang. Reflection high-energy electron diffraction during substrate rotation: A new dimension for *in-situ* characterization. *Journal of Vacuum Science & Technology B: Microelectronics and Nanometer Structures*, 16(3):1507, May 1998.

[152] A. Proessdorf, F. Grosse, W. Braun, F. Katmis, H. Riechert, and O. Romanyuk. Analysis of GaSb and AlSb reconstructions on GaSb(111) A- and B-oriented surfaces by azimuthal-scan reflection high-energy electron diffraction. *Physical Review B*, 83:155317, April 2011.

[153] N. Yamada, E. Ohno, K. Nishiuchi, N. Akahira, and M. Takao. Rapid-phase transitions of GeTe-Sb_2Te_3 pseudobinary amorphous thin films for an optical disk memory. *Journal of Applied Physics*, 69(5):2849–2856, 1991.

[154] W. S. Lee, G. W. Yoffe, D. G. Schlom, and J. S. Harris. Accurate measurement of MBE substrate temperature. *Journal of Crystal Growth*, 111:131–135, 1991.

[155] B. V. Shanabrook, J. R. Waterman, J. L. Davis, and R. J. Wagner. Large temperature changes induced by molecular beam epitaxial growth on radiatively heated substrates. *Applied Physics Letters*, 61(19):2338–2340, 1992.

[156] Y. Takahira and H. Okamoto. Measurement of MBE substrate temperature by photoluminescence. *Journal of Crystal Growth*, 175-176:267–272, May 1997.

[157] T. Matsunaga, R. Kojima, N. Yamada, K. Kifune, Y. Kubota, Y. Tabata, and M. Takata. Single structure widely distributed in a GeTe-Sb_2Te_3 pseudobinary system: A rock salt structure is retained by intrinsically containing an enormous number of vacancies within its crystal. *Inorganic Chemistry*, 45(5):2235–2241, 2006.

[158] T. Janssen and A. Janner. Incommensurability in crystals. *Advances in Physics*, 36(5): 519–624, January 1987.

[159] H. Z. Cummins. Experimental studies of structurally incommensurate crystal phases. *Physics Reports*, 185(5-6):211–409, January 1990.

[160] X. Liu, Y. Sasaki, L. V. Titova, P. M. Reimer, and J. K. Furdyna. Fabrication and characterization of III-V semiconductor superlattices with sinusoidal compositional modulation. *Physica E: Low-dimensional Systems and Nanostructures*, 13:1143–1146, March 2002.

[161] W. Zhang, H. S. Jeong, and S. A. Song. Martensitic transformation in $Ge_2Sb_2Te_5$ alloy. *Advanced Engineering Materials*, 10(1-2):67–72, February 2008.

[162] P. Rodenbach, K. Perumal, F. Katmis, W. Braun, R. Calarco, and H. Riechert. Epitaxy of single crystal phase change materials on Si(111). *MRS Proceedings*, 1338, June 2011.

[163] H. K. Peng, K. Cil, A. Gokirmak, G. Bakan, Y. Zhu, C. S. Lai, C. H. Lam, and H. Silva. Thickness dependence of the amorphous-cubic and cubic-hexagonal phase transition temperatures of GeSbTe thin films on silicon nitride. *Thin Solid Films*, 520:2976–2978, January 2012.

[164] S. Raoux, J. L. Jordan-Sweet, and A. J. Kellock. Crystallization properties of ultrathin phase change films. *Journal of Applied Physics*, 103(11):114310, 2008.

[165] Y. Yin, H. Sone, and S. Hosaka. Dependences of electrical properties of thin GeSbTe and AgInSbTe films on annealing. *Japanese Journal of Applied Physics*, 44(8):6208–6212, August 2005.

[166] W. Zhang, A. Thiess, P. Zalden, R. Zeller, P. H. Dederichs, J-Y. Raty, M. Wuttig, S. Blügel, and R. Mazzarello. Role of vacancies in metal-insulator transitions of crystalline phase-change materials. *Nature Materials*, 11(11):952–956, October 2012.

List of Figures

List of Tables

Acknowledgement

It gives me immense pleasure to express my deepest gratitude to all those who have directly, or indirectly contributed to the successful completion of my thesis.

I am truly indebted and thankful to Dr. Wolfgang Braun, who showed faith in me and gave an interesting and fascinating topic to work on as part of my doctoral thesis. He gave me full freedom to work on this interesting project and was a source of continuous support.

I owe sincere and earnest thanks to Prof. Henning Riechert for giving me a chance to carry out my doctoral research at Paul-Drude-Institut für Festkörperelektronik. Especially, I would like to thank him for giving me the opportunity to attend and present my results in various conferences.

I thank Prof. Andreas D. Wieck and Prof. Ted Masselink for taking their time to review this work.

Special thanks go to Dr. Andre Prößdorf, for he was always there to help me out giving suggestions and ideas. Right from the beginning of my thesis, he was a source of constant support and was the first person I would go, when in need of help related to my work.

I would like to thank Dr. Michael Hanke for teaching me the basics of synchrotron based grazing incidence x-ray diffraction and also for going through my thesis, giving suggestions for its improvement.

I thank Dr. Raffaella Calarco for her help during my final stages of my PhD in correcting my thesis and giving valuable comments for its improvement. I would also like to thank Ferhat Katmis for his support during my initial days at PDI and Dr. Peter Rodenbach for his help in x-ray analysis and fruitful discussions. Special thanks go to Dr. Alessandro Giussani for sharing almost half of my burden during the final stages of my PhD. We spent a lot of time together trying to understand the growth of GST films and superlattices. Will never forget the time spent during the successful and not so successful synchrotron measurements at BESSY. I thank BESSY for providing the synchrotron beam and for hosting the MBE.

I thank Dr. Frank Große for his support during my PhD for the innumerable discussions on mass spectroscopy. Thanks to Dr. Vladimir Kaganer for his special interest in our work during the group meetings and the constructive discussions on x-ray diffraction analysis. Whenever I see him, I remember the first day at PDI and his help in finding me an accommodation. I also thank Dr. Oliver Bierwagen for his support during the later stages of my PhD.

This work would not have been possible within 3 years without the help of these two important people: Carsten Stemmler and Steffen Behnke. Steffen took care of the MBE system, and was highly instrumental in moving the MBE system into the beamline and get it work within a short period of time. Without his experience, it would have been an enormous task for us to get it ready on time for the synchrotron measurements. Special thanks to Carsten for helping me out with the numerous hardware software interfacing problems. He also took care of the digitization

of the lab books and backup of the huge amount of data that I had saved during the course of my work. Apart from the work, I had nice time with him going to Indian restaurants or discussing about football.

During the course of my thesis, I was fortunate to collaborate with Dr. Alexander Kolobov and Dr. Paul Fons. I sincerely thank them for the fruitful discussions on phase change materials. I am truly indebted and thankful to Dr. Richard Campion for the few days he spent with us and for showing how effective one can use the quadrupole mass spectrometer. It greatly helped me in understanding the complexities involved in the GST growth. I should also thank Dr. Wolfgang Braun for inviting him.

I thank Bernd Jenichen for discussions on x-ray diffraction at the lab diffractometer, Anne-Kathrin Blum for the SEM measurements and Martin Dubslaff for helping us at the microdiffraction beamline at ESRF. I also thank Claudia Hermann for her help with InAs buffer growth and Mr. Jürgen Weiß for his help in transport and logistics from PDI to BESSY.

I thank Dr. Tamil Selvi *akka* for going through my thesis and giving ideas and suggestions for improving it. Also, I should thank her for taking me out of my comfort zone by showing few places in Europe. I am indebted and thankful to Prof. Govindaswamy Rajagopal for writing a nice poem in tamil for my dedication section.

My stay here would not have been possible without the support of my friends and I take this opportunity to thank all of them, who made my stay as enjoyable as possible. First, I would like to thank Shilly and Meetu, my long term friends here in Germany who made my life much easier. When I first came to Germany I was totally unprepared and it happened to be a weekend. Shilly fed me for the first two days till I got some stuff to cook on my own. Learnt a bit of cooking from her, which helped me to survive the last three years.

Thanks to Meetu for the nice Punjabi food, she used to prepare during innumerable visits to her home. She was always there to listen to my day-to-day stories. Lot of weekends were spent with her, either going out together or preparing new dishes. Special thanks to her for encouraging me to write in Latex.

Dr. Sivanesan, his wife Kalaivani and Kommi Naveen made my initial days in Berlin enjoyable. Thanks to Kalai for the nice food, which she used to pack for me. I sincerely thank Raja *anna* and his family for taking care of me and inviting to their home once in a while.

I thank my friend Anil for being a nice and caring neighbour. He always accompanied me to most of my sports activities. Whenever I was late from my office, he was always there to prepare nice dinner for me. Thanks also to his wife Niharika for preparing nice pasta and briyanis during the weekends and also accompanying us for playing badminton.

Also I want to thank my other Indian friends who made my stay in Berlin comfortbale and enjoyable. They include: Ananth, Vallini, Thiru, Kiran, Atul, Aditya, Vikram Singh Raghuwanshi, Vikram Patil, Ravi, Jatin, Rajesh, Ananyu, Kumar, Mals. I wish a good time to all of them.

Above all, I am indebted and thankful to Deutscher Akademischer Austausch Dienst (DAAD) for offering me a scholarship without which my stay here would not have been possible.

My deepest gratitude goes to my family members. My *amma* and *appa* for their unfailing love and support which proved invaluable throughout my life. They gave me full freedom to pursue my endeavours. This work is dedicated to them. Special thanks to my *akka* and *thambi* for their love and care. They were a source of constant support and everlasting optimism.

Selbständigkeitserklärung

Ich erkläre, dass ich die vorliegende Arbeit selbständig und nur unter Verwendung der angegebenen Literatur und Hilfsmittel angefertigt habe.

Berlin, den July 17, 2013 Karthick Perumal